Radio-frequency atomic magnetometry with a rubidium Bose-Einstein condensate

Yuval Cohen

A dissertation submitted in partial fulfillment

of the requirements for the degree of

Doctor of Philosophy

of

University College London.

Department of Physics & Astronomy

University College London

November 16, 2021

I, Yuval Cohen, confirm that the work presented in this thesis is my own. Where information has been derived from other sources, I confirm that this has been indicated in the work.

Abstract

This thesis details progress in radio-frequency atomic magnetometry with ultracold rubidium atoms. Motivations and context are first covered, before an introduction of the main concepts required to understand the underlying physics is given. At first, a cold atom magnetometer is designed, built and characterised. Consistent 20 µK atoms are produced. Radio-frequency (RF) atomic magnetometry (AM) is performed by placing the atoms in a bias magnetic field and generating coherent precession with an external AC field. A noise floor at $330\,\mathrm{pT}/\sqrt{\mathrm{Hz}}$ defines the sensor's sensitivity, with a range of applications.

RF-AM is then performed with a Bose-Einstein condensate (BEC). The 20 µK atoms are loaded into a magnetic trap, where RF evaporation increases their phase space density (PSD $= n\lambda_{dB}^3$, n is the density and λ_{dB} is the thermal de Broglie wavelength of the atoms). Next, atoms are transferred into a hybrid dipole trap, collecting in a dimple created at the intersect of two high power laser beams. Production and stabilisation of these beams is described, which are focused down to a 75 µm beam waist at the trap position with a total power of 7 W. Optimisation of the evaporation process in both traps leads to consistent BEC production. A pure condensate with 4×10^4 atoms at 25 nK is reported.

Radio-frequency magnetometry is performed at various probe volumes. With systematic optimisation a best AC sensitivity of $24\,\mathrm{pT}/\sqrt{\mathrm{Hz}}$ with 3.4×10^8 atoms in the magnetic trap before evaporation is achieved. This is extended to the BEC with 4×10^4 atoms, where an AC sensitivity of $84\,\mathrm{nT}/\sqrt{\mathrm{Hz}}$ and DC sensitivity of $14\,\mathrm{nT}/\sqrt{\mathrm{Hz}}$ is reported, bringing previously achieved atomic magnetometry into the micrometer regime. A trade-off must be considered due to reduction in sensitivity at

lower probe volumes. Volumes between 1.4×10^{-7} m^3 and 1.6×10^{-14} m^3 can be accessed, highlighting the sensors adaptability and tunability for different applications. The results are contextualised in the background of previously achieved magnetometers of various types. Finally, proof-of-concept electromagnetic induction imaging (EMI) measurements are made to confirm the sensor's viability for high resolution imaging.

Impact Statement

Applications of magnetometers are plentiful, and so the impact of the one developed in this thesis is considerable. Specifically, the ultracold RF-AM provides a sensing volume of $1.6 \times 10^{-14}\,\mathrm{m}^3$. This could be leveraged for high spatial resolution applications, where the sensing volume is the limiting factor. Electromagnetic induction imaging (EMI) will benefit from such a decrease in probing volume, with current demonstrations limited to millimetre resolution [25, 61]. Proof-of-concept measurements have been made here, with future implementations expected to make a meaningful contribution to industry and academia.

Within academia, the work presented here has led to journal publications [1, 2]. These report work on both cold atom and vapour cell magnetometry. The work is funded by the Engineering and Physical Sciences Research Council (EPSRC), supporting this project financially. Collaborations have been established with other universities, and research on the thesis topic is ongoing. Much of the work is motivated by applications in industry, leading to significant impact outside of academia. Funding from the Defence Science and Technology Laboratory (DSTL) for projects with different technology readiness levels (TRLs) has lead to collaboration with many different industry partners.

Finally, from an outreach and education point of view, the work here has been presented at events such as the University College London's Quantum Science and Technology Institute (UCLQ) industry day, UCLQ quantum lunch, and to potential future PhD applicants at the UCLQ summer school. Both undergraduate and postgraduate students have been exposed to this area of research, through practical lab work, lab tours and lectures.

Acknowledgements

I would like to first thank my supervisor Prof. Ferruccio Renzoni, for giving me the opportunity to work and learn in your research group. Your ability to set long term goals and focus the work is invaluable. You gave me freedom to explore, knowing when to let me figure things out on my own and when to gently nudge me in the right direction. There are many things you said which will stick with me throughout my work life, and I appreciate you progressively entrusting me with more responsibility in the lab as I matured as a student.

My first two years were also heavily shaped by Luca. I appreciate the foundation you gave me in experimental atomic physics, as well as your contribution to the project and day-to-day work. Cameron, thank you for your guidance and friendship. I admire your work ethic and approach to science, even if you do speak about cricket too much. To other group members, some already gone: Antonio, Michela, Pik, and some still present: Ben, Han, Krishna, Sindi; thanks for always making the lab a great place to spend my days. Ben in particular, who I started my cold atom journey with five years ago at the University of Birmingham, thank you for the endless hours spent discussing my (at times tedious) problems with the experiment. It seems our academic journeys are strongly linked.

From a personal point of view, I have to thank my friends. There are too many to list, but I want to mention the six: Ben, Charlie, Gil, Joe, Joel, and Toby. You all showed me it is cool to be a science nerd, and I would not have made it here without you. To my family, although I don't say it enough, you are the wind at my back. I am forever aware of your support and encouragement. The things I have achieved are because of the confidence you instilled in me. I appreciate everything you have done

to get me to where I am today. Finally, to my girlfriend Talia. You have been with me every step of the way through this PhD journey. At this point you probably know the thesis better than I do, and I cannot overstate how much easier you have made the process. But more importantly, thank you for being someone I want to share my life with.

Contents

1 Magnetometry - General principles **20**

1.1 Types of magnetometers 22

1.2 Criteria for magnetometers 25

1.2.1 Shielding 25

1.2.2 Portability 26

1.2.3 Sensitivity 26

1.2.4 Spatial resolution 32

1.3 Thesis Outline 35

2 RF Magnetometer - Concepts **36**

2.1 Rubidium 87 36

2.2 Zeeman splitting 37

2.3 Bloch Equations 39

2.4 Optical Pumping 42

2.5 Polarisation Rotation 43

2.6 Phase sensitive detection 44

3 Ultracold atoms - Concepts **46**

3.1 Laser cooling 46

3.2 Evaporative cooling 47

3.2.1 Magnetic trapping 48

3.2.2 Dipole trapping 51

3.2.3 Hybrid Trapping 54

3.3 Bose-Einstein Condensation 56
3.3.1 Non-interacting trapped bosons 57
3.3.2 Interacting trapped bosons 59

4 Cold AM - Apparatus 62
4.1 Vacuum system 62
4.1.1 Baking 62
4.1.2 Pressure measurement 63
4.1.3 Atomic source 65
4.2 Laser control 67
4.2.1 Frequency and intensity control 67
4.3 Magnetic field control 71
4.4 Magnetometry 76

5 Cold AM - Results 79
5.1 Sequence 79
5.2 Optimisation 80
5.3 Sensor characterisation 84

6 Ultracold AM - Apparatus 88
6.1 Magnetic Trapping 88
6.1.1 Evaporation 89
6.2 Hybrid Trapping 94
6.2.1 Stabilisation system 95
6.2.2 Beam size 97
6.2.3 Trap loading 98
6.2.4 Evaporation 102
6.3 Magnetometry 103
6.3.1 Probe beam 104
6.3.2 Active bias field compensation 106
6.3.3 Phase sensitive detection 109
6.3.4 Magnetometry delay 111

6.3.5 Re-optimisation 112

7 Ultracold AM - Results **115**

7.1 Bose-Einstein Condensation 115

7.2 Sensor Characterisation 120

7.3 Conductivity measurements 123

8 Conclusions **127**

8.1 Outlook 128

8.2 Further Work 128

Appendices **130**

A Imaging system **130**

A.1 Fluorescence 130

A.2 Absorption 130

A.2.1 Atom Number 133

A.2.2 Temperature 135

A.2.3 Optical pumping out of resonance 135

A.3 BEC fitting 136

B Optimisation **143**

C Computer systems **144**

Bibliography **145**

List of Figures

1.1 Noise against bin size 28
1.2 Bin centring effect on SNR 29
1.3 Example amplitude spectrum 30
1.4 Phase sensitive detection 31
1.5 AC & DC sensitivity 31
1.6 Sensitivity vs. Probe volume 33
1.7 ^{87}Rb density 34

2.1 ^{87}Rb energy levels 38
2.2 Zeeman splitting 39
2.3 Rotating frame transformation 42
2.4 Optical pumping 43
2.5 RF magnetometry 44
2.6 Bloch equations simulation 45

3.1 Magnetic trap potential surface 49
3.2 Dipole trap depth and scattering rate 53
3.3 Single beam focused trap simulation 53
3.4 Crossed beam evaporation 54
3.5 Hybrid trap potential surface 55
3.6 Dipole trap beam angle estimation 56
3.7 Transition temperature 59

4.1 Vacuum system 63
4.2 Baking 64

4.3 MOT lifetime . . . 65
4.4 Ampoule temperature . . . 66
4.5 Optical setup . . . 68
4.6 Cooling VCO calibration . . . 69
4.7 Cooling locking point . . . 70
4.8 Cooling AOM double frequency driving . . . 71
4.9 DC2240A Power supply . . . 72
4.10 Magnetic field control . . . 72
4.11 Water-cooled coils . . . 73
4.12 Current stabilisation . . . 74
4.13 Hall voltage calibration . . . 74
4.14 Magnetic field gradient ramping . . . 75
4.15 Simulated failure of water-cooling . . . 75
4.16 Kill switch logic . . . 76
4.17 Magnetometer setup . . . 77
4.18 Probe power calibration . . . 78

5.1 Sequence . . . 80
5.2 Transverse fields compensation . . . 82
5.3 RF power broadening simulation . . . 82
5.4 RF power broadening . . . 83
5.5 Polarimeter signal . . . 85
5.6 Coherence time extraction . . . 85
5.7 Cold magnetometer characterisation . . . 86
5.8 Dynamic range . . . 87
5.9 Atom number scaling . . . 87

6.1 Magnetic trap loading - duration . . . 89
6.2 Magnetic trap loading - gradient . . . 90
6.3 Magnetic trap lifetime . . . 90
6.4 RF evaporation . . . 91

6.5 First RF evaporation optimisation 92
6.6 RF evaporation amplifier calibration 93
6.7 PSD vs. RF power 93
6.8 Final RF optimisation 94
6.9 Dipole trap laser calibration 94
6.10 Dipole trap setup 95
6.11 Dipole trap stabilisation 96
6.12 Dipole trap power calibration 96
6.13 Dipole trap voltage inverter 97
6.14 Dipole trap beams size 98
6.15 Dipole trap alignment 99
6.16 Dipole trap temperature change 100
6.17 Dipole trap extinction ratio 101
6.18 Dipole trap power balance 101
6.19 Offset field 102
6.20 Dipole trap lifetime 102
6.21 Dipole trap load setpoint optimisation 103
6.22 Final evaporation setpoint optimisation 104
6.23 Probe beam upgrade 105
6.24 Probe power optimisation 106
6.25 FLC100 mount 107
6.26 FLC100 calibration 107
6.27 FLC100 during sequence 108
6.28 FLC100 PID locking 108
6.29 Phase sensitive detection simulated signal 110
6.30 Gated operation of Keysight 33120A 111
6.31 Offline phase sensitive detection 111
6.32 Magnetometry delay 112
6.33 Bias field direction 113
6.34 Gradient compensation 114

6.35 Magnetic resonance in 2nd RF and dipole trap load 114

7.1 Overall sequence 116
7.2 Sequence images 117
7.3 Overall evaporation sequence 118
7.4 BEC production 119
7.5 BEC aspect ratio inversion 119
7.6 Magnetic trap magnetometry 120
7.7 BEC magnetometry 121
7.8 Sensitivity vs. atom number & probe volume 122
7.9 Contextualised sensitivity results 123
7.10 EMI setup 124
7.11 Magnetic trap conductivity measurements 125
7.12 2nd RF conductivity measurements 126
7.13 Dipole trap conductivity measurements 126

A.1 Imaging atoms with a single lens 131
A.2 Magnification and camera position 132
A.3 Temperature measurement - image of atoms 136
A.4 Temperature measurement 136
A.5 Optical pumping out of resonance 137
A.6 Filtered image 139
A.7 Automatic locating of atoms in an image 140
A.8 Multi-function 1D fitting of BEC images 141
A.9 Comparison with no BEC fraction 141
A.10 Simulated data BEC fitted fraction 142

B.1 Optimisation 143

C.1 Computer Control 144

List of Tables

4.1 Magnetic field control 72

6.1 780 nm filter for stabilisation 105
6.2 Active bias field stabilisation single runs 109
6.3 Active bias field stabilisation averaged runs 109
6.4 Magnetic field setpoint 113

A.1 Magnification 132

List of Acronyms

AM	Atomic Magnetometer
AOM	Acousto-Optic Modulator
BEC	Bose-Einstein Condensate
C-MOT	Compressed Magneto Optical Trap
DAQ	Data Acquisition
DT	Dipole Trap
EMI	Electromagnetic Induction imaging
FFT	Fast Fourier Transform
HWP	Half-Wave plate
LIA	Lock-in Amplifier
LVIS	Low Velocity Intense Source
MIT	Magnetic Induction Tomography
MOT	Magneto Optical Trap
MT	Magnetic Trap
NV	Nitrogen Vacancy
OD	Optical Density
OP	Optical Pumping
PBS	Polarising Beam Splitter
PGC	Polarisation Gradient Cooling
PSD	Phase Space Density
QWP	Quarter-Wave plate
RF	Radio-frequency
SNR	Signal to Noise Ratio
SQUID	Superconducting Quantum Interference device

Chapter 1

Magnetometry - General principles

Sensing of the environment is ubiquitous. Our interaction with the world, dominated by technological advancement, is now completely reliant on a plethora of different sensors. As progress accelerates, so does our sensing capability. Previously unattainable sensitivities to small changes in the environment are now possible. Magnetic fields are omnipresent. Whether man-made, natural or biological, these contain information about the state of a system. This is the concern of this thesis, the measurement of magnetic fields to drive forward state of the art technology.

Applications of magnetometers is plentiful, from medical to industrial. Magnetometers have been used to perform magnetic resonance imaging (MRI) [3, 4] and magnetoencephalography [5, 6] (detection of magnetic fields generated by brain activity). In industry, magnetometers have found uses in industrial imaging [7], mechanical stress measurements [8], coal and mineral exploration [9], and in the oil industry. Magnetometers are also used for submarine activity monitoring, which are regularly degaussed to avoid detection, and many techniques use magnetic field measurements for navigation [10], with the compass invented over two millennia ago. The space industry also uses magnetometers [11] (e.g. for navigation [12]), and most modern mobile phones have built in magnetometers [13]. Other applications include nuclear magnetic resonance (NMR) measurements [14], nuclear quadrupole resonance (NQR) measurements [15], and fundamental physics [16, 17, 18].

The work presented in this thesis is with the outlook of using a magnetometer for electromagnetic induction imaging (EMI). In recent years, efforts have been devoted

to development and application of atomic magnetometers for this purpose. Imaging of sample objects is performed by applying an AC magnetic field which induces eddy currents in the target. These produce a secondary field, in response to the primary field, which contains details of the sample's properties (namely the conductivity σ, relative permittivity ε_r, and relative permeability μ_r). The combination of the primary and secondary fields defines the total field at the sensor. By detecting this total field, a two dimensional image is built, moving either the sample or sensor to record data for different pixels. Magnetic induction tomography (MIT) can be performed by changing the applied AC field's frequency, penetrating into the sample at different depths, allowing for three dimensional images to be obtained when combined with suitable reconstruction algorithms.

EMI has been successfully applied to security screening [19, 20, 21]. Whilst conventional X-ray scanners perform well in some conditions, and are able to image through barriers, due to their ionising radiation they cannot be used in many applications. On the other hand, EMI is inherently safe (with low power magnetic fields applied to the target) whilst still allowing through barriers imaging. For improved penetration, lower operating frequencies must be used. This is where atomic magnetometers outperform existing inductive pick up coils, with AMs maintaining sensitivity at relatively low frequencies (kHz). Furthermore, EMI has also been applied to surveillance, such as underwater detection [22]. With existing detection methods relying on the magnetisation of an object, EMI's response to conductivity improves on current methods, as countermeasures to avoid detection are more difficult. Finally, efforts to use EMI to image biological tissues have also been fruitful. With minimum conductivities imaged improved upon regularly, now down to single $\mathrm{S\,m^{-1}}$, biological imaging can be envisaged in the near future [23, 24, 25]. These tools will aid in diagnosis of head injuries and atrial fibrillation [26, 27], allowing non-invasive imaging of organs. In addition, portable AMs will allow rapid diagnosis in the field [2].

While AMs are driving progress in applications of EMI, they are limited by their spatial resolution, which is set by both the proximity of the sensor to the target (due to the reduction of the secondary field magnitude) and the sensor's volume. Efforts

to miniaturise AMs are ongoing [28], but micro meter resolution is unfeasible using current technology. This is where an ultracold sensor improves on current state-of-the-art, as the spatial resolution can be smaller than 100 µm due to the small dense atomic cloud acting as the sensor. Furthermore, direct measurement and control of the atom temperature, density and number can be made. These parameters can be tailored to improve the magnetometers response for a specific task. In addition, in contrast to vapour cell magnetometers which must rely on buffer gases to avoid spin relaxing collisions with the walls of the cell, trapped cold atoms in ultra-high vacuum provide excellent isolation from the environment.

In the next sections, competitors to atomic magnetometers are discussed before the criteria for a useful sensor is presented. Here, a comparison of the achievable sensing volume for different magnetometers is described, highlighting the benefits of an ultracold AM to further motivate the thesis subject.

1.1 Types of magnetometers

Magnetometry describes the building of machines sensitive to magnetic fields. When considering any sensing element, different criteria can characterise and define the usefulness of a sensor. A large part of the motivation for work in this field has been applications of the technology. With this goal in mind, many different types of magnetometers have been developed, each with their own unique set of properties. It is important to understand and consider the different options available within the field, and why this thesis and research has been focused on ultracold radio-frequency magnetometry. Let us first define a sensor. Sensors translate a change or state of a property, in this case magnetic field, into a more useful change of a different property, for example electric current or potential difference. This translation can allow the user to detect and respond to the change. As much of our technology is based on computers, an electrical signal can be manipulated, analysed and responded to more readily than a magnetic field. Miniaturization also allows for some of these to be incorporated into integrated circuits directly.

Hall probes are the earliest forms of magnetometers. First discovered in 1879

[29], a conductor with flowing current has its charge carriers deflected by the magnetic field to be sensed. This produces a potential difference, known as the Hall voltage, which is directly proportional to the strength of the magnetic field. Hall effect sensors have seen applications from keyboards to anti-lock braking systems. One is used in this BEC experiment, to sense the current in the anti-Helmholtz coils used for magnetic trapping, which is then fed back to a stabilisation system (a current to potential difference converter without interaction with the circuit directly).

Magnetoresistive sensors change their resistance, R, under the influence of magnetic fields. At first used in applications such as badge readers, and later in hard disks, they are widely used in industry today. More recently, the Nobel prize was awarded for work on Giant magnetoresistance (GMR) [30], showing their continued relevance in the field [31].

Fluxgate magnetometers consist of a ring core of highly permeable alloy, with two coils wound on top; a drive coil and sense coil [32]. The drive signal oscillates but causes no net change of flux in the sense coil, as the field induced by the two halves of the drive coil is equal and opposite leading to no induced voltage. Once an external magnetic field is introduced, the balance between the two halves of the drive coil is no longer present, seeing one half come into saturation sooner than the other. A voltage is now induced in the sense coil, and is often integrated, providing a readout proportional to the strength of the magnetic field.

Induction coils rely on Faraday's law of induction, $V = -N\frac{d\Phi}{dt}$, where V is the induced voltage in the coil, N the number of turns in the coil and Φ the magnetic flux. Widely used for their ease of production, cost effectiveness, and large operational range, inductive coils can be found in applications such as MRI.

Superconducting quantum interference devices (SQUIDs), operating at cryogenic temperatures, had for many years shown unmatched magnetic field sensitivities [33, 34, 35]. These have two different working regimes, the RF SQUID and the DC SQUID. Both rely on the flux of the magnetic field, coupled to the SQUID via a detection coil, changing the current flowing in the SQUID loop. SQUIDs have seen applications such as magnetic microscopes and biomedical measurements.

Nitrogen vacancy (NV) colour centres in diamonds have pushed the boundary of high spatial resolution magnetometry [36][37][38]. These exhibit similar quantum properties to traditional atomic magnetometers, where in the case of an NV^- centre, a spin-1 triplet electronic ground state is Zeeman split due to a magnetic field which can then be read out optically. NV centres have seen applications varying from condensed matter physics to neuroscience [39].

Atomic magnetometers (AM) have achieved impressive sensitivities as low as $1 \times 10^{-18}\,\mathrm{T}/\sqrt{\mathrm{Hz}}$ [40, 41, 42], matched only by state of the art SQUID magnetometers. Relatively simple, robust, tunable, able to work in an unshielded environment, and without the need for cryogenic temperatures (in contrast to SQUIDs) these magnetometers have seen many applications. AMs make use of alkali metal atoms, usually confined to a glass cell. Generally, the atomic ensemble is prepared in a state where the populations of the magnetic sub-levels are imbalanced (optical pumping). In this state, the spin of the atoms precesses around a bias magnetic field to be measured [43]. Precession is readout optically with a probe beam. There are many different types of atomic magnetometers.

Radiofrequency AMs (RF-AM) exploit a small oscillating field perpendicular to the bias field to be measured. This field can be viewed as synchronizing the precession of individual spins, discussed further in Section 2.3. As the radio-frequency approaches the Larmor frequency, a resonance is seen, with the largest amplitude of in phase precession at the Larmor frequency. Linking the Larmor frequency to the applied field through γ, the gyromagnetic ratio, allows determination of the field magnitude.

Push-pull AMs replace the radio-frequency field in RF-AMs with modulation of the pumping light (amplitude, frequency or polarisation) [44]. In the case of polarisation modulation, the light is switched between $\sigma+$ and $\sigma-$ at half the Larmor frequency, forcing the spin polarisation into coherent precession. The magnetometer itself does not need to produce any magnetic fields allowing arrays of push-pull magnetometers to be built with minimal cross-talk, increasing the range of available applications. Other all-optical approaches include non-linear magneto-optical rota-

tion (NMOR) magnetometers [45] [46] [47] [48] and Coherent population trapping (CPT) magnetometers [49] [50], where atoms with a three level Λ system are illuminated by bi-chromatic near resonant laser field. When the difference in frequency of the light matches the difference in energy of the ground states, atoms are pumped into a coherent dark state (superposition of the ground states) leading to a reduction in fluorescence. Measurements of the frequency splitting between m_F states can be performed, related to the magnetic field in the usual way.

Spin relaxation due to collisions between alkali metal fundamentally limits AM's achievable sensitivity. At low fields and high density the rate of spin exchange can be larger than the Larmor precession frequency. In this regime, the magnetometer resonance is unaffected by broadening due to spin exchange collisions. So called Spin-exchange relaxation free (SERF) magnetometers have shown the best achieved sensitivities of all atomic magnetometers [51] [52], but their low field working regime limits their applications.

Finally, atomic magnetometers which exploit cold or ultracold atoms as sensing mediums have been built. Previous magnetometers in this category have already shown impressive sensitivities at small probe volumes [53] [54] [55] [56], competing with state of the art SQUIDs. In this work, the unmatched sensitivities and simple detection methods of atomic magnetometers is combined with the high atomic control, high density, Doppler broadening free, long coherence times and potentially improved atom number scaling of sensitivity of ultracold atoms. With EMI application in mind, the RF-AM is chosen for its maintaining of impressive sensitivities in unshielded environments, over a wide frequency range (kHz - MHz [57]), and its previously achieved imaging [7] [58] [59] [60] [21] [22] [61] [25].

1.2 Criteria for magnetometers

1.2.1 Shielding

Some magnetometers require magnetic shielding for their efficient operation. In fact, most magnetometers benefit from magnetic shielding, due to the reduction in noise. However, for many applications, magnetic shielding is prohibited. The best achieved

sensitivity can no longer be exploited and alternatives must be considered. RF-AMs perform very well in unshielded environments, maintaining their sensitivity.

1.2.2 Portability

For applications which require portability of the system, the power consumption of the setup must be considered. This can be linked to feasibility of application in the field. For SQUIDs, cryogenic temperatures limit the foreseeable portable applications. Portable AMs have been realised [2] and ultracold atoms have been produced in transportable devices, even in space [62]. With current available technology it is reasonable to consider future portable versions of ultracold atomic magnetometers.

1.2.3 Sensitivity

We can firstly define the responsivity of a sensor. This can be thought of as the change in the output state, for example potential difference, with respect to a change in magnetic field. In this example, the responsivity of our magnetometer will be in units of V/T. Depending on the detection method of the output, this can be the limit in sensitivity.

Sensitivity is defined as either the noise floor or the resolution of the magnetometer, whichever is smallest. A resolution-limited magnetometer is one whose noise floor is below the smallest step it can output. Taking the example where the resolution of the magnetometer is 1 G, anything below this is treated as no field. The magnetometer is insensitive to fields below 1 G, defining its sensitivity.

Next, we consider the case where the magnetometer is limited by its noise floor. At the same resolution, but with a noise floor of 1.5 G, we can not detect any field smaller than 1.5 G, as we cannot distinguish it from noise. The resolution of the magnetometer is no longer relevant in describing the smallest field measurable. In the case of atomic magnetometers, the noise floor is the limiting factor in the sensitivity, and so will be discussed extensively.

Magnetometers can be sensitive to different types of field. We can consider static DC fields which do not change in time, or oscillating AC fields which do. RF atomic magnetometers perform well in this respect, where by either controlling the static bias

field or the oscillating RF field the magnetometer can be sensitive to either AC or DC fields. As such, it is important to define two different sensitivities, AC and DC.

For proper discussion of the AC sensitivity of an atomic magnetometer we must first consider what kind of output it produces. In vapour cell magnetometers, the output of the balanced polarimeter (see Section 4.4) is fed directly to a spectrum analyser. These can give continuous measurement of the AC field for long periods of time, producing a power spectrum. In this work, the polarimeter signal is acquired for short periods of times, in the 10s of milliseconds, too quick for most spectrum analysers. As such, the polarimeter signal is acquired with a fast oscilloscope, which samples the signal ready for analysis via a Fast Fourier transform (FFT). FFTs give an amplitude spectrum of the signal, which is simply the square root of the power spectrum. The next section will discuss some fundamental concepts in FFT analysis, based on the arguments presented in [63].

The maximum frequency in the FFT is set by the frequency at which the signal is sampled, F_s. The bin size, Δf, set by this sampling frequency is

$$\Delta f = \frac{F_s}{N} \tag{1.1}$$

where N is the number of points obtained. The sampling period, or time per point, is given by $T_s = 1/F_s$, which can be combined with 1.1 to give

$$\Delta f = \frac{1}{NT_s} = \frac{1}{T} \tag{1.2}$$

where T is the signal length in time. The measured noise scales with the bin size, and so it is important to define some standard in noise floor analysis. Noise floors are referenced to 1Hz binning. These are known as power ($\frac{V^2}{Hz}$) or amplitude spectral *densities* ($\frac{V}{\sqrt{Hz}}$). This gives rise to the $\frac{1}{\sqrt{Hz}}$ in the unit of sensitivity for magnetometers, defining that the sensitivity was measured using 1Hz binning. It allows for comparison of different magnetometers without the need to consider the averaging time. Using a smaller bin size can also be thought of as averaging for longer, which would of course reduce white noise. An example of noise floor scaling with bin size is shown

in Figure 1.1, where the sampling frequency was kept constant but the signal acquired for different lengths of time.

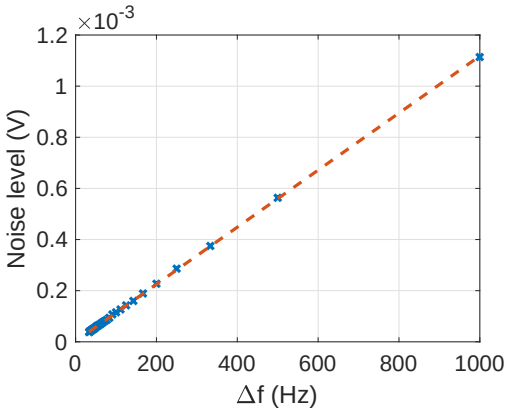

Figure 1.1: Noise floor measured as an average around the RF frequency used in magnetometry against the FFT bin size (Δf). Data (blue crosses) with a linear fit (red dashed line) show the reduction in noise as the bin size decreases.

Zero padding describes adding zeros to the end of a signal array to increase the amount of points, or length, of the signal thereby artificially giving finer steps (resolution) in frequency of an FFT. This can be very useful, but must be considered carefully. The minimum spacing between two frequencies that can be resolved does not change with zero padding, this is inherent to the actual data taken. However, by adding zero padding we can centre bins more effectively on the frequency we are trying to measure. An effect of the bin centring can be seen in Figure 1.2. Here, a 30 ms oscillating signal is cut, changing the bin size. The sawtooth pattern arises in the SNR from the change in bin centring on the frequency of the signal. Once zero padding is added to maintain 1Hz binning at all cut times, the sawtooth pattern is no longer seen and the expected increase in SNR with more signal sampled is seen. This confirms that with the short measurement times in the ultracold atom implementation of the radio-frequency magnetometer, we must be careful with the frequencies we choose to interrogate.

AC Sensitivity refers to detection of a field oscillating at frequency ω. In this case, even if we do not scan frequency space for a resonance, the magnetometer can simply output a response at a set frequency. We must calibrate this response, using a calibration field, to be able to determine the magnitude of an unknown field oscillating

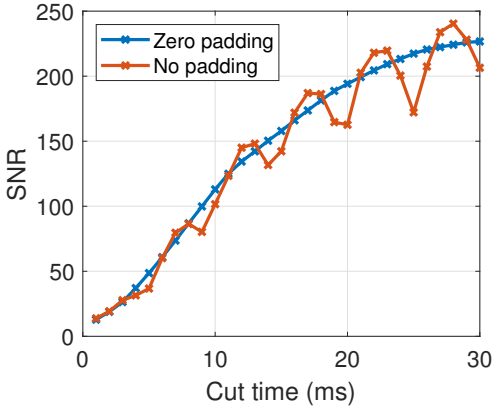

Figure 1.2: Bin centring effect on SNR. A signal oscillating at an integer frequency is sampled for different lengths of time (by changing the 'cut time'). With constant sampling frequency, this changes the bin size, seeing points of better and worse bin centring in frequency space. With added zero padding, 1 Hz binning sees a bin at each integer frequency, removing the problem of bin centring.

at this frequency. Calibration allows for conversion of the noise floor from voltage to magnetic field. This will define our AC sensitivity, written as

$$\delta B_{AC} = N\frac{B_{RF}}{S} = \frac{B_{RF}}{\frac{S}{N}} = \frac{B_{RF}}{SNR}, \tag{1.3}$$

where N is the noise level, S is the signal level, SNR is the signal to noise ratio and B_{RF} is the strength of the calibration field at the sensor. Figure 1.3 shows a typical FFT of the polarimeter signal acquired. A calibration field of 11 nT corresponded to 0.32 mV in the FFT. This defines our conversion factor $\frac{B_{RF}}{S}$ in units of $\frac{T}{V}$, which is used to plot a calibrated response. The noise figure used must be an amplitude spectral density, to be consistent with the previously described convention, and so has units of $\frac{V}{\sqrt{Hz}}$, giving sensitivity units of $\frac{T}{\sqrt{Hz}}$.

DC Sensitivity considers the efficiency with which the magnetometer can determine the bias field magnitude. This can also be thought of as what is the smallest detectable shift in the bias field that can be measured. Both pictures require a determination of the resonant frequency of the system, linked to the bias field through γ, the gyromagnetic ratio. The resonant frequency is most easily described by the dispersive response of the magnetometer, plotted in Figure 1.4, where the signal passes through zero at resonance. The dispersive gradient, when plotting voltage against frequency,

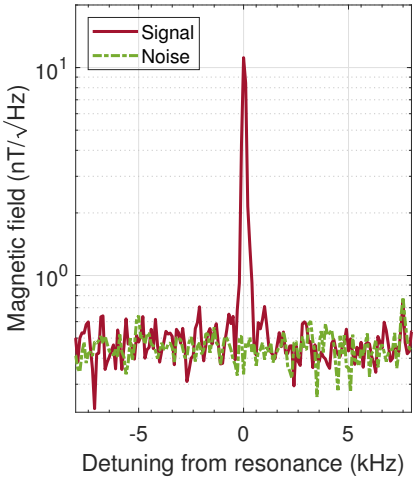

Figure 1.3: Example FFT output from the magnetometer, used to illustrate sensitivity calculations. A calibration field of 11 nT produces a signal height of 0.32 mV. This is used to convert the noise floor to magnetic units.

can be written as

$$\frac{dV}{df} = \frac{S}{\Gamma} \tag{1.4}$$

where S is the signal height and Γ is the full width at half maximum (FWHM) of the resonance. Moving to angular frequency

$$\frac{dV}{d\omega} = \frac{1}{2\pi}\frac{dV}{df}, \tag{1.5}$$

and by noticing that

$$\frac{dV}{d\omega} = \frac{1}{\gamma}\frac{dV}{dB} \tag{1.6}$$

the gradient can indeed be used to convert the noise floor N (units $\frac{V}{\sqrt{Hz}}$) to magnetic units (conversion factor $\frac{dB}{dV}$). We can write

$$\delta B_{DC} = N\left(\frac{dV}{dB}\right)^{-1} = \frac{2\pi}{\gamma}\frac{\Gamma}{SNR}, \tag{1.7}$$

defining our DC sensitivity, units $\frac{T}{\sqrt{Hz}}$ [48] [64]. Just as before, the noise N is converted to magnetic units, but this time by considering the slope of the quadrature response rather than a calibration field.

sensitive

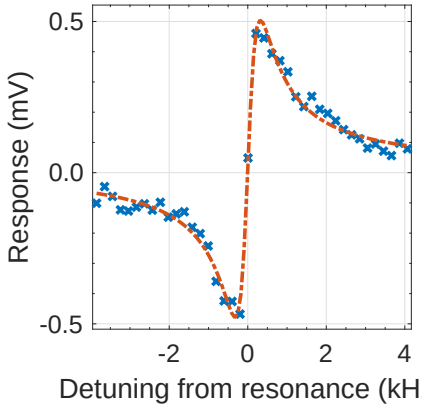

Figure 1.4: Example lock-in amplifier dispersive response of the magnetometer. Data (blue crosses) and fit (red dashed line) extract a resonant frequency and linewidth from the magnetometer's response. These are used to determine the bias field magnitude and define the DC sensitivity.

A simulation of the magnetometer working in two respective regimes is shown in Figure 1.5. In the AC detection regime, the bias field magnitude (B_0) is swept with the radio-frequency field held constant. By calibrating the response the radio-frequency field magnitude is determined. An example of two different radio-frequency field magnitudes is shown in the figure. Conversely, in the case of DC field detection, the magnetometer's bias field is constant and the radio-frequency is swept. Resonant frequency determination allows for bias field magnitude extraction.

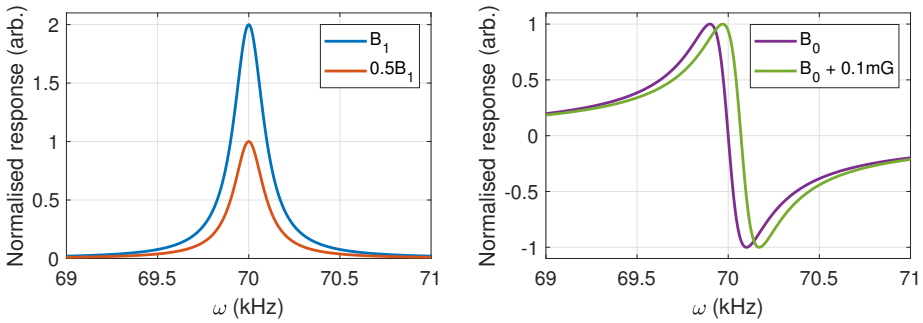

Figure 1.5: Simulated magnetometer response for different working conditions. On the left, the strength of the RF field (B_1) is halved, giving half the signal in the magnetometer response. This is the magnetometer working in the AC configuration. On the right, the bias field (B_0) strength is changed, leading to a change of resonant frequency, where the magnetometer is working in the DC configuration.

1.2.3.1 Fundamental limits

It is useful to consider the general fundamental limits on sensitivity, which ignore the specifics of the system, to be able to compare different types of magnetometers. Following the arguments presented in reference [41], the spin noise limit can be written as

$$\delta B_{spn} \approx \frac{1}{\gamma}\frac{1}{\sqrt{N\tau T}}, \tag{1.8}$$

where γ is the gyromagnetic ratio, N is the number of atoms, T is the measurement time and τ is the coherence time of the state. This merely considers that for a measurement of the Larmor precession angle, we can improve our measurement with N atoms by $\sqrt{N}$ whilst also repeating the measurement, gaining a factor of $\sqrt{T/\tau}$ (equal to the number of repetitions). Next, with atomic magnetometers using probe beams to read out spin precession, the photon shot noise can be written as

$$\delta B_{psn} \propto \delta\phi \approx \frac{1}{2\sqrt{\Phi_{ph}T}}, \tag{1.9}$$

where Φ_{ph} is the probe photon flux and $\delta\phi$ is the uncertainty in the rotation angle of the probe beam. Clearly the photon flux multiplied by the measurement time gives the total number of photons. Again, the uncertainty in the measurement scales with the number of measurements made as in the spin projection noise. Depending on the specifics of the system, either noise sources may dominate. When the experimental parameters are optimised for greatest sensitivity, the two fundamental noises are comparable [65] [66].

1.2.4 Spatial resolution

A major strength of an ultracold magnetometer is its small sensing volume. Considering a case where the magnetometer is used for imaging, the smaller the sensing volume, the better theoretically achievable spatial resolution. This is not always true, as the ability to place the sensor near to the sample of interest can also limit resolution.

In general, the sensitivity of a magnetometer scales with probe volume, due to the fundamental limits in sensitivity scaling with number of probed atoms, which can be related to volume through the density of the medium. A small survey of previously

achieved magnetometer sensitivities at different probe volumes is shown in Figure 1.6. Only AMs, BEC, NV and SQUID magnetometers are plotted as these are the current state-of-the-art and are actively researched. It is clear BEC magnetometers provide a path to micrometer resolution.

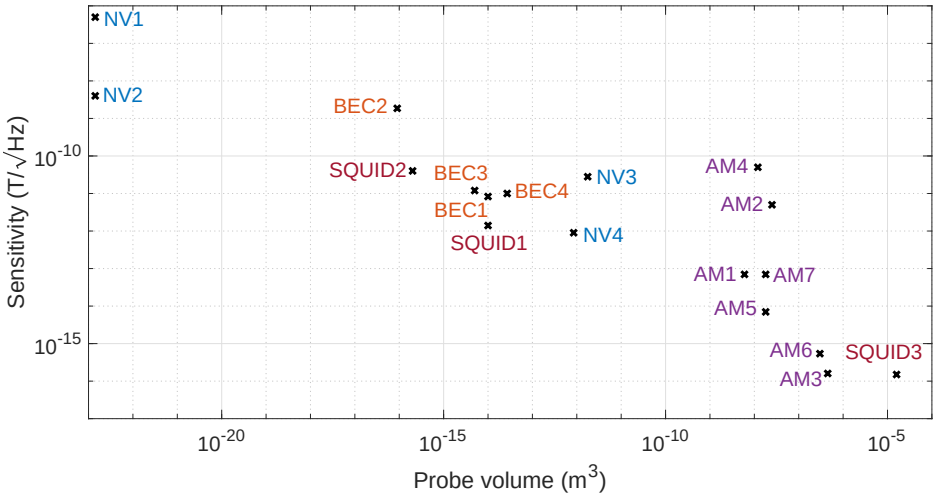

Figure 1.6: Sensitivity against probe volume plotted for a variety of magnetometers. Atomic and SQUID magnetometers perform the best in terms of absolute sensitivity. To exploit AM's sensitivity for higher spatial resolution measurements ultracold atoms are suggested as atomic mediums instead of buffer-gas cells. **NV(1-4)** [67, 68, 69, 70], **AM(1-7)** [28, 71, 42, 72, 73, 40, 74] **SQUID(1-3)** [75, 76, 35] **BEC(1-4)** [53, 77, 78, 79]

Considering density, NV centres see densities as high as $1 \times 10^{18}\,\mathrm{cm}^{-3}$ [70, 80]. Vapour cell magnetometers can increase their density by heating of such cells. A plot of the expected density in the buffer gas cell as a function of temperature is shown in Figure 1.7, discussed further in reference [81]. Most atomic magnetometers therefore heat buffer cells to increase density, thereby improving sensitivity. Increasing density in atomic magnetometers is not without limit, as at some point the collisions between alkali-metals begin to dominate the spin relaxation time, causing $N\tau$ to approach a constant value. This is the limit which is circumvented in SERF magnetometry, allowing densities as high as $1 \times 10^{14}\,\mathrm{cm}^{-3}$ to be explored ($\sim$4 orders of magnitude higher than non-SERF atomic magnetometers). The SERF regime is not useful for applications such as EMI as it requires very small bias fields. Furthermore, vapour cell magnetometers cannot exceed spatial resolutions better than the diffusion length

in one spin coherence time (∼mm). This work focuses on an alternative to vapour

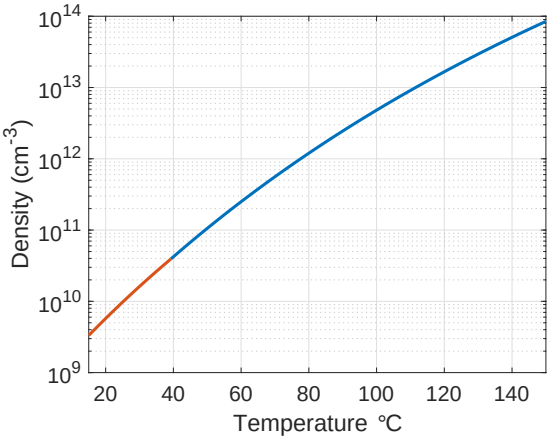

Figure 1.7: Atom density of ^{87}Rb in a vapour cell as a function of temperature.

cells, an ultracold atomic sample in ultra-high vacuum, which can maintain coherence times at higher densities and control sensor size down to μm [53] [54] [55] [56]. Although not competitive in absolute sensitivity due to the much smaller overall number of atoms, the increase in density (up to $1 \times 10^{15}\,\mathrm{cm}^{-3}$ [82] with potential coherence times on the order of 300 s [83]), suppression of thermal diffusion, and increase in atomic control can pull previously achieved vapour cell EMI into the micro meter regime. Furthermore, suggestion of the BEC maintaining coherent precession even in small magnetic field gradients could further increase sensitivity at micrometer length scales [54]. Finally, BECs are well positioned to improve on classical measurement schemes, exploiting better scaling with number of atoms in quantum enhanced measurement techniques [84] via entanglement [85] or atomic spin squeezing [86], although these are out of the scope of this thesis.

In addition, Figure 1.6 does not discuss the operational frequency of each magnetometer (ranging from DC-MHz). With the previous comments on other properties of magnetometers, it is clear a direct comparison is difficult, and a multitude of parameters must be considered. Even previously achieved BEC magnetometers vary significantly, with some detection methods not suitable for the application described in this thesis.

1.3 Thesis Outline

Overall, the thesis follows a concepts-apparatus-results-outlook structure, with the cold and ultracold implementations of the RF AM split as they were completed chronologically.

Chapter 2 introduces radio-frequency magnetometry from its basic concepts. Neutral atoms and their spins are discussed, with the response to electric and magnetic fields described. Next, the output from a radio-frequency magnetometer is predicted and explained via the Bloch equations.

Chapter 3 briefly explains laser cooling before focusing on evaporation in magnetic and dipole traps. These allow for a Bose-Einstein condensate to be created, and so concepts required for understanding and observing a BEC are discussed.

Chapter 4 describes the experimental apparatus built to achieve the initial cold atom magnetometer. Most of the apparatus is linked to achieving only a cold atom setup, although the gradient producing coils which will later become a magnetic trap are also discussed.

Chapter 5 reports on the cold atom magnetometer's results, which are published in reference [1]. Optimisation and characterisation of the sensor is described, with the sensitivity, atom number response and frequency operational range defined.

Chapter 6 presents the apparatus required for production of a BEC, and the necessary upgrades made to the cold atom setup to achieve radio-frequency magnetometry with ultracold atoms. The evaporation optimisation is detailed and improvements such as offline phase sensitive detection and bias field stabilisation are described.

Chapter 7 discusses the ultracold magnetometer's results, with the sensor characterised at both its most sensitive and smallest probe volume (in the BEC). A comparison of the magnetometer's performance throughout the evaporation sequence is presented, before initial conductivity sensing measurements are made.

Chapter 8 summarises and concludes the thesis, discussing the outlook of the work presented and the next steps for the project.

Chapter 2

RF Magnetometer - Concepts

This chapter will explore theoretical concepts which underpin radio-frequency magnetometry. Ideas of spin will be introduced, to predict the behaviour of atomic species when interacting with both magnetic fields and light.

2.1 Rubidium 87

Alkali atoms, with their one valence electron, provide an electronic structure suitable for trapping and magnetometry. Such an electron defines the optical properties of alkalis. It has spin angular momentum **S** and orbital angular momentum **L**. Consider the ground state of this electron, where L = 0 and S = $\frac{1}{2}$. Transitions out of the ground state to higher values of L are possible. However, due to the coupling between **L** and **S**, a perturbation of these energy levels is produced. This is known as the fine structure, and is defined by the total electronic angular momentum, **J**, given by

$$\mathbf{J} = \mathbf{L} + \mathbf{S}, \tag{2.1}$$

where the values of **J** must be in the range

$$|L - S| \leq J \leq L + S. \tag{2.2}$$

For L = 1 S = $\frac{1}{2}$, there are two possible values of J, $\frac{1}{2}$ or $\frac{3}{2}$. Hyperfine structure arises because of coupling of **J** with the total nuclear angular momentum **I**. The total atomic

angular momentum, **F**, is given by

$$\mathbf{F} = \mathbf{J} + \mathbf{I}, \tag{2.3}$$

with the energy shift due to the hyperfine splitting

$$\delta_i = \frac{AK}{2} + B\frac{\frac{3}{2}(K^2+1) - 2I(I+1)J(J+1)}{2I(2I-1)2J(2J-1)}, \tag{2.4}$$

where K is

$$K = F(F+1) - I(I+1) - J(J+1). \tag{2.5}$$

The hyperfine splitting sees two contributions, magnetic dipole and electric quadrupole, terms A and B in Equation 2.4 respectively. Figure 2.1 shows an energy level diagram for the outer electron of ^{87}Rb. Both D1 and D2 lines are shown, corresponding to a transition of the outer electron from $5^2S_{1/2}$ to $5^2P_{1/2}$ and $5^2P_{3/2}$ respectively.

2.2 Zeeman splitting

Previous splitting has been caused internally in the atom, but external fields can induce further splitting. Firstly, an interaction with DC magnetic fields sees Zeeman splitting. For weak fields, where F is still a good quantum number, there are 2F+1 magnetic sublevels, split linearly by

$$\Delta E_z = \mu_b g_F m_F B_z \tag{2.6}$$

where the field is taken to be along the $\hat{\mathbf{z}}$ direction, μ_b is the Bohr Magneton, g_F is the Landé g-factor for the F level being considered, and m_F labels the different sublevels. For stronger fields the splitting is no longer linear, and the atoms enter the Paschen-Back regime. For the ground states of the ^{87}Rb, the splitting can be well described by the Breit-Rabi formula which is used and plotted in Figure 2.2 [81].

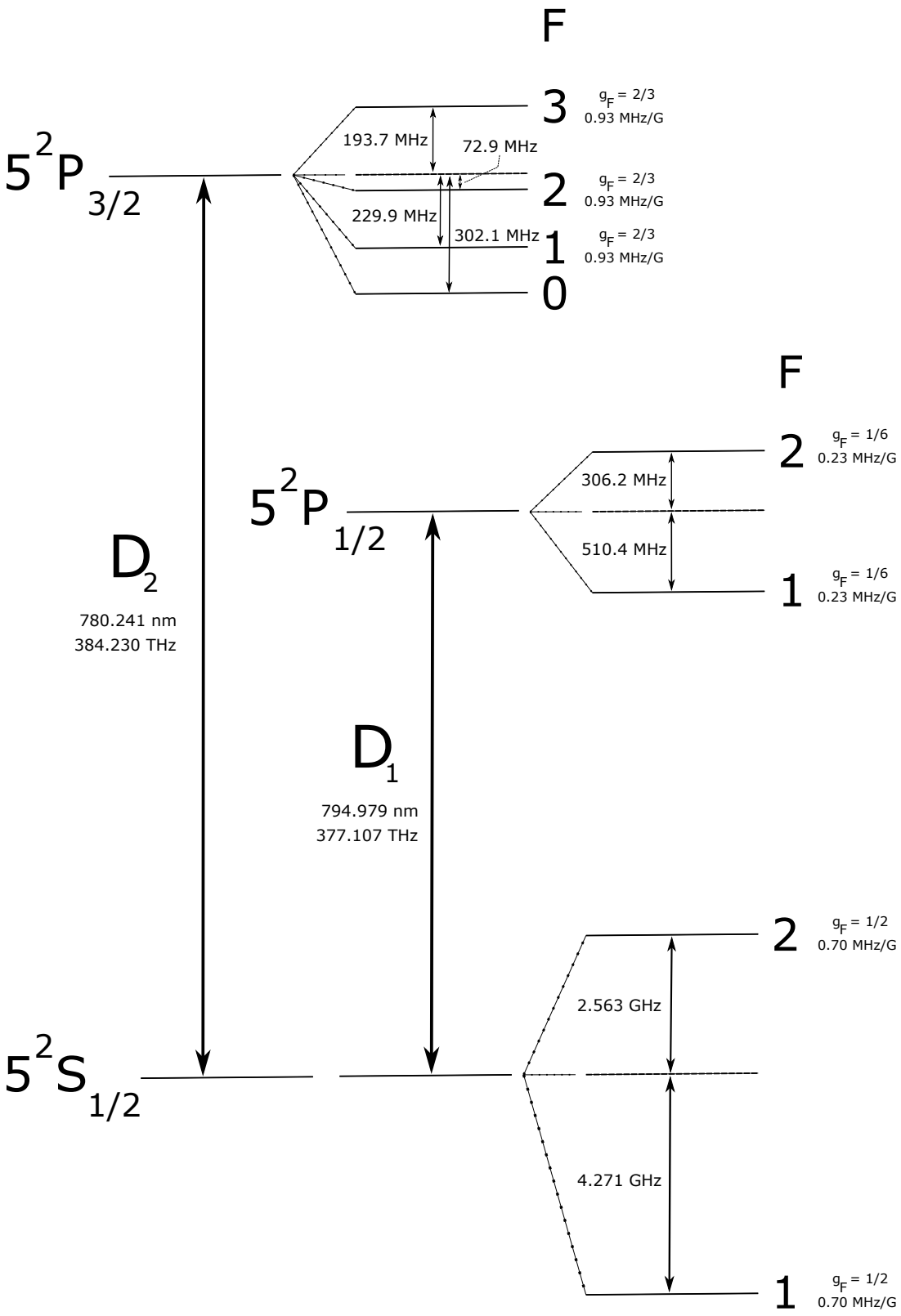

Figure 2.1: Energy levels diagram for ^{87}Rb, showing both the D1 and D2 lines.

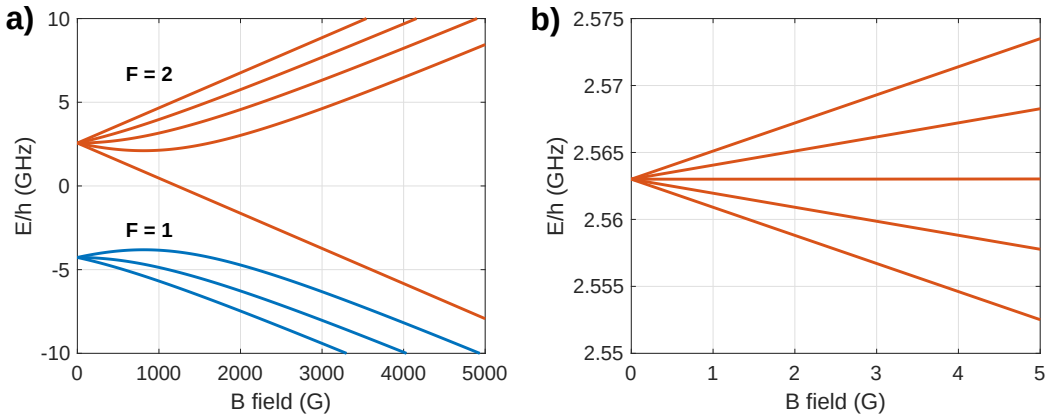

Figure 2.2: Zeeman splitting for the ground states of ^{87}Rb. Part a) shows the splitting as extended to the high-field regime, which is relevant for applications such as magnetic trapping or high frequency magnetometry. Part b) shows the low-field regime, where the splitting is linear.

2.3 Bloch Equations

The magnetometer response can be described by the classical Bloch equations. These consider magnetic resonance of a weak RF field perpendicular to a strong bias field, which in the case of the 1946 paper by Bloch [87], is read out via an induced voltage in a pickup coil. Although often described as phenomenological and heuristic, not truly explaining the underlying process, the predictions provided by this theory correspond well to the observed phenomena [88]. Furthermore, they give an intuitive understanding of the system, which can sometimes be hidden by the complications of the quantum mechanical picture.

Classically, a magnetic moment **M**, in an applied field **B**, feels a torque aligning the moment vector to the field vector. Torque can be written in terms of the rate of change of angular momentum, **I**,

$$\mathbf{T} = \frac{d\mathbf{I}}{dt}. \tag{2.7}$$

The total magnetic moment of an ensemble of atoms, **M**, in terms of the total angular momentum of the atoms, **I**, is given by

$$\mathbf{M} = \gamma \mathbf{I} \tag{2.8}$$

where γ is a constant conversion factor, the gyromagnetic ratio. The torque felt by the

atoms is also the cross product of the magnetic moment vector and the applied field vector **B**,

$$\mathbf{T} = \mathbf{M} \times \mathbf{B}. \tag{2.9}$$

Combining 2.7, 2.8, and 2.9 gives the equation of motion for this system of free spins

$$\frac{d\mathbf{M}}{dt} = \gamma \mathbf{M} \times \mathbf{B}. \tag{2.10}$$

In order to solve equations of motion such as the Bloch equation, it is useful to move from the lab frame into a frame which rotates at some angular velocity ω. We can write this transformation for the time dependent vector **M**, in the lab frame, as

$$\frac{d\mathbf{M}}{dt} = \frac{\delta \tilde{\mathbf{M}}}{\delta t} + \omega \times \mathbf{M}, \tag{2.11}$$

where $\frac{\delta \tilde{\mathbf{M}}}{\delta t}$ is the rate of change of the vector in the rotating frame. The notation for the rotating frame will be the same for all vectors, to be clear as to when we are considering vectors in the laboratory or rotating frame. Comparing this with the equation of motion for free spins (2.10), we can write

$$\frac{\delta \tilde{\mathbf{M}}}{\delta t} = \gamma \mathbf{M} \times (\mathbf{B} + \frac{\boldsymbol{\omega}}{\gamma}), \tag{2.12}$$

where the anticommutativity of the cross product has been used. We can now replace **B** with an effective field, $\mathbf{B_e}$, which is the sum of the field in the laboratory frame and a fictitious field ($\mathbf{B_e} = \mathbf{B} + \frac{\boldsymbol{\omega}}{\gamma}$). Setting the applied field in the lab frame to $\mathbf{B_0}$ and choosing a rotating frame $\boldsymbol{\omega} = -\gamma \mathbf{B_0}$, it is clear that $\frac{\delta \tilde{\mathbf{M}}}{\delta t} = 0$. In other words, the magnetic moment is static in the rotating frame, and so must be precessing in the laboratory frame. The frequency of this precession is the Larmor frequency associated with this field.

Building on this, setting the field along the z direction ($\mathbf{B} = B\hat{\mathbf{z}}$) we can consider the system trending towards some equilibrium value of magnetisation, with its $\hat{\mathbf{z}}$

component $M_z = M_0$. Writing an equation of motion for this

$$\frac{dM_z}{dt} = -\frac{M_z - M_0}{T_1} \tag{2.13}$$

where T_1 is labelled the longitudinal relaxation time. If the magnetisation is given a component in the perpendicular direction to the bias field, such as an RF field along the $\hat{\mathbf{x}}$ or $\hat{\mathbf{y}}$ directions, then the transverse magnetisation will decay in the following way,

$$\frac{dM_i}{dt} = -\frac{M_i}{T_2}, i = x, y, \tag{2.14}$$

with T_2 describing the transverse relaxation time. Finally, assuming that the motion due to the relaxation can be combined with the motion of free spins (2.10,2.13 and 2.14), the overall Bloch equation is

$$\frac{d\mathbf{M}}{dt} = \gamma \mathbf{M} \times \mathbf{B} - \frac{M_x \hat{\mathbf{x}} + M_y \hat{\mathbf{y}}}{T_2} - \frac{M_z - M_0}{T_1} \hat{\mathbf{z}}. \tag{2.15}$$

Considering now the experiment at hand, an ensemble of atoms are placed in a bias magnetic field, along $\hat{\mathbf{z}}$, with an oscillating field perpendicular to it, along $\hat{\mathbf{x}}$. The perpendicular field ($\mathbf{B_1} = 2B_1 cos(\omega t)\hat{\mathbf{x}}$) can be split into two counter rotating fields. When moving to a frame rotating with one of these fields, we can use the rotating wave approximation (valid near resonance) to neglect the counter rotating term, writing the field in this frame as $\tilde{\mathbf{B}}_\mathbf{1} = B_1 \hat{\tilde{\mathbf{x}}} = \frac{\omega_1}{\gamma} \hat{\tilde{\mathbf{x}}}$. The effective field, static in the rotating frame, can be written as

$$\tilde{\mathbf{B}}_\mathbf{e} = (B_0 + \frac{\omega}{\gamma}) \hat{\tilde{\mathbf{z}}} + B_1 \hat{\tilde{\mathbf{x}}} = \frac{1}{\gamma} (\Delta\omega \hat{\tilde{\mathbf{z}}} + \omega_1 \hat{\tilde{\mathbf{x}}}). \tag{2.16}$$

where $\Delta\omega = (\omega_0 - \omega)$, and ω_0 is the resonant frequency set by the bias field B_0 ($B_0 = \frac{\omega_0}{\gamma}$). Rewriting the Bloch equation of motion in the rotating frame

$$\frac{\delta \tilde{\mathbf{M}}}{\delta t} = \gamma \tilde{\mathbf{M}} \times \tilde{\mathbf{B}}_\mathbf{e} - \frac{\tilde{M}_x \hat{\tilde{\mathbf{x}}} + \tilde{M}_y \hat{\tilde{\mathbf{y}}}}{T_2} - \frac{M_z - M_0}{T_1} \hat{\tilde{\mathbf{z}}}, \tag{2.17}$$

leading to

$$\begin{pmatrix} \frac{\delta \tilde{M}_x}{\delta t} \\ \frac{\delta \tilde{M}_y}{\delta t} \\ \frac{\delta M_z}{\delta t} \end{pmatrix} = \begin{pmatrix} -\frac{\tilde{M}_x}{T_2} + \Delta\omega \tilde{M}_y \\ -\Delta\omega \tilde{M}_x - \frac{\tilde{M}_y}{T_2} - \omega_1 M_z \\ \omega_1 \tilde{M}_y - \frac{M_z - M_0}{T_1} \end{pmatrix}. \tag{2.18}$$

The general solution is one with decaying exponentials and a steady state solution. Assuming enough time has passed for the exponentials to have decayed, the steady state is found by setting $\frac{\delta \tilde{M}_x}{\delta t} = \frac{\delta \tilde{M}_y}{\delta t} = \frac{\delta M_z}{\delta t} = 0$, leading to,

$$\begin{aligned} \tilde{M}_x &= \frac{\Delta\omega\gamma B_1 T_2^2}{1 + (T_2\Delta\omega)^2 + \gamma^2 B_1^2 T_1 T_2} M_0, \\ \tilde{M}_y &= \frac{\gamma B_1 T_2}{1 + (T_2\Delta\omega)^2 + \gamma^2 B_1^2 T_1 T_2} M_0, \\ M_z &= \frac{1 + (T_2\Delta\omega)^2}{1 + (T_2\Delta\omega)^2 + \gamma^2 B_1^2 T_1 T_2} M_0. \end{aligned} \tag{2.19}$$

Moving back to the non rotating laboratory frame, we have the simple relations

$$\begin{aligned} M_x &= \tilde{M}_x \cos(\omega t) - \tilde{M}_y \sin(\omega t) \\ M_y &= \tilde{M}_y \cos(\omega t) + \tilde{M}_x \sin(\omega t) \end{aligned} \tag{2.20}$$

illustrated in Figure 2.3.

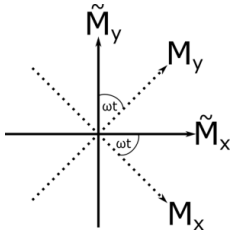

Figure 2.3: Rotating frame transformation from the frame rotating with the drive field ($\tilde{M}_x, \tilde{M}_y$ fixed axes) back to the lab frame (M_x, M_y rotating at ωt).

2.4 Optical Pumping

Efficient initial atomic spin polarisation is achieved via optical pumping. The RF magnetometer signal is proportional to this initial polarisation. Optical pumping is illustrated in Figure 2.4, with a two level atom in a bias magnetic field in the $\hat{z}$ direction. Circularly polarised light, tuned to the ^{87}Rb $5^2S_{1/2}, F = 2 \rightarrow 5^2P_{3/2}, F' = 3$

transition and also along $\hat{z}$, can only drive transitions with $\Delta m_F = \pm 1$, due to the angular momentum of the photon. With just $\sigma+$ light, any state apart from the $m_F = +F$ is immediately depopulated. Once in this state, a cycling transition with short excited state lifetimes ensures the atomic cloud stays in $m_F = +F$.

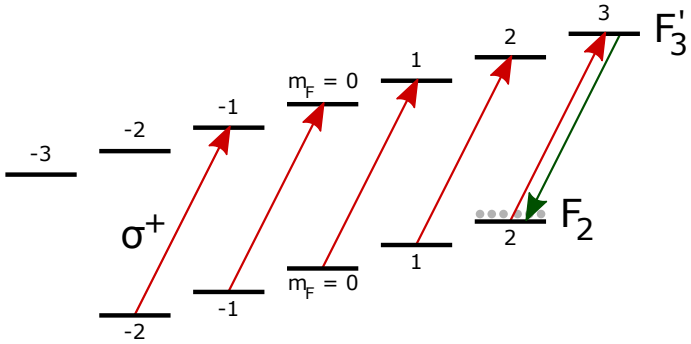

Figure 2.4: Spin polarisation of ^{87}Rb atoms via optical pumping on the D2 line. Atoms in a bias field undergo Zeeman splitting of their m_F sub-levels. Circularly polarised light, in the same direction as the bias field, drives $\Delta m_F = +1$ transitions, leading to accumulation of atoms in the $|F = 2, m_F = +2\rangle$ state.

2.5 Polarisation Rotation

Detection of spin polarisation precession is achieved via polarisation rotation of a linearly polarised probe beam. The linear polarised probe can be split into two counter rotating $\sigma\pm$ components, which see different refractive indices in the circularly birefringent atomic media consisting of polarised atomic spins. For radio-frequency magnetometers the angle of polarisation rotation, ϕ, for a probe beam propagating along $\hat{\mathbf{y}}$ is often written as

$$\phi = \frac{1}{2} l r_e c f n P_y D(\nu) \tag{2.21}$$

where l is the length of propagation in the atomic sample, r_e is the classical electron radius, c is the speed of light, f is the oscillator strength for the relevant transition, n is the density of the medium, $D(\nu)$ is the dispersion profile of the transition and P_y is the degree of spin polarisation (simply $\frac{M_y}{|\mathbf{M}|}$) [65]. For a cold atom magnetometer, the polarisation of the probe beam will be modulated at the precession frequency, decaying as the spin precession de-phases or the atoms leave the probing region. The polarisation angle of the probe can be read out with a polarimeter, consisting of a

polarising beam splitter (PBS) and balanced photodiode. The response in volts of the polarimeter will be directly proportional to the angle of rotation, with a gain factor depending on the specifics of the system.

2.6 Phase sensitive detection

An illustration of a radio-frequency magnetometer is shown in Figure 2.5. Atoms in a bias magnetic field, B_0, are optically pumped by circularly polarised light. A transverse oscillating field B_1 causes coherent spin precession, which is mapped onto the plane of polarisation of a linearly polarised probe beam.

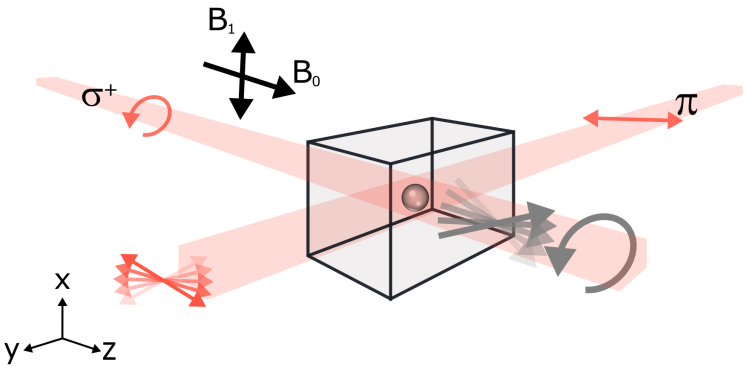

Figure 2.5: Radio-frequency atomic magnetometry. Circularly polarised light and a bias field (B_0) optically pump atoms. Coherent precession is driven with an oscillating field (B_1), leading to polarisation rotation of a probe beam.

At this point, it is useful to discuss practical measurements. The RF magnetometer, with the probe beam travelling along the transverse direction $\hat{\mathbf{y}}$, is sensitive to M_y. The resonance is probed by sweeping frequency and measuring the polarimeter response using a lock-in amplifier. These give a phase sensitive response, one output in phase with a reference signal (labelled X) and another out of phase with the same reference signal (labelled Y). We can consider the total signal oscillating at the probed frequency by taking the quadrature sum of the two (labelled R) and the phase of the signal relative to the reference signal by computing arctan(Y/X) (labelled phase or θ).

Considering Equation 2.20, the lock-in amplifier's X,Y outputs correspond to $\tilde{M}_x$ and $\tilde{M}_y$, when the reference phase is set accordingly. As the reference phase can be arbitrarily changed on a lock-in amplifier, it must be adjusted until a symmetric in-phase

and out of phase resonance is attained. This can be thought of as adjusting the laboratory frame, when moving back from the rotating frame. Simply, the measurement can be swapped between M_x and M_y with a $\frac{\pi}{2}$ phase addition. A simulation of the expected lock-in amplifier output using the Bloch equations is shown in Figure 2.6.

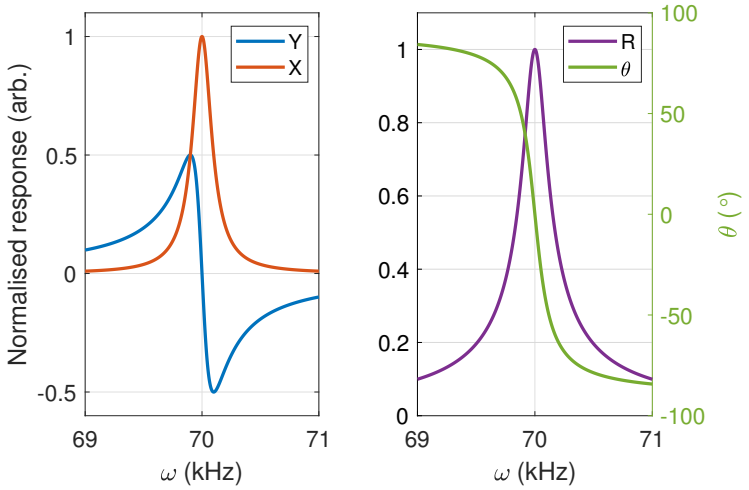

Figure 2.6: The Lock-in amplifier response simulated using the Bloch equations, normalised to the maximum of the in-phase (X) response. The in phase and out of phase (Y) response described is shown on the left, with the right showing a different representation of the same data by considering the total response (R) and the phase (θ).

The Bloch equations perform well when the contribution of spin exchange collisions to the linewidth is small. Deviation of data from Lorentzian fits described by the Bloch equations is obvious when there is considerable RF broadening. A comparison of the Bloch equation performance in such limits can be seen in reference [89], with suggested modifications for improvement of the Bloch equations and a full density matrix formalisation of the phenomena.

Chapter 3

Ultracold atoms - Concepts

The trapping and cooling of neutral atoms, first demonstrated over 25 years ago [90, 91, 92], led to a new field of physics. The progress made in those early years, reviewed in Nobel lectures [93, 94, 95] and other works [96, 97], forms the foundation of this project. Subsequently, phase-space densities (PSD) high enough for Bose-Einstein condensation (BEC) were achieved, first in ^{87}Rb [98] and then closely followed by many other atomic species [99, 100, 101, 102, 103, 104]. This chapter will discuss methods of trapping neutral atoms, with the necessary concepts explored and early implementations of traps summarised. It will then progress to describe a special phase of matter, the Bose-Einstein condensate.

3.1 Laser cooling

Magneto-optical trapping relies on the exchange of momentum between photons and atoms. When acted upon by a laser, atoms absorb and emit photons, where over many cycles they gain momentum in the direction of propagation of the laser. Counter propagating beams, slightly detuned from the resonant frequency of an atomic transition, provide a velocity dependent force, cooling the atoms via Doppler cooling [105]. When a magnetic field gradient is added, a spatially dependent force arises, leading to trapping of neutral atoms. The atoms behave as a damped oscillator, eventually reaching the Doppler limited temperature. We can write the force acting on the atoms as

$$F_{MOT} = -\beta v - \xi r, \tag{3.1}$$

where v is the velocity of the atoms, r is their spatial position and β, ξ contain all constants and parameters of the system. By introducing the lifetime of the excited state used in cooling, τ, and its inverse linewidth, Γ, the Doppler limited temperature can be written as,

$$T_D = \frac{\hbar\Gamma}{2k_B} \tag{3.2}$$

in the low intensity limit at optimal detuning. For ^{87}Rb, T_D is 146 µK. This result can be easily attained by equating the rate of cooling and heating in the MOT, and converting to temperature using the equipartition theorem. This limit was soon improved on with sub-Doppler cooling techniques [106] [107], such as polarization gradient cooling (PGC) [108]. Here, the magnetic field gradient is removed, so only the cooling beams are felt by the atoms. With counter propagating beams, a spatially varying polarisation is seen by the atoms. As the atoms move in this field, they are optically pumped into different states. Each optical pumping cycle also sees a small difference between the frequency of absorbed and emitted light, leading to a net loss of energy for the atom. This cooling mechanism works over a much narrower velocity range and does not spatially confine the atoms, and so many cold atom experiments start with a MOT before moving to a PGC mechanism [109]. The temperature limit here is described by the momentum imparted on the atom due to absorption of a photon, written as

$$T_{recoil} = \frac{\hbar^2 k^2}{2Mk_B}, \tag{3.3}$$

where M is the mass of the atom, and k is the photon angular wavenumber. For ^{87}Rb, T_{recoil} is 362 nK. Combination of laser cooling techniques with evaporative cooling allowed circumventing of the mentioned fundamental limits, leading to observation of Bose-Einstein condensation. Evaporative cooling techniques are described next.

3.2 Evaporative cooling

Evaporative cooling is often compared to blowing on a hot cup of tea, whereby the hottest atoms are removed from the system to achieve a new system whose average temperature is lower than the original system. In this context, atoms are a finite resource used to reduce the temperature of the system [110]. We start by considering

an ensemble of atoms in a Boltzmann distribution, with average temperature T and energy E, where $E = k_b T$. A cut is made into the distribution at a multiple of the average energy. We define this energy to be $E_{cut} = \eta k_b T$, where η is the truncation parameter. For $\eta > 1$, after some time dictated by the rate of elastic ('good') collisions between the atoms, a new Boltzmann distribution is formed with a reduced average energy. Cooling of the atomic ensemble is therefore achieved. An interesting thought experiment can be performed, considering the most efficient evaporation possible. Theoretically, we could set E_{cut} to be infinitely high, and wait an infinitely long time for a single atom to be removed (as the probability of the atom being at a very high energy falls exponentially), carrying away almost all the energy of the system. This, of course, is not practical, as there are other sources of losses in the trapped atom systems apart from the evaporation, namely inelastic ('bad') collisions. Efficient runaway evaporation must therefore be optimised to the specifics of the system, where the 'bad' loss rate dictates the optimal rate of change of the cut energy. Evaporation in a magnetic trap can be performed using a RF knife, where the potential depth does not need to be lowered, maintaining the rate of elastic collisions between atoms. In the dipole trap, evaporation occurs by lowering the potential depth.

3.2.1 Magnetic trapping

Magnetic trapping relies on the interaction of an atom's magnetic moment, $\boldsymbol{\mu}$, with an external magnetic field, $\mathbf{B}$. The atom has energy U_B, where

$$U_B = -\boldsymbol{\mu} \cdot \mathbf{B}. \tag{3.4}$$

This can be rewritten as

$$U_B = \mu_b g_F m_F |\mathbf{B}|, \tag{3.5}$$

simply the Zeeman splitting of the atom's magnetic sublevels. With the potential proportional to the absolute value of the magnetic field, $|\mathbf{B}|$, a gradient of magnetic field can be used to levitate atoms against the potential due to gravity [111] and confine them spatially. Practically, magnetic field gradients are often provided by a quadrupole

field, which can be estimated to first order as

$$B = b' \sqrt{\frac{x^2}{4} + \frac{y^2}{4} + z^2}, \tag{3.6}$$

where b' is the gradient provided along the axial direction of the coils. Combining Equations 3.5 and 3.6, the potential surface can be plotted at $z = 0$, seen in Figure 3.1. Clearly, atoms in the $m_F = -2$ state see a repulsive potential, whilst

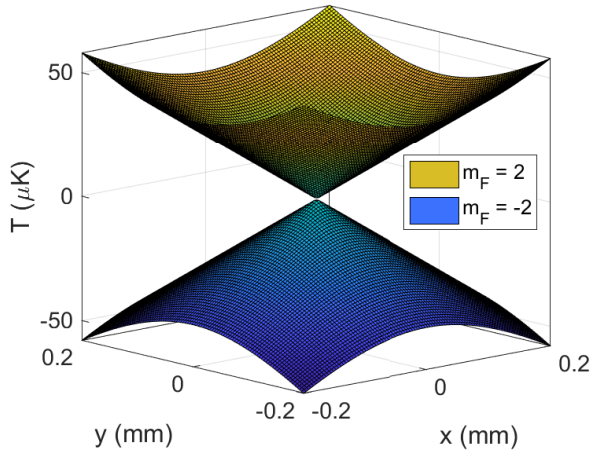

Figure 3.1: Surface of the potential due to the magnetic trap at $z = 0$ for 2 magnetic sublevels of the $|F = 2\rangle$ ^{87}Rb state. Atoms in the $|F = 2, m_F = 2\rangle$ are trapped, whereas atoms in the $|F = 2, m_F = -2\rangle$ are repelled.

atoms in the $m_F = +2$ state are trapped. States which can be trapped by a potential minimum are described as low field seeking states, of which ^{87}Rb has 3 ($|F = 1, m_F = -1\rangle, |F = 2, m_F = +1, +2\rangle$). Considering the response of the state in the high field regime, plotted in Figure 2.2, the $|F = 1, m_F = -1\rangle$ sees an upper limit in useable field before the atoms are lost from the trap. As such, the $|F = 2, m_F = +2\rangle$ is trapped in this experiment, which has no upper limit in field gradient.

Once trapped, atoms can be cooled via radio-frequency evaporation. This describes selectively driving transitions between m_F sublevels of the hotter atoms in the trap. These transitions can be driven with radio-frequency magnetic fields tuned to resonance, set by the magnetic field magnitude. Specifically, for the $|F = 2, m_F = 2\rangle$ state a conversion of magnetic field to frequency is set by its gyromagnetic ratio of 0.7 MHz/G [81]. When the hottest atoms are removed, the remaining atoms rether-

malise at a rate proportional to the trapping frequencies, leaving an overall colder cloud. With the potential symmetry, the hottest atoms are those which spend most time at the outer edges of the trap. By sweeping the radio-frequency of the magnetic field, whilst allowing enough time for the cloud to rethermalise, efficient cooling can be achieved.

Although the quadrupole trap is one of the most efficient in power consumption, giving the tightest traps at the lowest currents, it has one major downfall. As the atoms are cooled in such a trap, they can no longer follow the changing magnetic field (they oscillate in the potential) adiabatically [112]. This leads to spin flips when an atom suddenly sees a magnetic field pointing in the opposite direction after passing the zero point of magnetic field. These spin flips are labelled Majorana flops, and are the fundamental limit in efficient evaporation in magnetic traps which contain a magnetic field zero. The condition for adiabaticity is that the Larmor frequency must be greater than the rate of change of the magnetic field direction [113].

Many solutions have been developed to overcome this catastrophic loss from the trap. Some of the early solutions which eventually led to pioneering observations of Bose-Einstein condensation [114] included a time-averaged potential [112] (labelled TOP trap) and a laser to 'plug the hole' in the zero magnetic field [115]. Both works led to awarding of the Nobel prize. The TOP trap uses a rotating field, to continuously move the magnetic field zero. When time averaged, the potential produced is that of a harmonic potential off setted from zero. This type of trap has inherent evaporation, where a bias magnetic field can be used to control the position of the circling magnetic field zero (colloquially referred to as the 'circle of death'). The optical plug was also successful, and indeed showed many more atoms in the BEC than the TOP trap. Here, a laser is used to repel the atoms from the magnetic field zero.

Although both successful, the TOP trap is difficult to work with once the atoms are in the BEC due to the constantly changing potential. The optical plug also suffers from stability issues in the alignment of the plug to the center of the trap, with the authors in reference [115] suggesting just 20 μm misalignment limits the achievable temperature to 50 μK - far from condensation.

Many solutions now involve a Ioffe-Pritchard type trap, originally suggested for plasmas [116] and extended to neutral atoms [117, 118]. These can be described by a radial quadrupole field and an axial parabolic field, with the minimum of the trapping potential being at a non-zero magnetic field. The first implementations use a co-axial circular coils (labelled the 'pinch' coils) and four current carrying wires (labelled 'Ioffe bars'). This configuration suffers from difficulty in aligning the magnetic trap and MOT centres, and so many modifications have been developed which produce a similar trapping potential. These include, but are not limited to, the cloverleaf trap [119], the baseball trap [120, 121], the QUIC trap [122], the biQUIC trap [123] and the racetrack trap [124]. In addition, there are many other types of magnetic traps, which can be loosely grouped into radio-frequency dressed potentials [125, 126, 127, 128] or time-averaged potentials [129, 130, 131, 132].

3.2.2 Dipole trapping

Dipole trapping relies on the electric polarisability of an atom, describing the ability of an electric field to induce a dipole in the atom. An oscillating electric field $\mathbf{E}$ produces an oscillating electric dipole $\mathbf{p}$, written as

$$\mathbf{p} = \alpha \mathbf{E}, \tag{3.7}$$

where α is the complex polarisability. Using the Lorentz oscillator model, solving the equation of motion for the driven oscillator, and introducing the on resonance damping rate, Γ, α can be written as

$$\alpha = 6\pi\varepsilon_0 c^3 \frac{\Gamma/\omega_0^2}{\omega_0^2 - \omega - i(\omega^3/\omega_0^2)\Gamma}. \tag{3.8}$$

where

$$\Gamma = \frac{e^2\omega_0^2}{6\pi\varepsilon_0 m_e c^3}. \tag{3.9}$$

This on-resonance scattering rate corresponds to the natural lifetime of the excited state, and agrees to within a few percent with the experimentally measured decay rate.

This leads to the interaction potential,

$$U_{dipole} = -\frac{1}{2}\langle \mathbf{p}\cdot\mathbf{E}\rangle_t = -\frac{1}{2\varepsilon_0 c}\Re(\alpha)I \tag{3.10}$$

which corresponds to the real part of the polarisability. Considering also the power absorbed by the oscillator, $\langle \dot{\mathbf{p}}\cdot\mathbf{E}\rangle$, the scattering rate can be written as

$$\Gamma_{sc}(\mathbf{r}) = \frac{1}{\hbar\varepsilon_0 c}\Im(\alpha)I(\mathbf{r}) \tag{3.11}$$

corresponding to the imaginary part of the polarisability. Finally, by using the rotating-wave approximation, the potential can be written as

$$U_{dip}(\mathbf{r}) = \frac{3\pi c^2}{2\omega_0^3}\frac{\Gamma}{\Delta}I(\mathbf{r}), \tag{3.12}$$

and the scattering rate as

$$\Gamma_{sc}(\mathbf{r}) = \frac{3\pi c^2}{2\hbar\omega_0^3}\left(\frac{\Gamma}{\Delta}\right)^2 I(\mathbf{r}). \tag{3.13}$$

Visualisation of the fall off of the trap depth and scattering rate with detuning, shown in Figure 3.2, confirms the suitable regime for optimal trapping with minimal heating - a focused far red detuned trap. The oscillator model performs well, but for a full discussion the response to light of a multi level atom must be considered. An interested reader may consult [81, 133, 134] and references therein.

The dipole trap's potential is defined by the intensity distribution of the laser I, which for a focused beam is well described by Gaussian propagation. Defining axial and radial directions, z and r respectively, we can write

$$I = \frac{2P}{\pi w^2(z)}\exp\left(\frac{-2r^2}{w^2(z)}\right) \tag{3.14}$$

where P is the power of the laser, the spot size $w(\mathbf{z})$ is

$$w(z) = w_0\sqrt{1+\left(\frac{z}{z_R}\right)^2}, \tag{3.15}$$

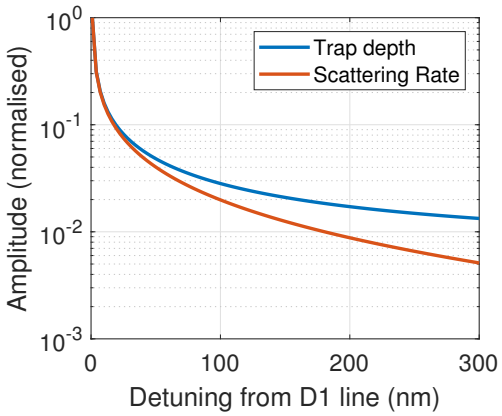

Figure 3.2: Trap depth and scattering rate scaling with red detuning from the D1 line. Both are normalised to their values 1 nm away from resonance.

and z_R is the Rayleigh length, the distance for which the spot size is $\sqrt{2}w_0$, where w_0 is the beam waist at the narrowest point,

$$z_R = \frac{\pi w_0^2}{\lambda}. \tag{3.16}$$

The potential due to one beam is shown in Figure 3.3. It clearly identifies that trapping

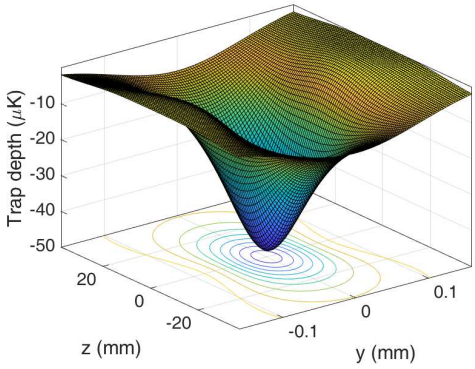

Figure 3.3: Dipole trap formed from a focused laser beam. Power is 5 W, waist is 80 µm, wavelength is 1070 nm giving a calculated Rayleigh length of 19 mm.

in the axial direction is much weaker than that in the radial, as expected. When the thermal energy of the atomic cloud, $k_B T$, is small compared with the potential depth of the dipole trap, the atoms radial and axial extensions are small compared with the beam waist and Rayleigh length ($w_0 \gg \delta r$ & $z_R \gg \delta z$, where $\delta r, \delta z$ are the radial and axial extensions of the cloud). In this regime, we can confidently Taylor expand our

expression for the potential, and deduce the trapping frequencies by comparison with the potential of a harmonic oscillator. These can be simply written as

$$\omega_r = \sqrt{\frac{4U_0}{mw_0^2}} \qquad (3.17) \qquad \omega_z = \sqrt{\frac{2U_0}{mz_R^2}}. \qquad (3.18)$$

To maintain tight trapping and high trapping frequencies in all directions, a crossed dipole trap is often employed, consisting of two focused beam traps. This causes a 'dimple' in the potential, with hotter atoms escaping along the propagation direction of the beams. Forced evaporation in an idealised crossed dipole trap can be visualised in Figure 3.4. Here, the potential is plotted at different intensities of the dipole trap laser. As the intensity of the dipole trap is reduced, so is the trapping depth, leaving only the coldest atoms confined.

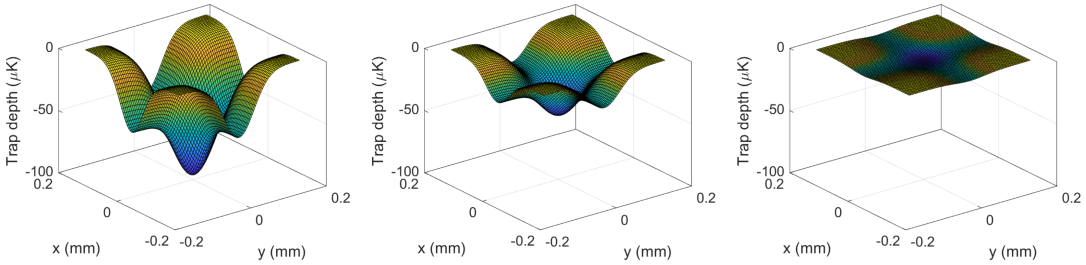

Figure 3.4: Visualisation of forced evaporation. As the dipole trap depth is lowered, only the coldest atoms stay trapped. The beam intensities are reduced from left to right, starting at 100 %, then 50 %, and finally 10 % of the maximum intensity.

The major shortcoming of the optical cross dipole trap is its relative inefficiency, as compared with a quadrupole trap, of loading atoms from the MOT. Past attempts at all optical evaporation to condensation has seen smaller BECs produced [135] [136] [137]. This can be attributed to the small volume and relatively small trap depth, limited by the available laser power, of the dipole trap.

3.2.3 Hybrid Trapping

The hybrid trap, consisting of a dipole 'dimple' superimposed onto a large volume quadrupole magnetic trap [138] exploits the strengths of the individual traps whilst circumventing many of their shortcomings. To recap, atoms can be efficiently transferred from the MOT into the magnetic trap, with minimal losses. The magnetic trap

is robust and simple to implement, as the coils used for the MOT gradient can also be used for the quadrupole trap. Furthermore, this ensures the centres of the two traps are automatically overlapped. Once in this trap, a large gain in PSD is achieved via RF evaporation, where the trapping frequencies can be kept at maximum. As the atoms get colder, and spin flips become the dominant loss term, the atoms are transferred into the dipole trap, with the magnetic field gradient only kept on to levitate the atoms. This transfer moves the potential minimum away from the magnetic field zero, reducing spin flip losses, whilst also gaining in PSD. Many previous implementations of this trap configuration suggests an optimal displacement of one dipole trap beam waist away from the magnetic field zero [139, 140, 141]. In the hybrid potential, forced evaporation to BEC can be performed by lowering of the dipole trap depth. Other techniques, such as tilting of the dipole trap, can also be used [142]. The production of the BEC is now completed in a spin-independent trap (as the levitating field can be switched off) with improved optical access when compared to the coil geometries described in Section 6.1.

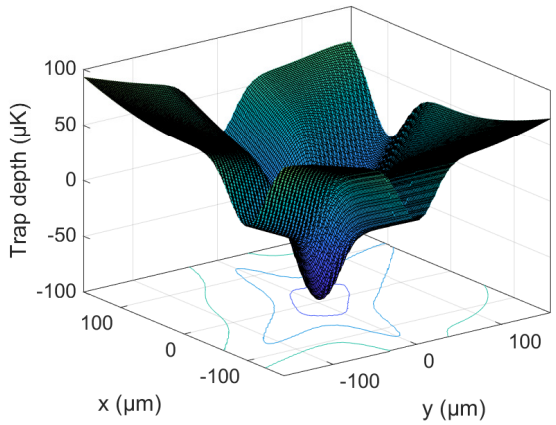

Figure 3.5: Hybrid trapping potential, plotted using the measured values for beam diameters, powers, and magnetic field gradient described in Section 6.

The trapping potential can be visualised in Figure 3.5. The magnetic funnel and dipole 'dimple' can be clearly seen. To match the potential created in the experiment, data reported in Section 6 is used, such as the magnetic field gradient and dipole trap power and beam waist. Furthermore, although ideally the cross dipole trap beams would be orthogonal to each other, to compensate for weaker trapping in the axial di-

rections, experimental limitations mean this can often not be possible. For estimation of the angle between the beams used in this experiment, an absorption image where the potential shape is obvious was used. This is shown in Figure 3.6, where the angle was calculated to be 43.4°.

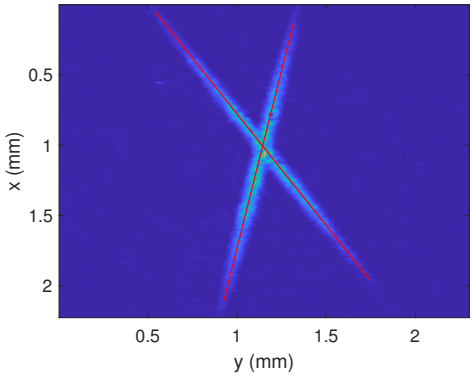

Figure 3.6: Atoms are loaded into the dipole trap with no magnetic field gradient present, producing an image where the dipole trap beams' potential is clearly visible. An estimated angle of 43.4° between the dipole trap beams is calculated from the equations of the red lines.

3.3 Bose-Einstein Condensation

With the combination of laser cooling and evaporative cooling, temperatures low enough for macroscopic ground state population are possible. For integer spin particles (bosons), the atomic ensemble can undergo a phase transition, from a dilute gas (densities $<1 \times 10^{13}\,\mathrm{cm}^{-3}$, compared with $1 \times 10^{19}\,\mathrm{cm}^{-3}$ of air) to a Bose-Einstein Condensate (BEC). Initially, efforts to achieve a BEC focused on liquid Helium. These were hindered by the interactions between atoms, whose effects due to the liquid phase of the atoms was too large. Laser cooled alkali atoms proved to be a much better choice as they stay in the gas phase up until condensation. A more detailed historical overview may be found in [82]. Intuitively, the phase transition occurs when the thermal de Broglie wavelength of the particles, λ_{dB}, is approximately equal to the mean inter-particle separation. The thermal de Broglie wavelength, due to the temperature T of the atoms, is written as

$$\lambda_{dB} = \sqrt{\frac{2\pi\hbar^2}{mk_BT}}. \tag{3.19}$$

The mean inter-particle separation is dictated by the density n of the atomic cloud, leading to the useful parameter which characterises the comparison of the two quantities, the phase-space density (PSD), written as

$$\rho = n\lambda_{dB}^3. \tag{3.20}$$

Indeed, the phase transition occurs when $\rho \approx 1$, or more precisely for an ideal Bose gas $\rho \approx 2.612$.

As the atoms are evaporatively cooled to the BEC, they are held in a potential. In most cases, we can approximate this trapping potential as harmonic, written simply as

$$V(\mathbf{r}) = \frac{1}{2}m(\omega_x^2 x^2 + \omega_y^2 y^2 + \omega_z^2 z^2). \tag{3.21}$$

In such potentials, we consider the geometric mean of the trapping frequencies

$$\omega_{ho} = (\omega_x \omega_y \omega_z)^{\frac{1}{3}}, \tag{3.22}$$

which leads to the characteristic length scale of the system

$$a_{ho} = \sqrt{\frac{\hbar}{m\omega_{ho}}}. \tag{3.23}$$

We will follow the reasoning presented in [143], where a brief summary of the features of a non-interacting Bose gas in a harmonic trap is given. A similar argument based on the density of states is presented in [144]. Next, we will see how interactions perturb our picture, before considering the dynamic behaviour of the condensate through the Gross-Pitaevskii equation.

3.3.1 Non-interacting trapped bosons

We can write the many body Hamiltonian of a non-interacting ideal Bose gas as the sum of single particle Hamiltonians with eigenvalues

$$\varepsilon_{n_x n_y n_z} = \left(n_x + \frac{1}{2}\right)\hbar\omega_x + \left(n_y + \frac{1}{2}\right)\hbar\omega_y + \left(n_z + \frac{1}{2}\right)\hbar\omega_z, \tag{3.24}$$

where n_x, n_y, n_z are integers. The ground state of N non-interacting bosons confined to a harmonic potential is obtained by setting these to zero, leading to

$$\psi_0(\mathbf{r}) = \left(\frac{m\omega_{ho}}{\pi\hbar}\right)^{\frac{3}{4}} exp[-\frac{m}{2\hbar}(\omega_x x + \omega_y y + \omega_z z)]. \tag{3.25}$$

We must now define the total number of atoms, N, in the grand-canonical ensemble,

$$N = \sum_{n_x,n_y,n_z} \frac{1}{exp[\beta(\varepsilon_{n_x n_y n_z} - \mu) - 1]}, \tag{3.26}$$

where μ is the chemical potential, $\beta = 1/(k_B T)$, and the total energy is

$$E = \sum_{n_x,n_y,n_z} \varepsilon_{n_x n_y n_z} \frac{1}{exp[\beta(\varepsilon_{n_x n_y n_z} - \mu) - 1]}. \tag{3.27}$$

It is now convenient to separate out the lowest eigenvalue ε_{000} from the sum of the number of atoms, and label it N_0. By subtracting this from Equation 3.26, and replacing our summation with an integral (valid for $k_B T \gg \hbar\omega_{ho}$ and $N \to \infty$), we can write

$$N - N_0 = \int_0^\infty \frac{dn_x dn_y dn_z}{exp[\beta\hbar(\omega_x n_x + \omega_y n_y + \omega_z n_z)] - 1}. \tag{3.28}$$

The integral can be evaluated to

$$N - N_0 = \zeta(3)\left(\frac{k_b T}{\hbar\omega_{ho}}\right)^3 \tag{3.29}$$

where the Riemann zeta function $\zeta(3) \approx 1.202$. The transition temperature, T_c, is obtained by imposing $N_0 \to 0$, leading to

$$k_B T_c = 0.94\hbar\omega_{ho} N^{\frac{1}{3}}. \tag{3.30}$$

The temperature dependence of the condensate fraction can then be readily written down as

$$\frac{N_0}{N} = 1 - \left(\frac{T_0}{T}\right)^3, \tag{3.31}$$

plotted in Figure 3.7. This model gives predictions for transition temperatures which are already in good agreement with experimentally measured values [145]. Corrections such as a finite number of atoms in the trap or interaction between the atoms must be added to reduce the gap between theoretically predicted and experimentally measured values.

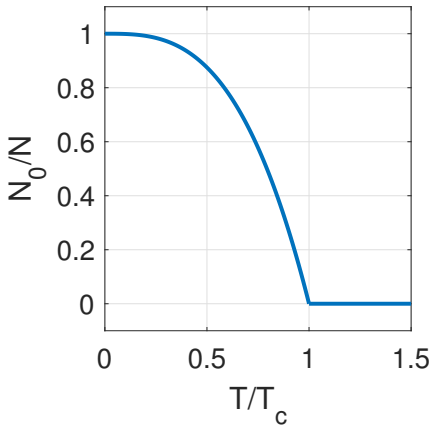

Figure 3.7: Condensed fraction dependence on the transition temperature, plotted from Equation 3.31.

3.3.2 Interacting trapped bosons

Up until the transition temperature the atoms can be well approximated as non-interacting. Once in the BEC, densities high enough that interactions must be considered are achieved. The many-body Hamiltonian of this N boson system confined to an external potential V_{ext} is

$$\begin{aligned}\hat{H} = &\int d\mathbf{r}\hat{\Psi}^{\dagger}(\mathbf{r})\left[-\frac{\hbar^2}{2m}\nabla^2 + V(\mathbf{r})\right]\hat{\Psi}(\mathbf{r}) \\ &+\frac{1}{2}\int d\mathbf{r}d\mathbf{r}'\hat{\Psi}^{\dagger}(\mathbf{r})\hat{\Psi}^{\dagger}(\mathbf{r}')V(\mathbf{r}-\mathbf{r}')\hat{\Psi}(\mathbf{r})\hat{\Psi}(\mathbf{r}'),\end{aligned} \tag{3.32}$$

where $\hat{\Psi}^{\dagger}(\mathbf{r})$ and $\hat{\Psi}(\mathbf{r})$ are the creation and annihilation operators of bosons at position $\mathbf{r}$, and $V(\mathbf{r}-\mathbf{r}')$ is the interatomic potential.

We aim to determine the ground state of this system, which is non trivial to calculate from the Hamiltonian. Mean-field theory allows many simplifications. Firstly, the Bogoliubov approximation allows splitting of the operator in the Heisenberg repre-

sentation $\hat{\Psi}(\mathbf{r},t)$ into $\hat{\Phi}(\mathbf{r},t)+\hat{\Psi}'(\mathbf{r},t)$. Physically, the modulus $|\hat{\Phi}(\mathbf{r},t)|^2$ defines the condensate density distribution $n_0(\mathbf{r},t)$, and is often referred to as the 'wave function of the condensate'. In a cold dilute gas, only binary collisions are relevant, so we can replace the interaction term with an effective interaction term

$$V(\mathbf{r}'-\mathbf{r}) = g\delta(\mathbf{r}'-\mathbf{r}) \tag{3.33}$$

where the coupling constant g is dependent on the s-wave scattering length a by $g = \frac{4\pi\hbar^2 a}{m}$. Placing the above into the Heisenberg equation leads to the Gross-Pitaevskii (GP) equation,

$$i\hbar\frac{\delta}{\delta t}\Phi(\mathbf{r},t) = \left[-\frac{\hbar^2\nabla^2}{2m}+V(\mathbf{r})+g|\Phi(\mathbf{r},t)|^2\right]\Phi(\mathbf{r},t) \tag{3.34}$$

For a system of non-interacting bosons, the condensate has a density distribution of a Gaussian with average width a_{ho}.The interactions are characterised by the s-wave scattering length a. The scattering length sets the interaction energy of atoms in the trap, whose kinetic energy is dictated by the harmonic oscillator length, a_{ho}. A comparison of the two energy scales dictates the importance of interactions to the dynamics of the system. The width of the condensate, for positive (repulsive) scattering length systems, is typically much larger than a_{ho}, confirming interactions are at play.

To obtain the ground state from mean field theory, we can write the condensate wave function, $\Phi(\mathbf{r},t)$, as

$$\Phi(\mathbf{r},t) = \phi(\mathbf{r})exp\left[\frac{-i\mu t}{\hbar}\right] \tag{3.35}$$

leading to the GP equation having the form

$$\mu\phi(\mathbf{r}) = \left[-\frac{\hbar^2\nabla^2}{2m}+V(\mathbf{r})+g|\phi(\mathbf{r})|^2\right]\phi(\mathbf{r}). \tag{3.36}$$

In the limit of $Na/a_{ho} \gg 1$ (large N), we can make the Thomas-Fermi (TF) approximation, neglecting the $\hbar^2\nabla^2/2m$ term in the GP equation. In this case, the density

profile of the atomic cloud can be simply written as

$$n(\mathbf{r}) = |\phi(\mathbf{r})|^2 = \frac{\mu - V(\mathbf{r})}{g}. \tag{3.37}$$

In other words, the density profile will have the form of an inverted parabola (due to the harmonic potential shape), which vanishes at the edges of the condensate, of the form

$$n(\mathbf{r}) = A\left[1 - \left(\frac{x}{R_x}\right)^2 - \left(\frac{y}{R_y}\right)^2 - \left(\frac{z}{R_z}\right)^2\right], \tag{3.38}$$

where R_x, R_y, R_z are the radii in the respective directions, and A is the maximum density. This prediction has been well confirmed in experiments.

Chapter 4

Cold AM - Apparatus

In this chapter the experimental apparatus for a cold atom radio-frequency magnetometer is presented. The vacuum systems, lasers, optics and magnetic field control are all described. Much of this set-up is then upgraded in later chapters to produce an ultra-cold radio-frequency magnetometer.

4.1 Vacuum system

Trapping, cooling and manipulation of cold atoms must occur in ultra high vacuum conditions, achieved by continuous pumping of a vacuum system. The setup, illustrated in Figure 4.1, is split into two chambers. The low velocity intense source (LVIS) chamber is pumped to 1×10^{-8} mbar by a $20\,\mathrm{L\,s^{-1}}$ Agilent StarCell ion pump. The science chamber is kept at 2 orders of magnitude lower, via a vacuum impedance, and is pumped by a larger $55\,\mathrm{L\,s^{-1}}$ StarCell ion pump. A SAES MK5 getter pump provides further pumping of the science chamber. Separate vacuum chambers allow for the MOT in the science chamber to be loaded from an LVIS [146].

4.1.1 Baking

With a constant relatively high background pressure of Rubidium in the LVIS chamber, maintenance of the vacuum conditions is required. Failure of the $20\,\mathrm{L\,s^{-1}}$ Varian ion pump meant the system had to be exposed to air so that a replacement (identical model) could be fitted. A full bake out of the system was performed. The baking procedure was carried out by connecting a Turbo molecular pump to two valves, each connected to either of the chambers, as shown in Figure 4.1. The entire system is

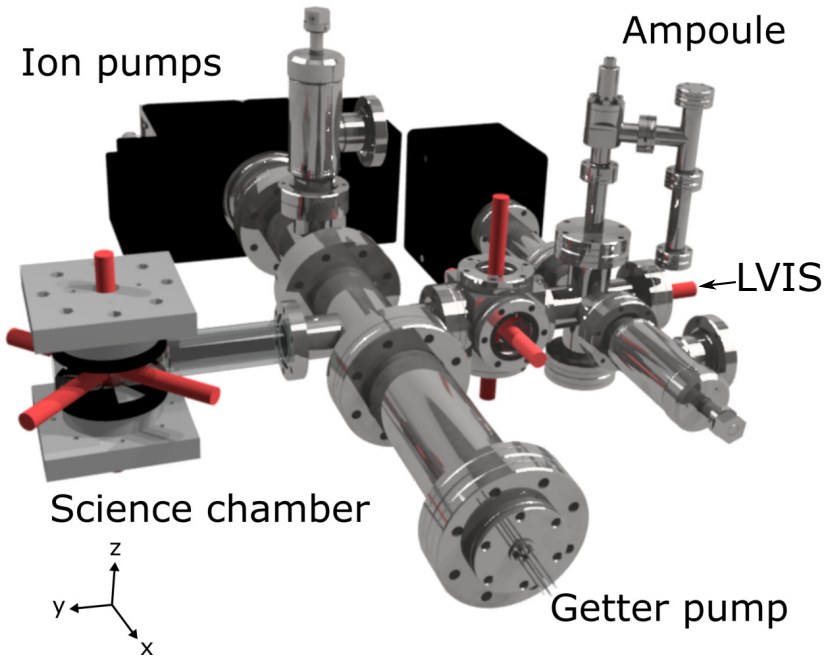

Figure 4.1: 3D (to scale) representation of the cold atoms phase of the experiment. A vacuum chamber is pumped down to pressures as low as 1×10^{-10} mbar, with laser beams shown in red.

wrapped with three resistive heating tapes, each connected to a different Variac which provides a fraction of the voltage drawn from the mains to control the power output of the heating tapes. Three layers of aluminium foil provides even heating of the whole system and isolation from the environment. The baking temperatures are illustrated in Figure 4.2, where the rate of change was kept below $2\,^{\circ}\mathrm{C\,min^{-1}}$ to ensure no glass-metal connections are damaged in the process. Any small imperfection in these connections could lead to an increase in the achievable base pressure. Once the system reached above 100 °C, the getter pump was activated. Electrical feed-through allows for connection to a power source and read out of temperature. The getter was activated by heating to 450 °C for 45 min, as per the manual.

4.1.2 Pressure measurement

After the baking, a base pressure reading of 5×10^{-9} mbar was reached in the science chamber and 1×10^{-9} mbar in the LVIS chamber. These readings are attained from the ion pump currents directly. Overtime, leakage current in the ion pump makes the pressure reading from the current unreliable. Operating the ion pump controller in Step

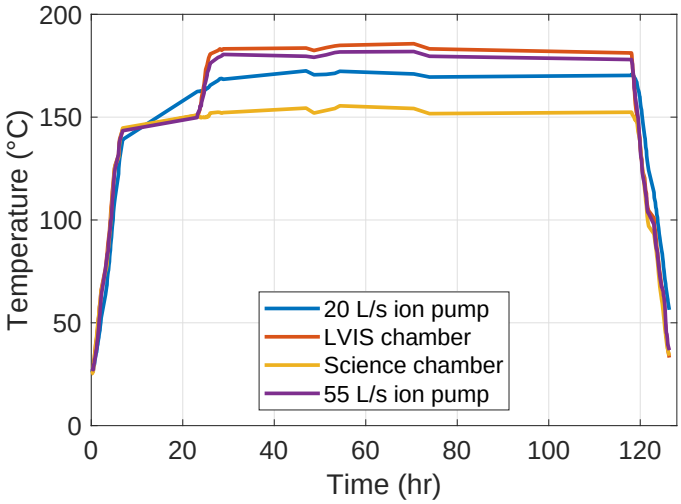

Figure 4.2: Baking of the Vacuum system for 5 days. Measurements of the temperature at different locations of the system ensured the system did not have large temperature gradients, protecting fragile connections.

V mode allows circumventing of this problem, as per the ion pump controller's manual [147]. Step V sees the ion pump controller step down from $-7000\,\mathrm{V}$ to $-5000\,\mathrm{V}$ if a current lower than $3\times10^{-4}\,\mathrm{A}$ is read. It will step down again to $-3000\,\mathrm{V}$ if at $-5000\,\mathrm{V}$ a current lower than $8.5\times10^{-6}\,\mathrm{A}$ is read. The ion pump requires less voltage to pump efficiently at low pressures. Once at $-3000\,\mathrm{V}$ 'Low Pressure' is read on the display, indicating the pressure reading from the ion pump is below $2\times10^{-10}\,\mathrm{mbar}$.

Although the ion pump current is a reasonable indicator of pressure in the system, a more reliable measurement can be made from the MOT lifetime. The MOT loss rate, Γ_{loss}, can be written as

$$\Gamma_{loss} = \Gamma_0 + bP, \tag{4.1}$$

where b is a constant and P is the pressure in mbar. Γ_0 is the loss term due to two body collisions between atoms inside the trap, and is only significant at high cloud densities. The second term dictates the loss rate due to interaction with background atoms not inside the trap. Previous work [148] confirms these two distinct regimes of decay, and shows the first rapidly decaying ($\sim$150 times quicker than the second regime). Therefore, fitting the latter part of the MOT lifetime isolates the losses due to background gas.

Similar work gives an error weighted mean of experimental values of b, cal-

culated for three different systems with a Rubidium MOT, of $6.7 \times 10^7\,\mathrm{mbar}^{-1}\,\mathrm{s}^{-1}$ [149]. A factor of 2 change in this value due to MOT parameters is observed which is negligible in the context of this experiment, so this can be used as a good estimation of our pressure. Other works report similar values for different background gases and MOT alkali atoms [148] [150] [151] [152]. Measurement of the MOT lifetime is shown in Figure 4.3. The lifetime from the fit was 260 s, leading to a pressure of 1.02×10^{-10} mbar.

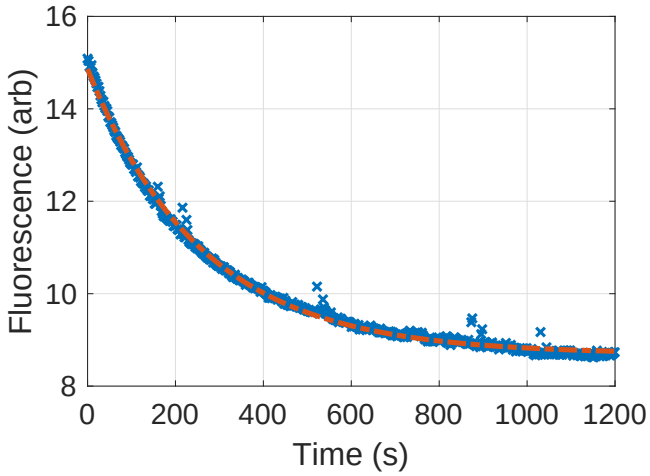

Figure 4.3: MOT fluorescence level as a function of time after loading of the MOT is stopped. This gives a calculated 1/e lifetime of 260 s, corresponding to a pressure of 1.02×10^{-10} mbar

4.1.3 Atomic source

A reservoir of naturally occurring rubidium (ampoule, separated with a valve, see Figure 4.1) is heated, providing the necessary background vapour for fast loading of a MOT in the LVIS chamber. The temperature of the reservoir proved to be very important for the experiment, as shown in Figure 4.4.

With an obvious change in the measured phase-space density (PSD) when the temperature of the ampoule is increased, a dedicated stabilisation and switching system is required. For temperature control the Omron E5CC-RX3A5M-005 PID controller provides much functionality. The PID system here makes use of a relay switch, which is turned on/off for a different percentage of a time period depending on its measured error value (the difference between the set temperature and read tempera-

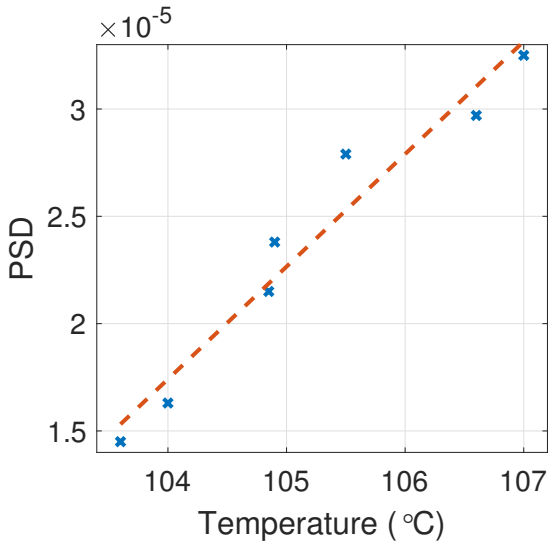

Figure 4.4: PSD measurement after the evaporation in the magnetic trap as a function of the measured temperature of the ampoule. The temperature of the ampoule was measured with a thermocouple placed under foil shielding, and was increased with resistive heating of a heating tape.

ture). The time period can be set by the user as required, and a 2 minute time period was found to be optimal for this application. The PID controller is compatible with K-type thermocouples, which are used here. A supply current is required for the resistive heating tape, which is provided by the Variac already installed to heat the system. Finally, for a weekly schedule, a timer was installed. A Theben digital time switch, NTT07, acts on the event inputs of the PID controller. Depending on the state of the event input pins, different preset temperatures are stabilised. In this way, the heating can be turned on at 5am (105 °C), leaving enough time for the system to stabilise before work begins, and turned off at 8pm (40 °C). Most cold atom vacuum systems require re-baking during their lifetime, due to build up of the alkali metal on the inner surfaces of the chamber. As these become saturated, their pumping capacity is reduced, leading to an increase in background base pressure. Therefore, the heating is turned off over the weekend, and turned on earlier on Sunday to account for this switching off, limiting the degradation of the vacuum conditions when the experiment is not in use.

4.2 Laser control

An overview of the optical components and lasers used is shown in Figure 4.5. Due to the difficulty in representation of a 3 dimensional space in a 2 dimensional image there are some inaccuracies in the sketch. This mainly affects beams going through the page, such as the up down beams of the MOTs and the imaging beam. All optics, apart from the cooling beam spectroscopy and fibre injection, are on the same optical table. A computer controlled sequence acts on components such as shutters or AOMs for sequencing.

4.2.1 Frequency and intensity control

The control of a laser's frequency, intensity, direction, and polarisation is required for any atomic physics experiment. An overview of a generic control system will be presented, to introduce ideas which will be used practically, before an explanation of the specific arrangement of this experiment.

To tune the laser frequency, Doppler-free saturated absorption spectroscopy is used, achieved in the usual way. Once saturated absorption spectroscopy is attained, the signal can be converted to a zero crossing error signal suitable for locking, via the use of DAVLL [153] or frequency modulation lock [154]. Spectroscopy provides a reference point for the frequency, but for improved stability it is useful to lock to the larger signals generated by cross over peaks, midway in frequency space between hyperfine transitions. Consider the case where the laser is locked to the ^{87}Rb $5^2S_{1/2}, F = 2 \rightarrow 5^2P_{3/2}, F' = 2/3$ crossover, which is 133 MHz from the ^{87}Rb $5^2S_{1/2}, F = 2 \rightarrow 5^2P_{3/2}, F' = 3$ cooling transition. An AOM in the double pass configuration is employed [155], before spectroscopy, ensuring no alignment change with small changes in AOM driving frequency (ω_{RF}) whilst allowing for fine tuning of frequency. The -1 order of the AOM is chosen for double pass, resulting in the laser being $2\omega_{RF}$ higher in frequency than the locking point.

Later in the setup, another AOM is installed, this time in a single pass configuration (-1 order), closely followed by a telescope with a mechanical shutter at its focal point. This allows fast on/off switching of the laser beam as well as stabilisation of the intensity. Switching is performed by the shutter, whilst a photodiode and RF

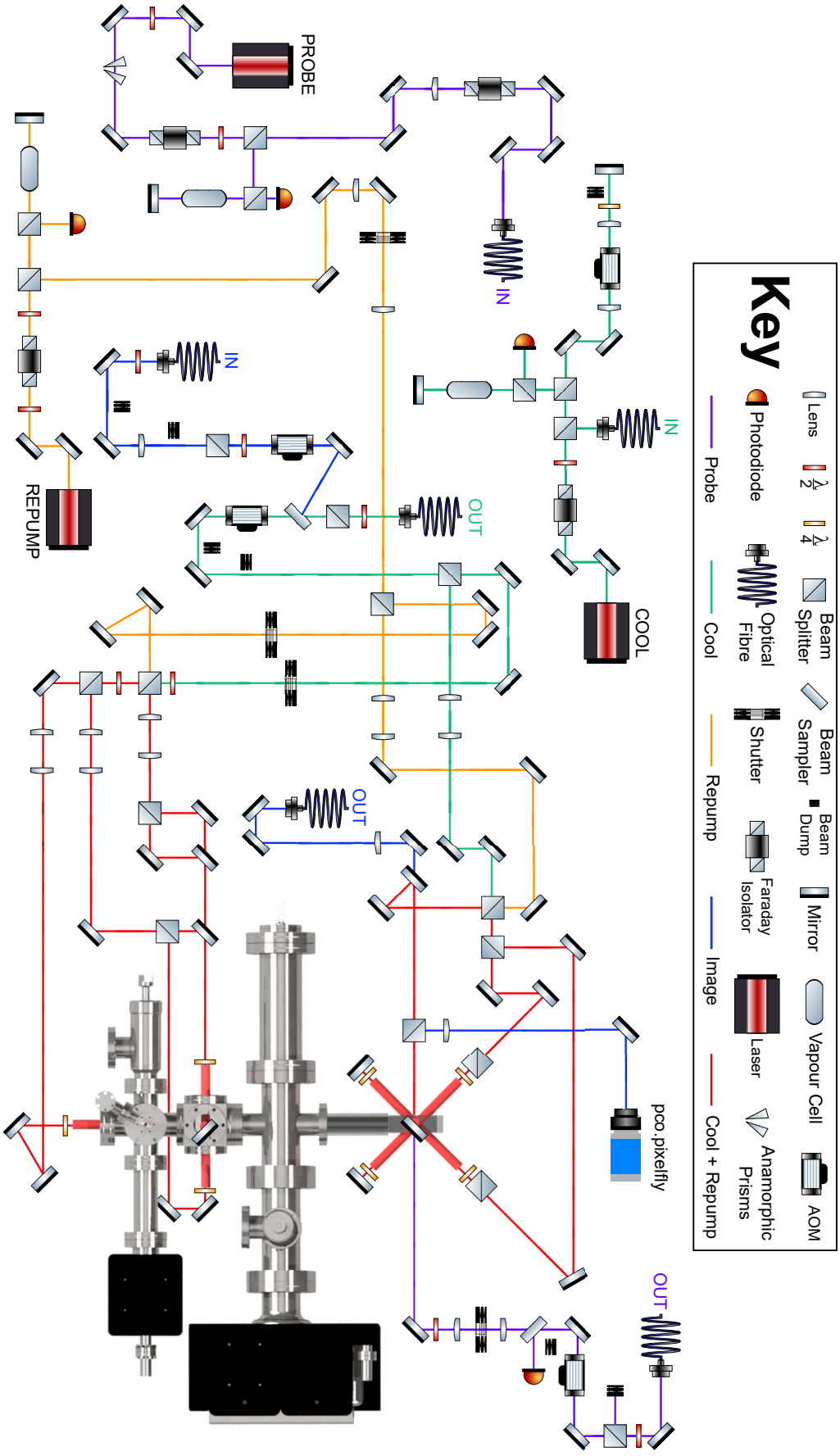

Figure 4.5: The optical setup for cold atom magnetometry. Three separate lasers, locked to atomic references, cool and probe the atoms. Some omissions are made for clarity.

amplitude modulation of the AOM drive frequency allows a PID controller to dictate intensity. Switching cannot be performed solely by the AOM as some leakage light is always present, even when the amplitude modulation is set to a minimum. Later on, when the atoms are magnetically trapped, resonant leakage light is catastrophic, justifying the need for a mechanical shutter.

Setting ω_{RF} to 98.3 MHZ and the single pass AOM to 75.4 MHz sees the overall shift in frequency of +116.6 MHz, detuning the cooling laser by 12.1 MHz ($\sim 2\Gamma/2\pi$, $\Gamma/2\pi = 6.07$ MHz [81]). For ease of use, the setpoints in the LabVIEW program which controls the sequence is in units of $\Gamma/2\pi$. A voltage controlled oscillator (VCO) is used, which was calibrated using a spectrum analyser, show in Figure 4.6. The laser control is also illustrated on an energy level diagram in Figure 4.7.

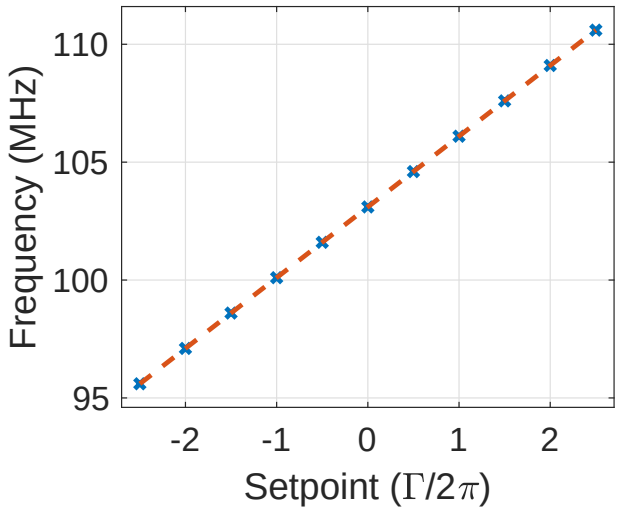

Figure 4.6: A calibration of the cooling VCO, used to determine the setpoint required for different stages in the sequence.

A problem was encountered with the MOT sequencing. When longer sequences are run, where the cooling beams are off for tens of seconds, the starting atom number in the MOT was lower. This can be seen in Figure 4.8. A 10 s wait between successive MOT loading was introduced for testing purposes, during which the cooling beams are off. When compared to 0.1 s wait, the MOT does not load for the first 3.65 s.

This was attributed to temperature change in the AOM, which causes significant alignment change as the AOM warms up. Previously when the cooling beams are off,

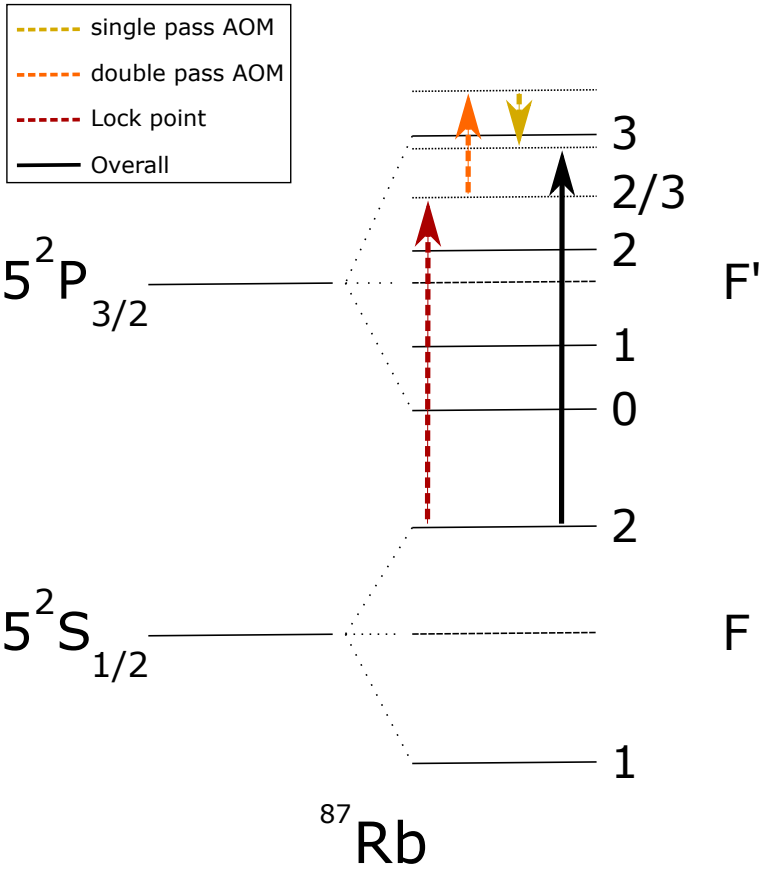

Figure 4.7: The locking point and AOM frequency shifts of the ^{87}Rb cooling beam. The laser is locked to the ^{87}Rb $5^2S_{1/2}, F = 2 \rightarrow 5^2P_{3/2}, F' = 2/3$ crossover. The double pass AOM shifts the frequency by +196.6 MHz, and the single pass shifts the frequency by -75.4 MHz. A total of +116.6 MHz sees the laser red detuned by $\sim 2\Gamma/2\pi$ from the ^{87}Rb $5^2S_{1/2}, F = 2 \rightarrow 5^2P_{3/2}, F' = 3$ transition.

no RF signal is sent to the AOM. Instead, to maintain the temperature of the AOM, a 100 MHz dummy signal is sent. This was used to ensure it is within the AOMs bandwidth (and so causing heating) yet far enough away from the 75.4 MHz used to be completely blocked when the cooling beams are off. A MOGLabs AADPCB AOM Driver is used, providing 2 separate channels with on/off switching and amplitude and frequency modulation. The output of both is sent to a Mini Circuits ZMSC-2-1+ power splitter/combiner, and then directly to the AOM. For the MOT, turning the 75.4 MHz off and 100 MHz on is sufficient to fix the problem, although for other applications (such as pointing instability in dipole trapping, discussed further in Section 6.2.1) amplitude modulation is more appropriate.

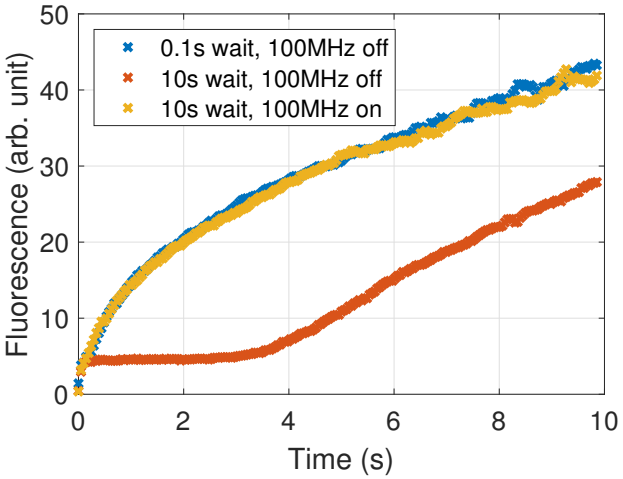

Figure 4.8: A comparison of the AOM driving with and without the dummy signal. With the dummy signal driving, the delay in loading due to heating of the AOM, and therefore misalignment of the cooling beams is completely removed.

4.3 Magnetic field control

Control of magnetic fields is paramount in the experiment. Most traps used in the experiments require specific fields, and magnetometry requires efficient cancelling of stray fields. Magnetic fields are controlled with coils in the Helmholtz or anti-Helmholtz configuration, for uniform or gradient fields respectively.

Passive uniform and gradient compensation coils are installed for the $\hat{x}$ and $\hat{y}$ directions (side length 17 cm and 19 cm respectively) as defined in Figure 4.1. Current is supplied to these coils via synchronous four quadrant power supplies (Linear technology DC2240A LT8714EE), allowing switching of the magnetic field direction during the sequence via a control voltage. Response to a change in control voltage as well as a calibration is shown in Figure 4.9. The coils powered by this supply respond within a milliseconds, which is satisfactory for the experiment. For compensation in the $\hat{z}$ direction, multiple separate coils are wound around a 3D printed PLA mount which attaches to the quadrupole coil mount. Coils in this direction include; anti-Helmholtz and Helmholtz coils, dedicated coils for optical pumping, and an RF evaporation coil. An overview of the coil dimensions and field produced is given in Table 4.3, with a sketch of the setup in Figure 4.10.

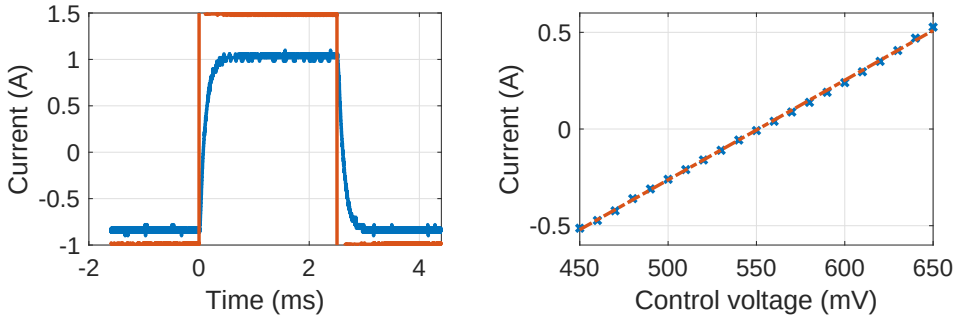

Figure 4.9: Left: The response to a step change in control voltage is measured. The gate voltage is driven at 400 Hz by a square wave, shown in red, with the current response shown in blue. The rise and fall time of the current is < 1 ms. Right: A calibration of the control voltage, used to calculate the applied field at the atoms during different phases of the experiment.

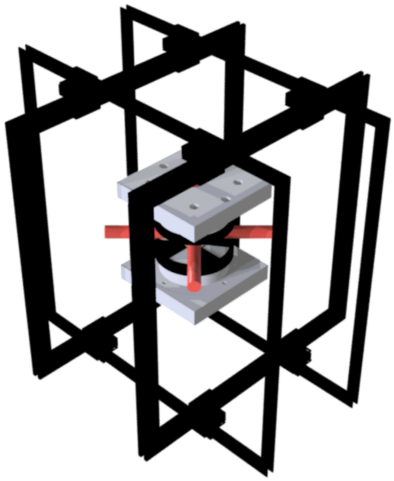

Figure 4.10: To scale, three dimensional representation of all coils around the chamber. 3D printed coil mounts allow for optimal separation and alignment of the coils.

	Direction	Current (mA)	N	Radius (mm)	Field (G)
X Comp	x	145	30	165	0.24
Y Comp	y	40	30	190	0.06
Z Comp	z	490	8	46	0.77
OP	z	30	8	46	0.05

Table 4.1: Coils used to control the magnetic field at the atoms, with their dimensions. Further coils are installed in the $\hat{z}$ direction, such as the RF evaporation and dipole trap offset coils. Gradient compensation are also installed in all axes, with the same dimensions as their 'comp' counterparts, omitted here because they are not used for this section of the experiment.

The centre piece of the magnetic field control is the water-cooled gradient providing coils. These require cooling due to the high currents used during magnetic trapping (up to 100 A, required later on in the experiment for Bose-Einstein condensation), and therefore considerable heat generated. Consisting of 40 turns of ($4\,\mathrm{mm} \cdot 2\,\mathrm{mm}$ cross section) copper wire, these coils provide up to $225\,\mathrm{G/cm}$, and are illustrated in Figure 4.11. The coils sit in an O-ring sealed PVC mount, and water flows in the sealed section. Two elbow hose couplings provide entrance and exit points for the water, and are connected to the main supply via flexible tubing sealed with hose clips. Valves are installed between the water supply and coils, allowing for maintenance and switching of the coils, as well as switching off of the water supply to reduce the potential damage of a water leak when the coils are not in use. A bypass ensures water flows throughout the rest of the system, limiting failures due to freezing in the winter.

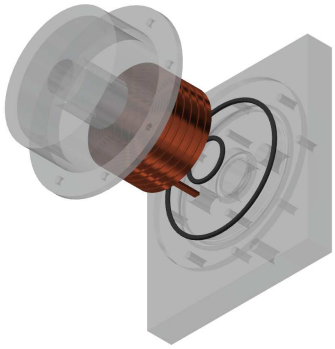

Figure 4.11: Coil mount designed to provide water cooling, necessary for magnetic trapping required to reach ultracold temperatures, to scale and expanded for clarity. The copper wire is wound with 1 mm spacings to allow water to flow between turns, increasing the cooling efficiency. Rubber O-rings are compressed by connecting the cup and base of the mount to form a seal.

Control of the current in the coil comes from a dedicated water-cooled MOSFET system. 6 IXFN 150N15 MOSFETs are used, to distribute the load between them, which are mounted onto a water-cooled copper plate. The output current is passed through the centre of a Hall sensor, Honeywell CSNP661, before going to the coils. In this way, the current can be inferred without a sensor being directly placed inside the circuit. The Hall voltage is therefore used as the measure for the stabilisation system. An overview of the current control and stabilisation system is shown in Figure 4.12. The LabVIEW sequence sends a voltage to the setpoint of the PID, which acts on the

MOSFET to increase or decrease the current. The coils were characterised, allowing

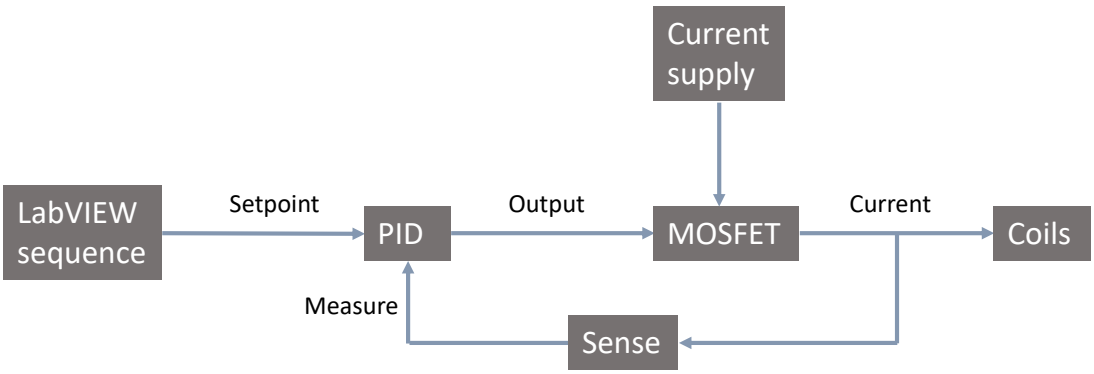

Figure 4.12: Current stabilisation logic for gradient coils. LabVIEW sequence is a dedicated program used for timing of the experiment. PID is a SIM960 analogue PID controller. Sense is a Honeywell CSNP661 sensor. The current supply can provide a maximum of 100 A.

for a direct conversion of Hall voltage used for stabilisation to gradient of the magnetic field felt by the atoms. This is shown in Figure 4.13.

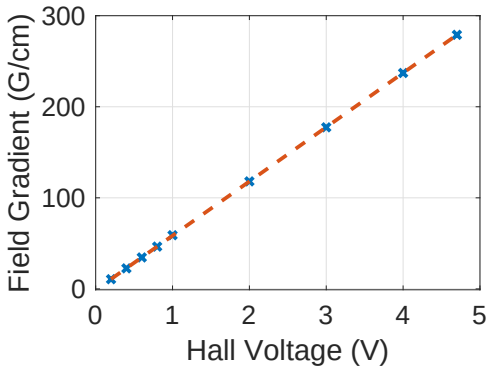

Figure 4.13: The Hall voltage measured from the Honeywell CSNP661 sensor is calibrated to a magnetic field gradient. The voltage is used to monitor the current during the sequence of the experiment, which is then PID stabilised.

Once implemented, the ramp up time of the gradient, and eventually the magnetic trap, was considered. The error signal can be monitored from the PID, and so used to track the increase in field gradient (as the error goes to zero). The ramp up is illustrated in Figure 4.14, and confirms the millisecond response of the magnetic field gradient.

The water supply for the cooling of the coils is an external system which provides water cooling for all the labs in the building. Due to its temperamental nature, a failure of this system is simulated in Figure 4.15. Overheating of the coils can be catastrophic

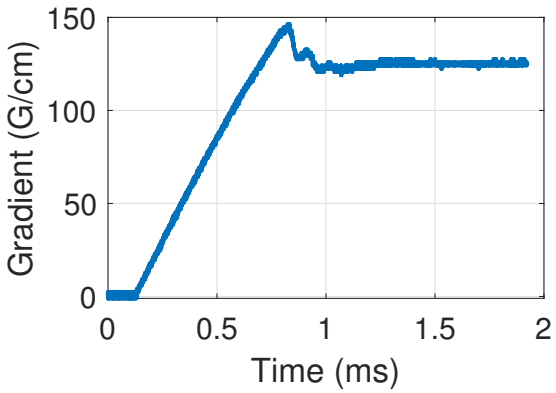

Figure 4.14: The ramping up of the gradient coils to 125 G/cm. The gradient is stabilised to the desired value in 1 ms, ensuring minimal atom loss.

to the experiment, with permanent deformation of the PVC mount leading to leakage. The temperature measured is that of the copper wire which provides the magnetic field, leaving the mount through two exit holes. This measurement is indeed sensitive to a sudden stop in water supply.

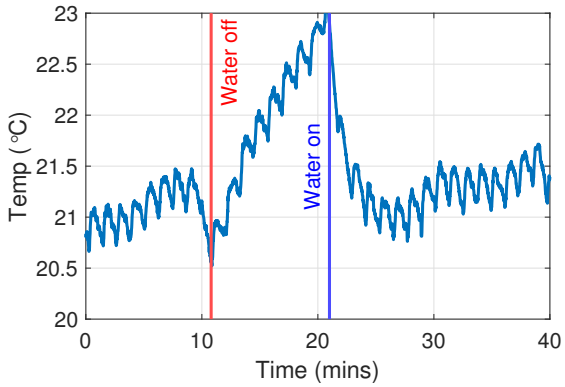

Figure 4.15: Failure of the water-cooling system simulated by turning off the supply of the water. Problems with previous implementations have been due to a lack of flow of water in the system. This data confirmed we can be sensitive to the failure of the water system by a simple measurement of the copper wire temperature.

To limit future failures, a monitoring system with a kill switch was implemented. This includes PT100 RTDs, designed for surface temperature measurement, and DP20-A1 modules. These measure temperature and have a relay output alarm which can be set. For the power supply to go into protection mode, and stop current output, pin 3 and 4 must be shorted. As such, the suggested kill switch logic can be seen in Figure 4.16. As many alarms as required can be implemented. For

now, measurement of both the bottom coil wire and top coil wire is used. Maximum temperature measurements under normal operating conditions were recorded over a couple of days to decide a set point of 32 °C, used for both alarms.

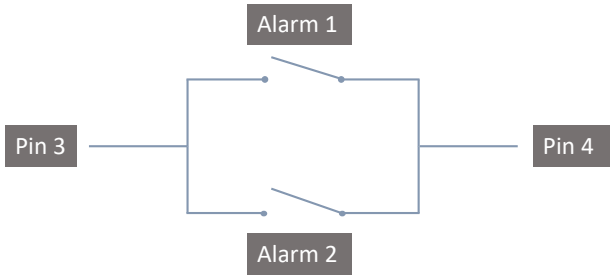

Figure 4.16: The logic implemented for the kill switch of the current in the coils. Relay outputs can be connected in parallel, so if any switch is triggered, the pins of the protection mode of the current supply are connected.

4.4 Magnetometry

The foundation of this experiment is the ^{87}Rb atom trap. Here, atoms are sub-Doppler cooled for magnetometry. Cooling light is provided by a MOGLabs MSA003 system, detuned from the ^{87}Rb $5^2S_{1/2}, F = 2 \rightarrow 5^2P_{3/2}, F' = 3$ transition by $2\Gamma/2\pi$, with an average intensity of $7.5\,\mathrm{mW\,cm^{-2}}$. Repumping light is provided by a MOGLabs CEL002 laser, locked to the ^{87}Rb $5^2S_{1/2}, F = 1 \rightarrow 5^2P_{3/2}, F' = 2$, with an average intensity of $1.4\,\mathrm{mW\,cm^{-2}}$.

Imaging of the atoms can be performed with either fluorescence imaging, which allows for real time observation of the atoms, or absorption imaging, which allows for measurements of atom number, temperature, position, and cloud size. Absorption imaging is destructive, and so must be done at different stages when required. Both are detailed further in Appendix A.

Once a reliable source of dense, sub-Doppler cooled atoms was attained, the magnetometry could begin, as sketched in Figure 4.17. Helmholtz coils, wound around the circular PLA mount described in Section 4.3, set $\mathrm{B_{Bias}}$, inducing Zeeman splitting of the atoms energy levels in the $\hat{z}$ direction.

Circularly polarised light propagating in the $-\hat{z}$ direction, resonant with the ^{87}Rb $5^2S_{1/2}, F = 2 \rightarrow 5^2P_{3/2}, F' = 3$ transition, optically pumps the atoms to the

$|F = 2, m_F = +2\rangle$ state in preparation for precession. In this experiment, the beam used for absorption imaging of the atoms was also used for optical pumping. The intensity of the pump pulse is $60\,\mu W\,cm^{-2}$, with a dedicated AOM for fast switching.

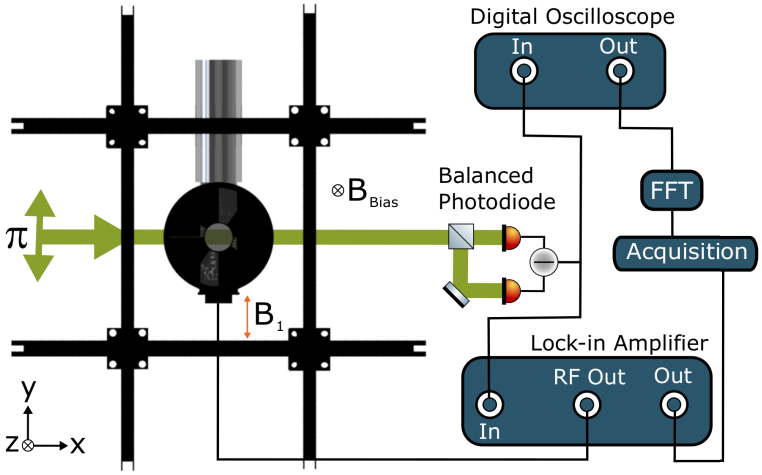

Figure 4.17: A schematic of the magnetometer phase of the experiment. Once cooled, B_{Bias} and circularly polarised light optically pump the atoms. Precession is excited by B_{RF}, and read out via a linearly polarised probe beam and polarimeter. Acquisition by either a digital oscilloscope or lock-in amplifier (AMETEK 7230 DSP), allows for full characterisation of the magnetometer.

Once the atoms are optically pumped, an oscillating magnetic field (B_1) in the $\pm\hat{y}$ direction, provided by an RF coil (3D printed PLA square, 35mm side length, 20 turns of 0.5mm diameter copper wire, 39mm away from the atoms) excites precession of the atoms.

This is read out via a linearly polarised probe beam, provided by a RadiantDyes NarrowDiode laser, injected into a Thorlabs P3-780PM-FC-2 optical fibre. At the output, a polarising beam splitter converts any polarisation instability into oscillations in intensity. A feedback loop, consisting of AOM, PID and photodiode actively stabilises the probe beam intensity at $257\,\mu W\,cm^{-2}$. A telescope is used to match the probe size to the estimated cloud size (for maximal signal to noise ratio (SNR) [56]). Saturated absorption spectroscopy is used to lock the probe to the ^{85}Rb $5^2S_{1/2}, F = 3 \rightarrow 5^2P_{3/2}, F' = 3/4$ crossover, which is +1.1 GHz away from the ^{87}Rb $5^2S_{1/2}, F = 2 \rightarrow 5^2P_{3/2}, F' = 3$ transition [156]. The probe beam optical path can be seen in Figure 4.5. A calibration of the probe power against the readout voltage can be seen in Figure 4.18.

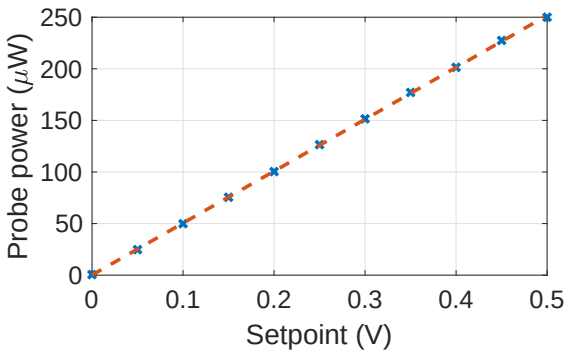

Figure 4.18: Probe beam power calibration, required for optimisation of the probe power against sensitivity of the magnetometer.

The polarisation of the probe beam, modulated at the precession frequency due to Faraday rotation, is measured via a polarimeter consisting of polarising beam splitter and balanced photodiode (omitted from Figure 4.5 for clarity). At $t = 0$, the polarisation of the probe beam is set to balance the two arms of the polarimeter using a $\frac{\lambda}{2}$ wave plate. The output of the polarimeter is sent either to a lock-in amplifier (LIA) (AMETEK 7230 DSP), referenced to its internal oscillator which is driving B_1, or to a digital oscilloscope (Tektronix DPO2014) which acquires the signal for a Fast Fourier Transform (FFT) performed by a LabVIEW program.

Chapter 5

Cold AM - Results

Once built, the cold atom radio-frequency magnetometer is optimised and characterised, which will be described in this chapter. The measurement sequence is detailed, and results are highlighted which led to a publication [1].

5.1 Sequence

Timing is key for the experiment, with phases as short as 0.8 ms requiring precise control of many instruments. Figure 5.1 illustrates the different phases of the experiment. Firstly, atoms are loaded into the science chamber MOT for 7 s, with the magnetic field gradient set to $32\,\mathrm{G/cm}$. To increase the density of the atoms, a compressed MOT (C-MOT [157]) is used for 12 ms, where the magnetic field gradient is ramped up to $59\,\mathrm{G/cm}$ whilst the detuning of the cooling laser is increased to $2.5\Gamma/2\pi$.

Polarisation gradient cooling follows, for 7 ms, by turning off the quadrupole coils and detuning the cooling beam further to $4\Gamma/2\pi$ whilst reducing its intensity to $3\,\mathrm{mW\,cm^{-2}}$. The temperature of the atoms is $(19 \pm 4)\,\mu\mathrm{K}$ at this stage, with a density of $1 \times 10^{10}\,\mathrm{cm^{-3}}$. A full discussion of the procedure for temperature and density measurements is given in Appendix A.2.

Next, B_{Bias} is switched on for 0.8 ms, as well as circularly polarised light for optical pumping. Once pumped, the atoms go through a 10 ms precession and measurement phase. Here, B_1 is turned on, as well as a linearly polarised probe beam for read out of the Larmor precession, whilst the pump beam is turned off.

Finally, the cloud is imaged via absorption imaging for diagnostics, dispersing

the atoms. This sequence is repeated immediately. For LIA sweeps, used to deduce the half-width at half maximum (HWHM), the frequency of B_1 is changed per run, building the typical in-phase (X) response and accompanying dispersive out-of-phase response (Y) (see Figure 5.7 (a)).

For SNR measurements (at the resonant frequency, calculated from a Lorentzian fit of the LIA in-phase response), the signal is sent to a digital oscilloscope. This allows for triggered acquisition of the polarimeter signal. A LabVIEW program computes the Fast Fourier Transform (FFT) of the signal. In this way, optimisation of the magnetometer with the LIA can be achieved whilst still attaining an accurate measurement of sensitivity from the FFT.

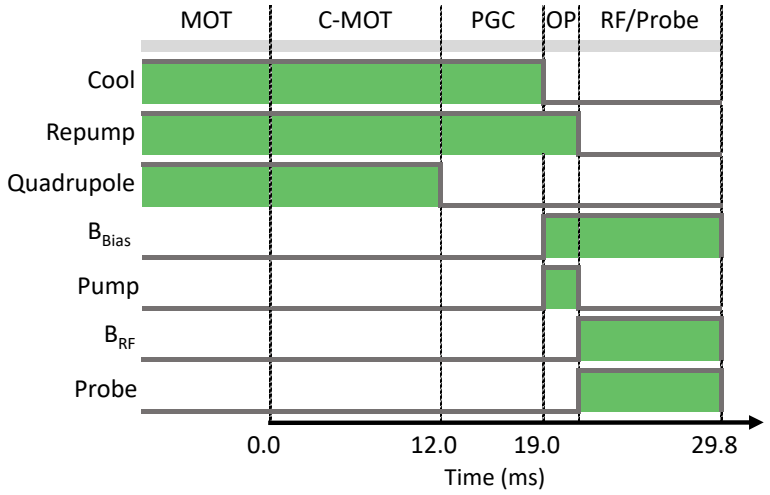

Figure 5.1: The experimental sequence. Atoms are loaded in a MOT, typically for 7 s. A compressed MOT (C-MOT) increases the density of atoms by ramping up the magnetic field gradient and detuning the cooling laser to $2.5\Gamma/2\pi$ for 12 ms. 7 ms of polarisation gradient cooling (PGC) reduces the atomic cloud temperature to $(19 \pm 4)\,\mu$K. Optical pumping (OP) aligns the atomic spin in 0.8 ms, preparing the cloud for coherent precession driven and measured for 10 ms.

5.2 Optimisation

To successfully trap atoms, a full sweep of parameters must be completed and optimised for. These include; laser alignment, frequency, intensity, polarisation, background fields and timings.

Any optimisation of the first MOT is done with the aim of increasing the loading rate of the second MOT. When correctly optimised almost no atoms are seen in the

first MOT, as trapped atoms are immediately transferred to the science chamber. Optimisation of the second MOT, and then C-MOT consists of increasing the atom number and density respectively. All the previously mentioned parameters were swept. PGC give a unique insight into power balance of the MOT beams and compensation coil current (with the quadrupole off). Long PGC time, and absorption imaging, allow investigation into the non-uniformity of cloud expansion, which is then corrected for. Optical pumping detuning from the ^{87}Rb cooling transition and intensity was varied to maximise the magnetometer's signal. With so many parameters to sweep, a small selection of the data taken can be seen in Appendix B. Next, the transverse compensation coil current was investigated, shown in Figure 5.2. This confirmed the scalar nature of the magnetometer whose resonant frequency can be described by

$$\omega_r = \gamma B_T, \tag{5.1}$$

where we can write the total magnetic field magnitude, B_T, as:

$$B_T = \sqrt{B_x^2 + B_y^2 + B_z^2} \tag{5.2}$$

and as the transverse field is linear with respect to the current in the coil, the relationship between coil current and resonant frequency can be described by some generic function:

$$y = \sqrt{(x+a)^2 + b} \tag{5.3}$$

which was used for fitting of Figure 5.2. Clearly, minimisation of B_T, and therefore optimal compensation in the directions perpendicular to optical pumping, occurs when the resonant frequency is smallest. From the fit, the optimal current was found at 102.7 mA for B_y and 40.6 mA for B_x, where it was set.

Next, the optimal magnitude of the oscillating field B_1 was investigated. The sensitivity of the magnetometer is dependent on the dispersive gradient, which is in turn set by the linewidth of the resonance. The Bloch equations describe a broadening of the resonance as RF power is increased, where the full-width-half-maximum

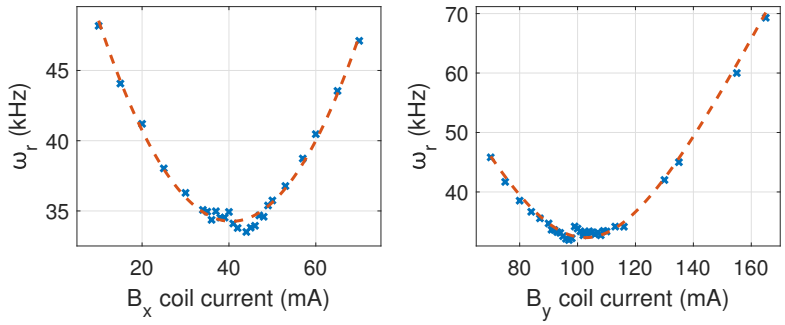

Figure 5.2: Optimisation run of the current in the transverse compensation coils. The resonant frequency, ω_r, as a function of the current in the compensation coils in the transverse directions is investigated. A minimum in ω_r is found at 102.7 mA for B_y and 40.6 mA for B_x from the fits.

(FWHM) of the Lorentzian X response can be written as

$$\Gamma = \frac{2}{T_2}\sqrt{1+\gamma^2 B_1^2 T_1 T_2}. \tag{5.4}$$

The value of B_1 which maximises the sensitivity is therefore $\frac{1}{\gamma\sqrt{T_1 T_2}}$ [158]. As B_1 is increased past the optimal value, eventually a dip in the R response of the lock-in amplifier at the resonant frequency is predicted (further discussion on the Bloch equation's performance can be found in Section 2.3). A simulation of this phenomenon is shown in Figure 5.3. Practically, the magnitude of B_1 is swept to decide on its optimal

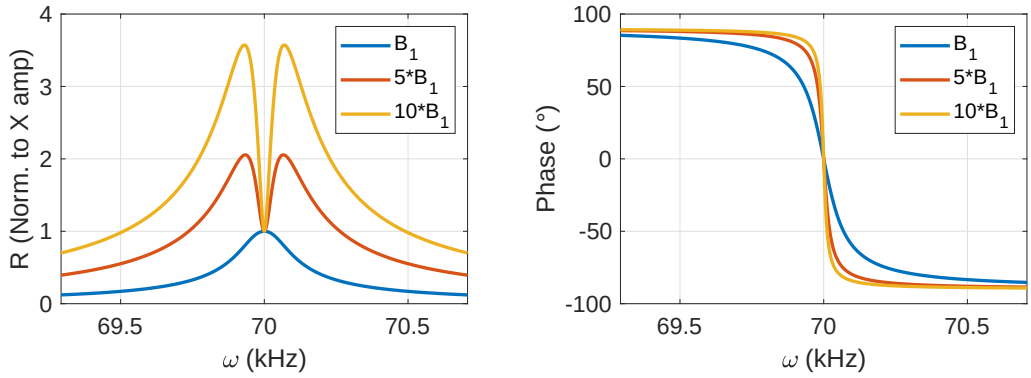

Figure 5.3: Simulation of RF power broadening using the Bloch equations. The predicted dip at resonance in R (left) is seen in experimental data, as well as the broadening of the linewidth. The phase response is also shown for completeness (right).

value, shown in Figure 5.4. The V_{RMS} described in this figure corresponds to the root mean squared output of the lock-in amplifier (LIA). Error bars shown in the figure are

calculated from the fit of R, with the insets illustrating the data and corresponding fits used for each point. Both the HWHM and uncertainty on the HWHM increase with V_{RMS}. As expected, a Lorentzian fit to R is no longer valid at very high calibration fields.

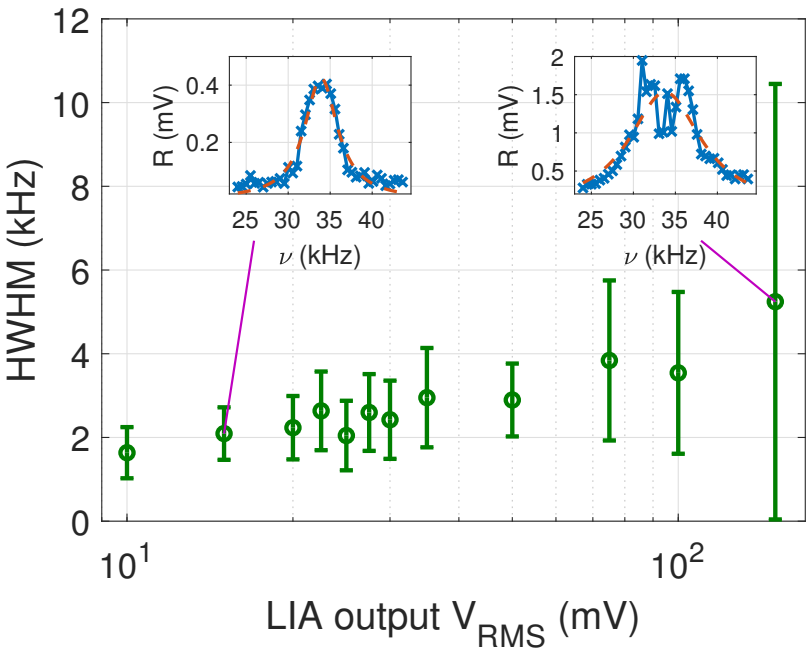

Figure 5.4: Optimisation run of the lock-in amplifiers V_{RMS} output. Evidence of power broadening is shown in the insets, accounting for the increase in HWHM as well as the increase in its uncertainty yielded from the Lorentzian fit.

Finally, probe beam intensity, detuning, alignment and polarisation was optimised for. Intensity was changed with amplitude modulation of the RF signal sent to the dedicated probe AOM. Detuning was changed by locking at different points in the ^{85}Rb D_2 manifold. It is noteworthy that all other locking points arising from spectroscopy of natural rubidium (~ 6.8 GHz range) were investigated. The best signal was attained at the ^{85}Rb $5^2S_{1/2}, F = 3 \rightarrow 5^2P_{3/2}, F' = 3/4$ crossover. Coarse alignment consisted of firstly locking the probe to a ^{87}Rb transition, and then changing the alignment until interaction with the MOT is seen in florescence imaging. Fine alignment was optimised against magnetometer signal. Polarisation was set to match the intensity at the two channels of the balanced photodiode, and then optimised against magnetometer signal.

5.3 Sensor characterisation

Once optimised against its various parameters, the magnetometer's performance was characterised. First, investigations into the polarimeter signal were carried out. Figure 5.5 (a) shows a typically acquired polarimeter signal during the 10 ms measurement phase, with no manipulation. Figure 5.5 (b) shows a fit at the Larmor precession frequency, which is 55 kHz in this example. Here, the signal centred around zero by finding the mean of the data and subtracting this as a constant offset.

Next, the data is processed for extraction of a decay constant, shown in Figure 5.6 (a). The signal was firstly down sampled, to remove high frequency noise, by a simple moving average. For each 10 points, a mean of the y is calculated, which is then plotted at the mean of the x points (shown in the inset). Also, only data after the transient is used, as oscillations seen in the first 4ms is only due to the rise time of the photodiode and the limitations of the PID and not due to the atoms. Next, Figure 5.6 (b) calculates the V_{RMS} at 15 different points between 4 ms and 10 ms. This is then plotted and fitted with an exponential. A decay constant is obtained from the fit, $\tau = 8.4\,\text{ms}$. This can be thought of as the coherence time of the system, limited by magnetic noise, which is not compensated for as the magnetometer is unshielded. With the atoms not trapped during precession, it was confirmed that they are not leaving the probe beam region during measurement. 20 µK atoms have an initial average velocity associated with this temperature of $0.014\,\text{m}\,\text{s}^{-1}$. This velocity, combined with the acceleration due to gravity, sees atoms move 0.63 mm in 10 ms, which is insignificant in comparison to the probe beam size (4 mm).

The response of the magnetometer at $B_{Bias} = 66.4\,\text{mG}$, corresponding to a resonant frequency, ω_r, of 46.5 kHz, is shown in Figure 5.7. Figure 5.7 (a) shows the output of the LIA, used to deduce the HWHM of the resonance, and Figure 5.7 (b) shows the FFT of the polarimeter signal, used to attain the SNR. The LIA is set to reference against its internal oscillator, which in turn drives the current in the RF coil. A resistor is placed in the circuit, allowing for deduction of the current flowing, and calculation of the RF field felt by the atoms. This is used to calibrate the graph shown in Figure 5.7 (b), and calculate the AC sensitivity of the magnetometer. The field

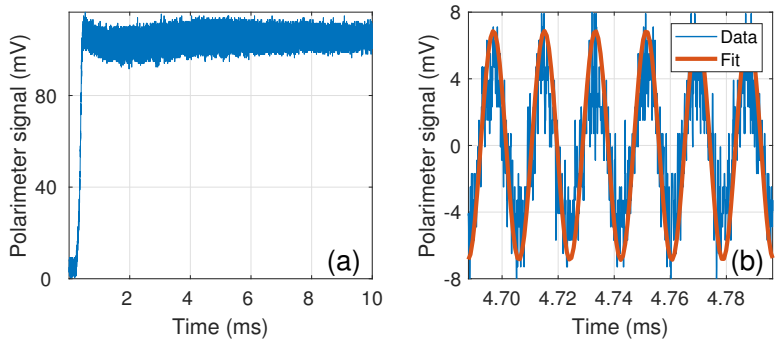

Figure 5.5: The polarimeter signal. (a) The raw output of the polarimeter. (b) A fit of part of the polarimeter signal with the offset removed at a Larmor precession frequency of 55 kHz.

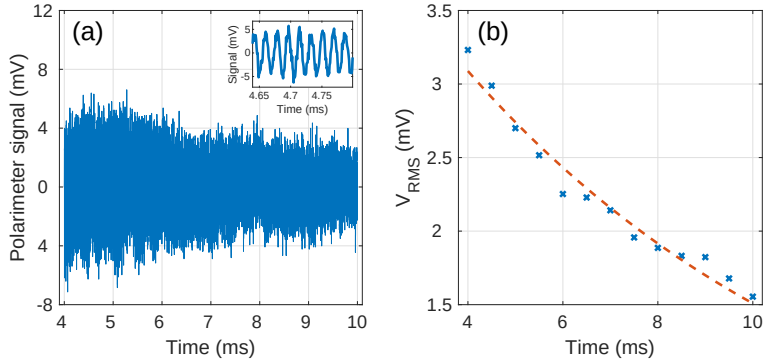

Figure 5.6: The polarimeter signal after processing. (a) 6ms of the polarimeter output. The inset shows the downsampling, using a simple averaging technique. (b) The RMS of the signal as a function of time, with an exponential fit giving an 8.4 ms decay constant

generated by the square calibration coil can be calculated using its parameters (see Section 4.4) [159]:

$$B(\hat{y}) = \frac{2\mu_0 NIa^2}{\pi} \cdot \frac{1}{(a^2+y^2)(2a^2+y^2)^{\frac{1}{2}}} \tag{5.5}$$

where N is the number of turns, I is the current, a is half the side length of the coil, y is axial distance away from the coil, and μ_0 is the vacuum permeability. The best sensitivity was found with B_1 = 11 nT, giving SNR = 33, and HWHM = 230 Hz. The magnetometer's AC sensitivity can be characterised by using this applied calibration field and the SNR:

$$\delta B_{AC} = \frac{B_1}{SNR} \tag{5.6}$$

where the noise level is taken at the resonance with the calibration field, B_1, off [57]. The magnetometer's sensitivity was found to be $330\,\mathrm{pT}/\sqrt{\mathrm{Hz}}$. This is in good agreement with another figure of sensitivity [64, 160], the DC sensitivity:

$$\delta B_{DC} = \frac{\hbar}{g\mu_b} \cdot \frac{\Gamma}{\mathrm{SNR}} \tag{5.7}$$

where Γ is the FWHM of the signal, μ_b is the bohr magneton, $\hbar$ is the reduced Planck constant, and g is the Lande factor. Using a FWHM of 460 Hz, the calculated sensitivity is $310\,\mathrm{pT}/\sqrt{\mathrm{Hz}}$. The tunability of the magnetometer is illustrated in Figure 5.8.

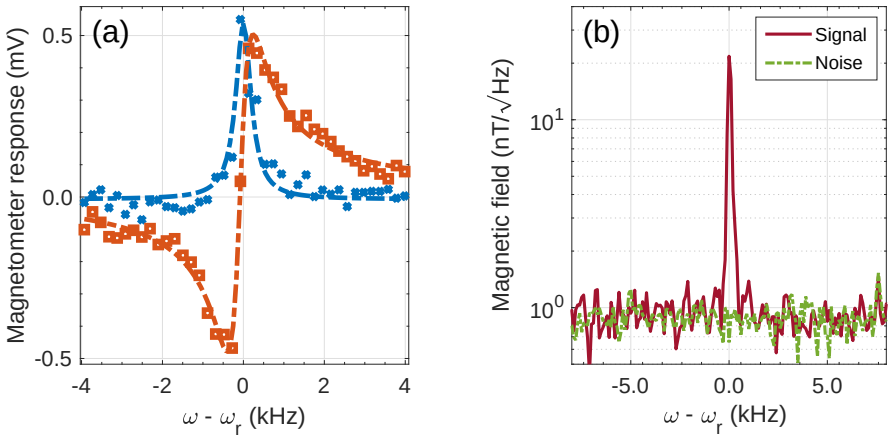

Figure 5.7: The response of the magnetometer, plotted against the detuning from resonance, ω_r. (a) The lock-in amplifier response of the magnetometer. Blue crosses show the in-phase component of the signal (X), with the red squares showing the out-of-phase component of the signal (Y). (b) The FFT of the polarimeter signal, calibrated with an 11 nT B_1

A negligible difference in magnetometer performance is seen at resonant frequencies ranging from 15.9 kHz to 99.6 kHz (22.7mG to 142.3mG). The available LIA has an operating frequency range between 1 mHz to 120 kHz. Lower frequencies could not be explored due to the short measurement duration. The system's response to atom number was also investigated, shown in Figure 5.9. The atom number in the PGC phase (just before the start of magnetometry) was varied by changing the MOT loading time, and the sensitivity recorded. A fit of the data showed that the sensitivity of the magnetometer, δB, scales with $N^{-1.17}$. This implies the magnetometer is currently not spin projection noise limited, expected to scale with $N^{-\frac{1}{2}}$ [41].

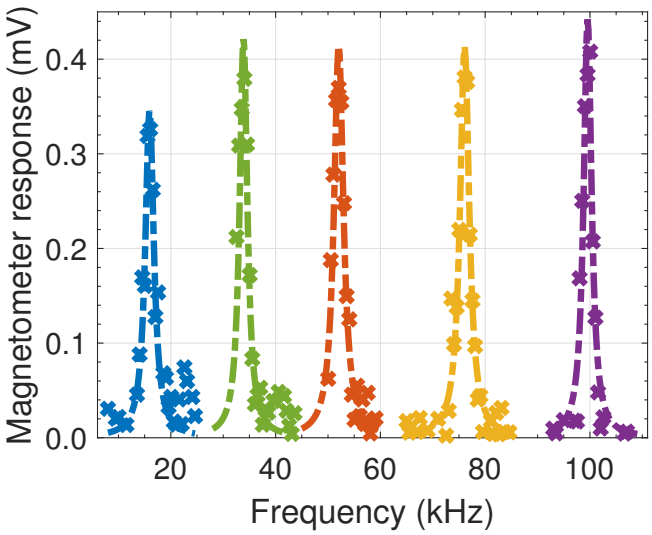

Figure 5.8: Multiple magnetometer responses at different values of B_{Bias}. These correspond to ω_r = 15.9, 33.9, 52.0, 76.1, 99.6 kHz. The HWHM range from 990-1100 Hz, maintaining consistent sensitivity.

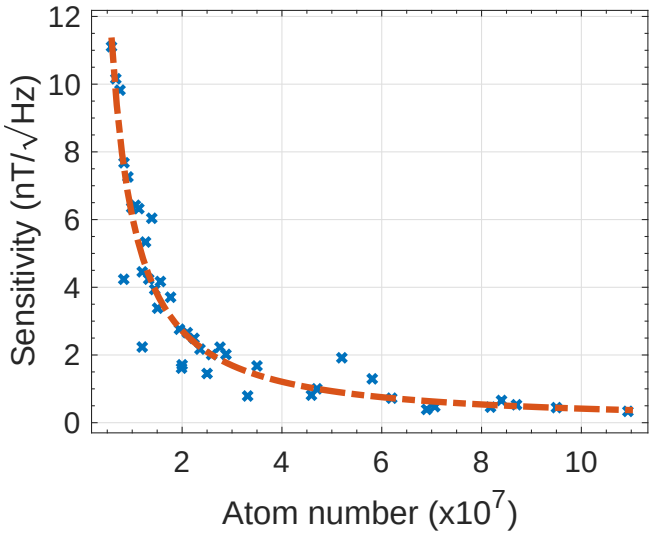

Figure 5.9: Sensitivity of the magnetometer against atom number in PGC. The atom number was varied by changing the loading time of the MOT, and the sensitivity of the magnetometer investigated. The sensitivity scales with $N^{-1.17}$, and so is not spin projection noise limited.

Chapter 6

Ultracold AM - Apparatus

With a cold atom radio-frequency magnetometer realised, the experiment progressed to an ultracold system. Here, a BEC is produced via evaporative cooling, with the experimental apparatus required described in detail in this chapter. A magnetic quadrupole trap is realised, fit for radio-frequency evaporation of the atoms, before a hybrid dipole trap is produced where the atoms are evaporated until condensation.

6.1 Magnetic Trapping

The theoretical underpinning of magnetic trapping is discussed in Section 3.2.1, with the coils which provide the necessary gradient described in Section 4.3. When loading a magnetic trap, the atoms are first optically pumped into $|F = 2, m_F = +2\rangle$ after PGC, before the magnetic field gradient is switched on. Practically, confirmation of efficient optical pumping is given by observing loading into the magnetic trap. In optimised conditions, where the magnetic trap centre overlaps the centre of the atomic cloud after optical pumping, the ratio of the number of atoms measured before optical pumping and immediately after loading of the magnetic trap is close to unity. To account for atoms not repumped during the MOT stage, 300 µs of just repumper before optical pumping is also required. This is discussed further in Appendix A.2.3.

The trap is very sensitive to any resonant light hitting the atoms. As such, all potential sources of scattered light are shielded and shutters are employed on the cooling and rempumping beams. The optical table is isolated from the environment by a black box, with further partitions within for different sections. The centre of the cloud

after optical pumping must coincide with the centre of the magnetic trap for optimal transfer of atoms. This is ensured by optimisation of the science MOT and subsequent phases of the experiment to the atom number measured in the magnetic trap.

The magnetic field gradient is switched on to an initial value of 107 G/cm, before being ramped up to 176 G/cm in 2.5 s. This loading sequence was optimised against atom number (N) and density in the hybrid dipole trap, shown in Figures 6.1 & 6.2. A trade-off between number of atoms and density must be considered. With high PSD the ultimate goal, and only an insignificant increase in atom number at longer durations and higher magnetic fields, the sequence is optimised for density.

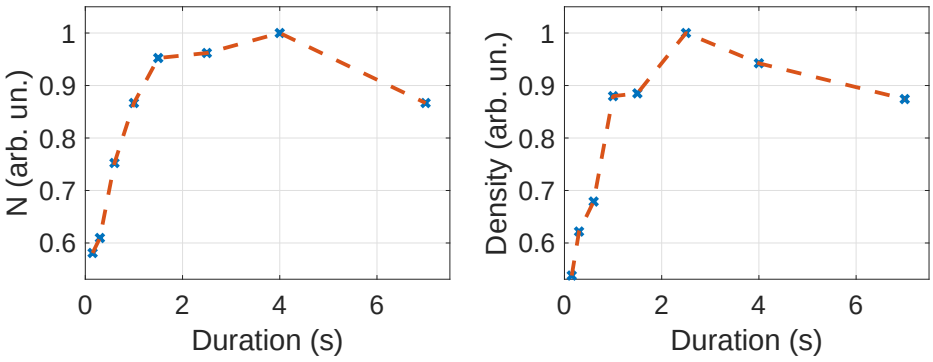

Figure 6.1: Optimisation of the loading time of the atoms after optical pumping into the magnetic trap. Data (blue crosses) plotted with a guide to the eye (red dashed line). The optimal value of 2.5 s is chosen as it maximises the density measured after loading of the hybrid dipole trap, whilst maintaining atom number (N).

Next, the lifetime in the magnetic trap was measured, shown in Figure 6.3. The number of atoms in the trap is measured for different hold times, and the data is fitted with a decaying exponential. As discussed earlier, the loss rate of atoms from the trap dictates the optimal evaporation sequence. A 32 s lifetime is extracted from the fit, setting a limit on the total evaporation time.

6.1.1 Evaporation

Once loaded into the trap with a satisfactory lifetime, evaporation of the atoms can begin. Radio-frequency magnetic fields are provided by a 2 turn coil wound on the same PLA mount which holds the $\hat{z}$ compensation coils. This coil is supplied by a combination of a Rhode & Schwartz SMT02 signal generator and a Mini-Circuits

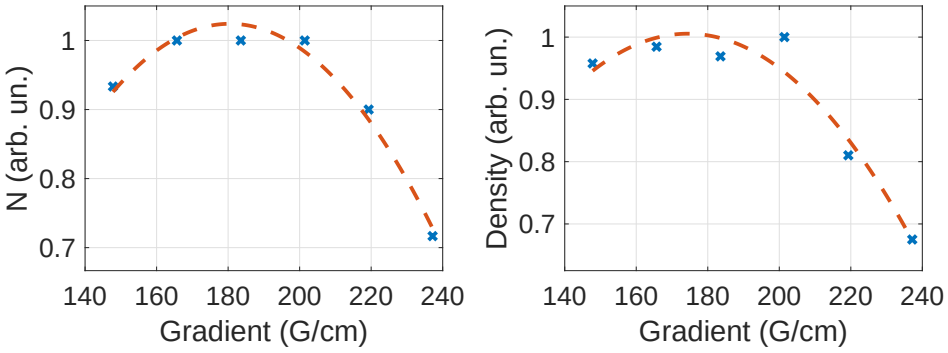

Figure 6.2: Optimisation of the magnetic field gradient during the loading of the atoms into the magnetic trap. Data (blue crosses) plotted with a quadratic fit (red dashed line). An optimal value of 176 G/cm is chosen from the maximum of the density fit. All data is measured with the atoms in the hybrid dipole trap, optimising for final PSD rather than conditions right after loading.

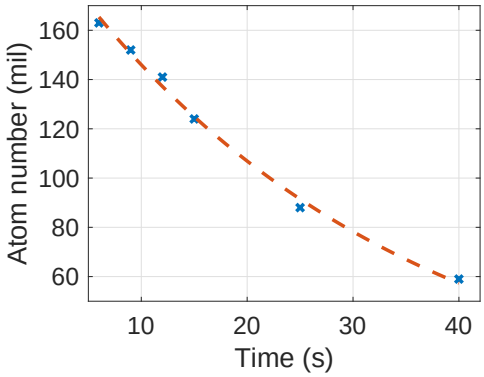

Figure 6.3: Lifetime of the atoms in the magnetic trap calculated to be 32 s from the fit. Losses are dominated by background collisions, setting the timescales available for evaporation. For the requirements for runaway evaporation see [110].

ZFL-500LN+ amplifier. To confirm atoms can be removed from the trap, the radius of the cloud is measured as a function of applied RF frequency, shown in Figure 6.4. Here, the atoms are loaded into the magnetic trap and held for 6 s, while the radio-frequency is swept linearly from 30 MHz down to a final value. As the final frequency of the sweep is reduced, a deeper cut into the distribution is visible with a smaller cloud size. A linear fit to a mean of the radii of the atomic cloud in both directions allows estimation of the magnetic field gradient, calculated from the fit to be 203 G/cm, in good agreement with the calibration of the coils which suggested a gradient of 200 G/cm. This also confirms a reasonable calibration of the absorption imaging.

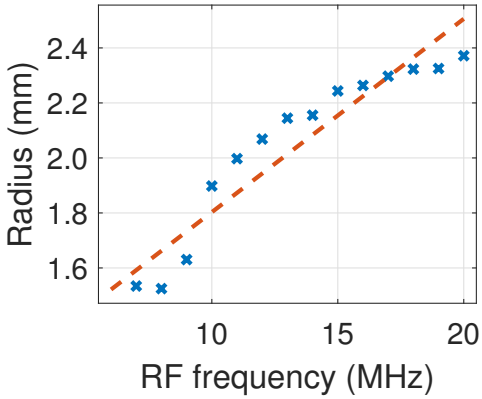

Figure 6.4: Mean of the calculated radii in orthogonal directions from Gaussian fits of an image of the atoms as a function of swept radio-frequency at 200 G/cm and a starting frequency of 30 MHz. The sweep time was 6 s, and the calculated magnetic field gradient from a linear fit (red dashed line) to the data (blue crosses) was 203 G/cm.

The RF evaporation is split into two separate sequences, allowing the maintaining of efficient evaporation without adding too much complexity to the experiment. Indeed, some groups report evaporation sequences split into 9 or more different sections [161]. The optimisation of the first RF sequence is shown in Figure 6.5. The start frequency, stop frequency, duration and gradient of the magnetic trap are all varied and the atom number, temperature and density are measured. This allows extraction of γ_{evap} [142], a parameter which describes the efficiency of the evaporation. It is calculated from

$$\bar{\gamma}_{ev} = -\frac{ln(PSD/PSD_0)}{ln(N/N_0)}, \tag{6.1}$$

where N, PSD are the atom number and phase space density after evaporation and N_0, PSD_0 are the initial atom number and phase space density before evaporation begins. This parameter describes the change in phase space density per atom lost, with positive values illustrating an increase in phase space density. The optimal values for each of the parameters are extracted from the data presented in Figure 6.5, and are set as sweeping the radio-frequency linearly from 13 MHz to 3.5 MHz in 5 s at a gradient of 176 G/cm.

Next, investigations into the RF power applied to the atoms were carried out. The signal generator could not provide enough RF power, so a Mini-Circuits ZFL-500LN+

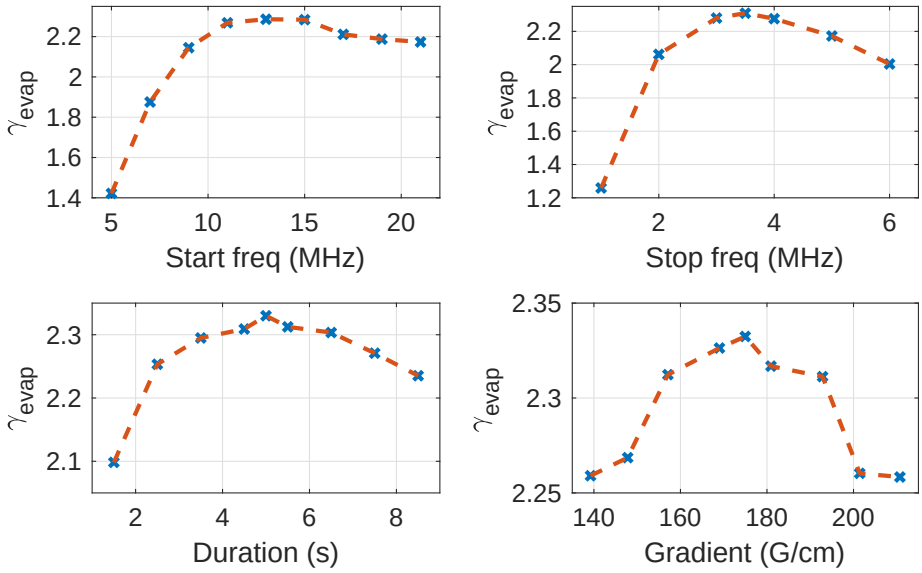

Figure 6.5: Optimisation of the first radio-frequency evaporation with respect to the start frequency, stop frequency, duration, and magnetic field gradient. Clear maxima of γ_{evap} set the chosen values for each parameter.

amplifier was implemented. A calibration of this amplifier at different frequencies was carried out, shown in Figure 6.6 to both calibrate the setpoint and confirm the amplifier's consistent working response at different frequencies. The amplifier provides 26.6 dBm of gain to the input. The RF power is swept in Figure 6.7 and the PSD recorded. Optimal set points of -4 dBm and -10 dBm for the first and second RF sweeps are chosen, corresponding to 22.6 dBm and 16.6 dBm after the amplifier. Both values are above the maximum the signal generator can supply on its own (13 dBm). At lower powers, hotter atoms are still clearly visible around the central colder cloud, having not been removed completely. This decreases the measured density of the cloud and increases the measured temperature. Above the optimal values of power, the increase in PSD saturates, as more RF power no longer removes more atoms from the trap.

Finally, the second RF evaporation was optimised against PSD, as shown in Figure 6.8. In this regime, it is more difficult to decide upon optimal values. Although the efficiency of evaporation is important, the next step in the sequence is fully loading the dipole trap dimple, where the magnetic trap gradient is lowered. The number of atoms

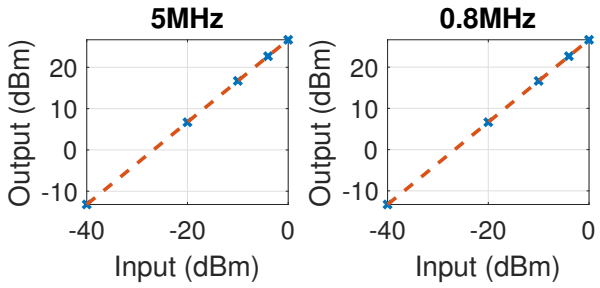

Figure 6.6: Calibration of the amplifier at different frequencies, confirming its consistent response through the evaporation process. Data (blue crosses) with linear fits (red dashed line).

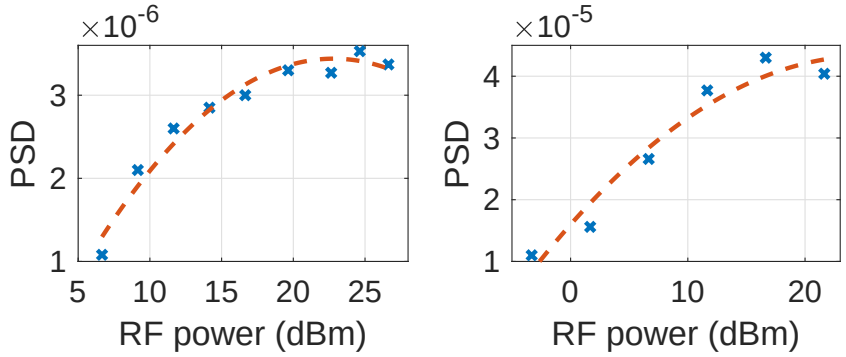

Figure 6.7: Optimisation of the RF power to the measured PSD after evaporation. Left, data (blue crosses) plotted with a guide to the eye (red dashed line) shows an optimal value of 22.7 dBm after amplification requires a setpoint for the signal generator of -4 dBm for the 1st RF evaporation. Right, the same but for the 2nd RF evaporation.

loaded into this dimple, which could then be efficiently evaporated in the dipole trap, must be considered. The dipole trap dimensions also sets a maximum cloud radius at the end of the radio-frequency evaporation, with atoms lost in the transfer if the cloud radius is too large. Furthermore, Figure 6.8 shows only γ_{evap}, and not the achieved temperature or PSD after evaporation. If the atoms are too hot, they will not load into the dipole trap dimple.

All these conditions are considered, and the parameters are set as sweeping down linearly to 0.8 MHz at a gradient of 29 G/cm in a total time of 1.75 s. The final RF frequency shows an obvious reduction in γ_{evap} below values of 0.5 MHz, with the best efficiency at 0.8 MHz. It is also determined that this value gives an adequate cloud radius and temperature, by considering further phases in the evaporation sequence. Similarly, a gradient of 29 G/cm gives both reasonable increase in PSD and an effi-

cient evaporation. Next, a duration of 1.75 s maintains the maximum measured γ_{evap}, with shorter durations showing similar efficiency but providing a lower PSD.

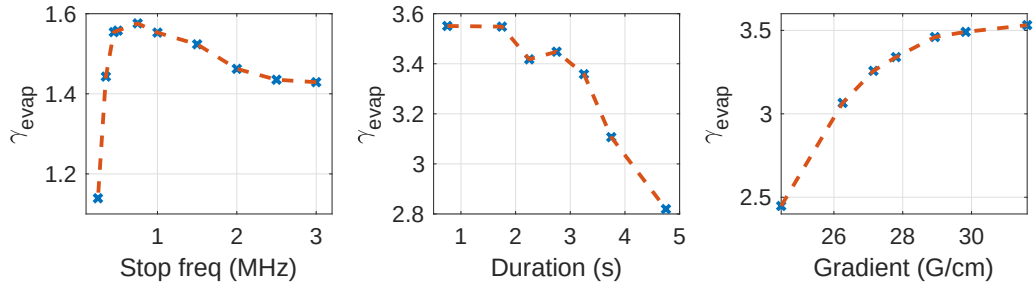

Figure 6.8: Optimisation of the final radio-frequency evaporation. The efficiency is considered through the parameter γ_{evap}, giving an optimal evaporation by sweeping linearly to 0.8 MHz in 1.75 s at a gradient of 29 G/cm. Further detail in the text.

6.2 Hybrid Trapping

After evaporation in the magnetic trap, the atoms are loaded into the dipole trap dimple of a hybrid trap. The laser used for the dipole trap is an IPG Photonics YLR-20-LP, which produces up to 20 W of optical power at a wavelength of 1070 nm. For confirmation of working condition and maximum power available, the output power directly after the coupler was calibrated against set-point, shown in Figure 6.9

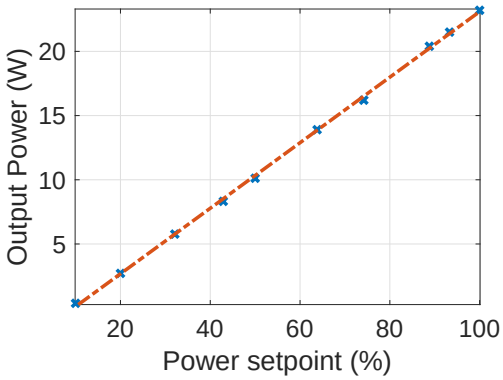

Figure 6.9: Power calibration of the YLR-20-LP laser directly at the output of the fibre. This dictates the maximum optical power available for dipole trapping.

The optical setup used for dipole trapping is shown in Figure 6.10, and will be described in detail next. It provides stabilisation, focusing and alignment of the beams to generate trap depths deep enough for evaporation to condensation.

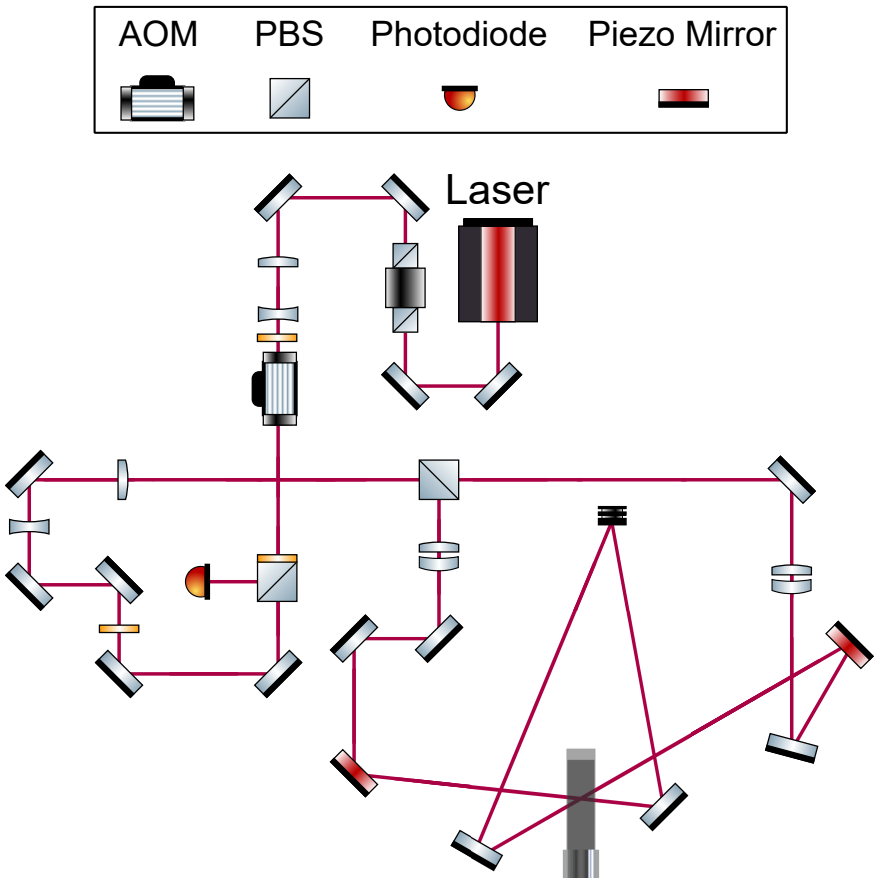

Figure 6.10: Optical diagram for the DT alignment. After passing through an optical isolator and an AOM, the beam is sampled for stabilisation of the potential depth. The beam is then resized and focused onto the atoms. Piezo actuated mirrors allow for fine movement of the dipole trap position with respect to the magnetic trap centre.

6.2.1 Stabilisation system

Evaporation in the dipole trap relies on precise control and ramping down of the laser's intensity. The stabilisation system begins by monitoring of the total power sent to the atoms. A Thorlabs VA5-1064/M combined half waveplate and beam splitter system extracts light to be measured by a Thorlabs DET36A photodiode. This measure is amplified and sent to an SRS SIM960 PID. An overview of the stabilisation system can be seen in Figure 6.11. It can be split into two sections, the double frequency driving of the AOM to mitigate thermal drift, and the monitoring of the dipole trap power by a photodiode.

The power at the atoms, measured for each beam separately is shown in Figure 6.12. The amplitude modulation of the 95 MHz is increased to its maximum value,

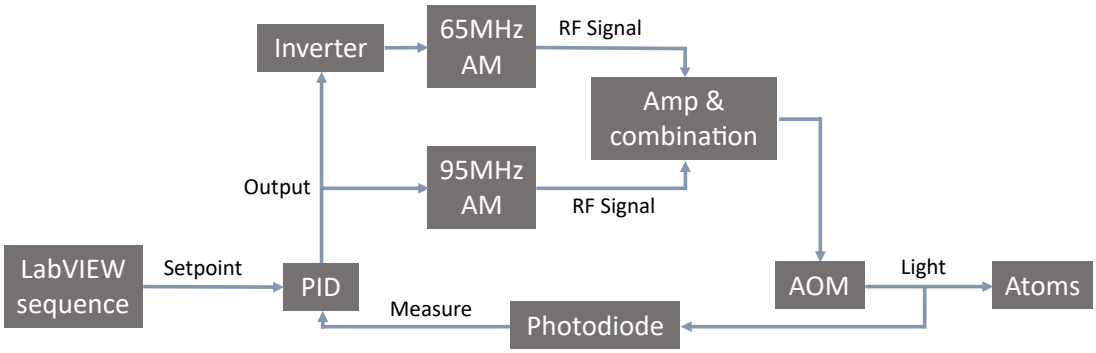

Figure 6.11: Overview of DT stabilisation system, further detail in the text.

changing the measured photodiode voltage, and an 1000:1 attenuator is used to measure the power at the atoms. A maximum of 7 W of optical power at the atoms is available.

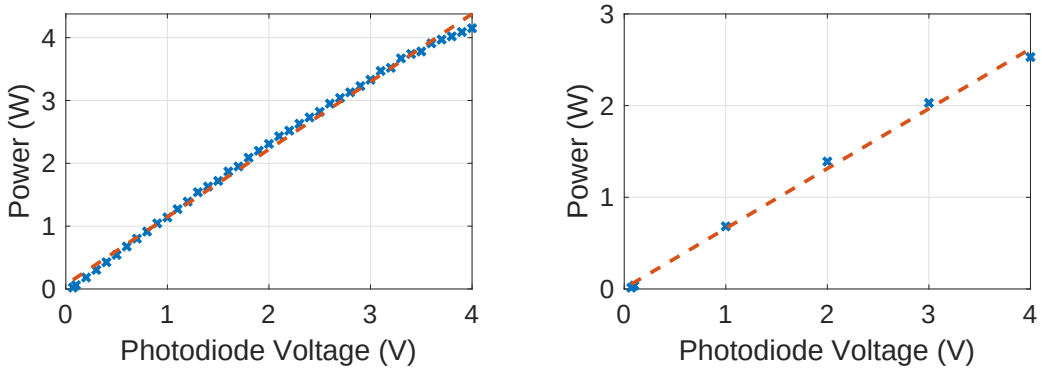

Figure 6.12: Calibration of the dipole trap power to the photodiode voltage, measured at the atoms for the two beams separately.

Next, double frequency driving is used to maintain constant RF power being sent to the AOM. A similar technique was also successfully implemented for the MOT cooling beams, described in Section 4.2. As the AOM changes temperature, beam position can vary dramatically. Frequencies of 65 MHz for the dipole trap 'off' and 95 MHz for the dipole trap 'on' are chosen to maximise extinction (by blocking spatially) whilst remaining within the AOM bandwidth (to not limit maximum trap depth). The PID output stabilises the dipole trap power by acting on the 95 MHz amplitude modulation. This output is also inverted, and sent to the 65 MHz amplitude modulation, illustrated in Figure 6.13. Both signal generators are set to output 5 dBm, and have a linear response to external DC amplitude modulation in the range ± 1 V. To

allow for some margin, the PID output limits are set to ±1.2 V, and its gain values (P,I,D) are then tuned in the standard way (different options are discussed in the manual). The two signals are then combined and amplified before being sent to the AOM.

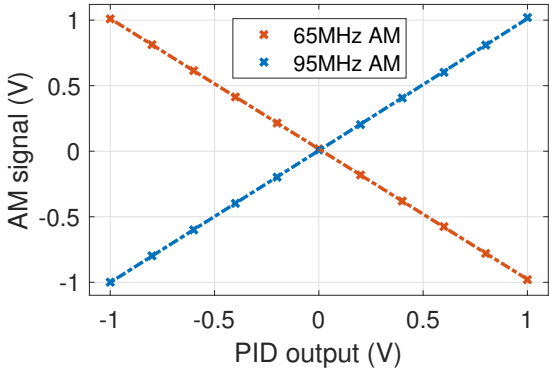

Figure 6.13: Voltage inverter used for double frequency driving of the dipole trap AOM. The amplitude modulation voltage is inverted for the two frequencies, so that the total RF power sent to the AOM is constant throughout the sequence.

6.2.2 Beam size

To achieve the tight focus at the trap, the beams are expanded by a telescope (x4, f = 50 mm & 200 mm) before passing through a diffraction-limited lens (Thorlabs AC254-500-C achromatic doublet). The beam waist, w_0, set by the diffraction limit can be written as

$$w_0 = \frac{4\lambda F}{\pi D} \tag{6.2}$$

where λ is the wavelength of the light used, F is the focal length of the lens and D is the spot size of the beam at the lens. Therefore, by increasing the spot size at the lens and choosing the shortest focal length lens which can be installed on the setup, the smallest beam waist at the trap is achieved. The focal length of the lens can be substituted with the effective focal length, due to a diverging input beam. The effective focal length was measured to be 700 mm, compared with the actual focal length of the lens which is 500 mm. The input beam spot size is measured at 12 mm. Therefore, using a 1070 nm laser gives a calculated diffraction limited beam waist of 79.5 µm, in good agreement with experimental results. The lenses are mounted on translation stages, along the line of the beam, for control of the focus position. The waist of

the dipole trap beams at the position of the atoms was measured using a CINOGY CinCam CCD beam profiler, with results shown in Figure 6.14.

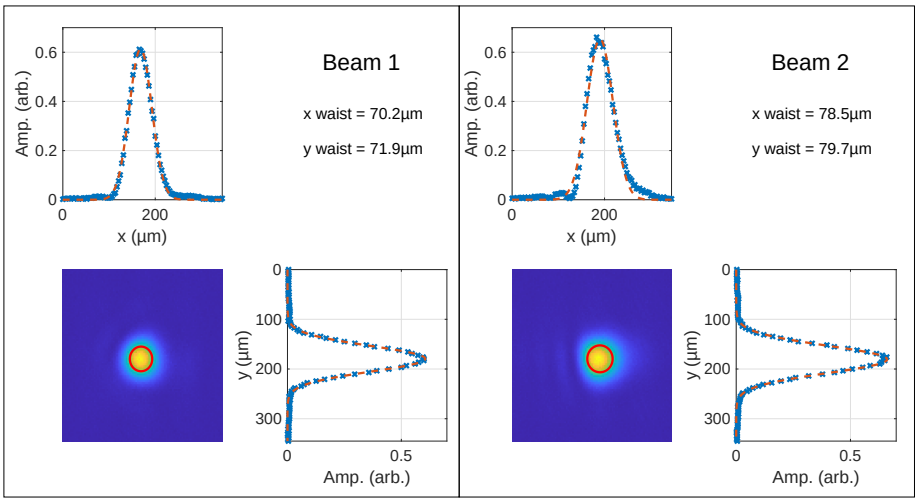

Figure 6.14: Beam size determined using a CINOGY CinCam beam profiler, with an image of the beams and cross sections with Gaussian fits shown. The average beam waist is calculated to be 75 µm.

6.2.3 Trap loading

With a mean waist of 75 µm and the 7 W available power at the atoms, the dipole trap is deep enough for efficient transfer of 2 µK atoms from the magnetic trap. Two or three mirrors after a final lens allows fine control of dipole trap position. The final mirror of both beams are mounted to an Agilis AG-M100N piezo mirror mount. These mounts, driven by an Agilis AG-UC8 controller, provide computer control of the dipole trap's position. Movement of the mirrors is done in arbitrary 'steps'. Scanning the two axes of each mirror, and monitoring atom number in the trap after the second RF evaporation is shown in Figure 6.15. Each scan of the beams is done separately with the other beam blocked manually. Furthermore, all available dipole trap power is routed to the beam under investigation. A clear reduction in the number of atoms is seen when the dipole trap beams are aligned to the magnetic field zero, as expected theoretically due to spin flips. For both beams, the atom number increases slightly at the centre of the trap when scanned horizontally. This is attributed to inhomogeneity in the magnetic field. The beams are left in the position which maximises the number of atoms in the dipole trap dimple, one dipole trap waist away from the centre of the

magnetic trap.

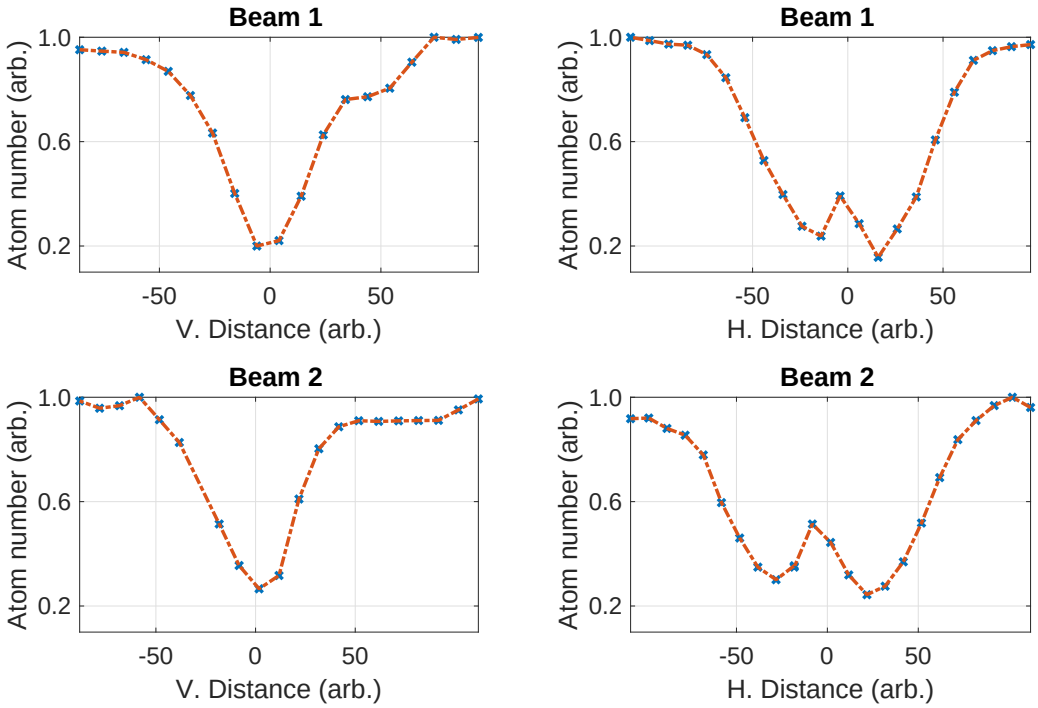

Figure 6.15: Alignment of the dipole trap by moving the Agilis AG-M100N mirror mounts in steps. For each alignment, only one beam was incident onto the atoms. Both horizontal and vertical alignment sweeps are shown. A clear reduction of the atom number (blue crosses, red dashed line to guide the eye) in the magnetic trap is seen when the dipole trap is aligned to the magnetic field zero. This is used as a reference point, to move the beams one waist away from the magnetic field zero.

Thermal instability of the system affects beam alignment to the atoms. This is most obviously seen as the high power laser is turned on. The 20 W of optical power changes the AOM temperature and optics significantly, causing the dipole trap beams to move relative to the atoms. This is shown in Figure 6.16, where the atom number and density is recorded for 30 min after the dipole trap is turned on. Once this initial drift stops, fine alignment can be retuned by moving the piezo mirrors. Daily maintenance is required for the evaporation to maintain efficiency and the maximum atom number to be seen in the dipole trap. Automatic solutions to this problem have been suggested, such as a four quadrant photodiode with a closed feedback loop, but have yet to be implemented.

With the optimal position of the dipole trap beams with respect to the magnetic

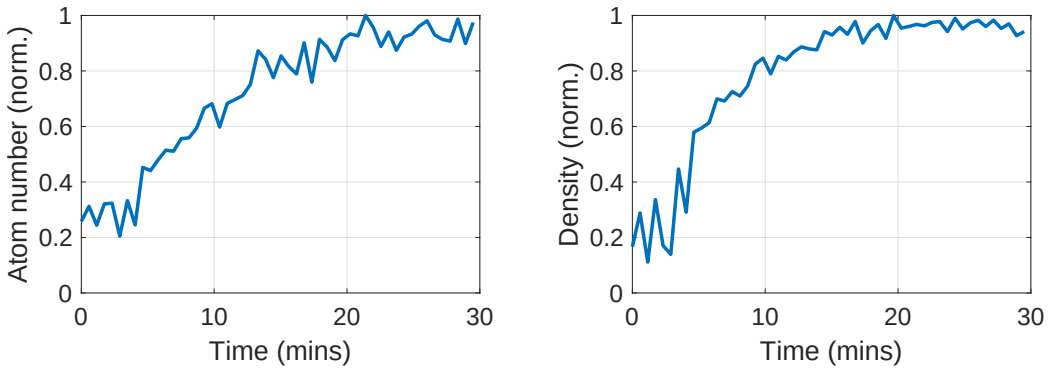

Figure 6.16: Atom number measurements after turning the dipole trap laser on. Whilst laser, AOM and optics thermally stabilise the dipole trap beams move, eventually reaching the optimised position.

trap decided on, the balance of power between the two beams is optimised. Initial efforts found a polarisation problem, whereby the power in the two arms of the dipole trap could not be adequately varied with the HWP before the PBS, as shown in the left panel of Figure 6.17. It was found that in an effort to increase the beam path length, allowing for the AOM orders to separate spatially, some mirrors were placed at non-optimal angles to the beam. The manufacturer states a recommended 45° angle of incidence (AOI) for consistent reflectance of S and P polarisation from the E03 coating, and so investigations into mirror angle against extinction ratio on the PBS were carried out. The estimated angle of the mirror is plotted against the measured extinction ratio at one of the arms of the PBS in the right panel of Figure 6.17. With such a large variation in extinction ratio, all mirrors in the dipole trap alignment were placed at 45° to the beam. Next, the power balance between the two arms of the dipole trap is investigated. The angle of the HWP before the PBS which splits the two arms of the dipole trap is varied, and the atom number in the dipole trap dimple is recorded, shown in Figure 6.18. A 38 % to 62 % split of the total beam power is found to be optimal.

Transfer is further optimised by sweeping an offset magnetic field in the $\hat{z}$ direction. This allows for fine alignment of the vertical position of the magnetic trap zero with respect to the dipole trap. A dedicated set of coils allow for fine sweeping of the field in this direction. These have the same dimensions and turns as the 'Z Comp'

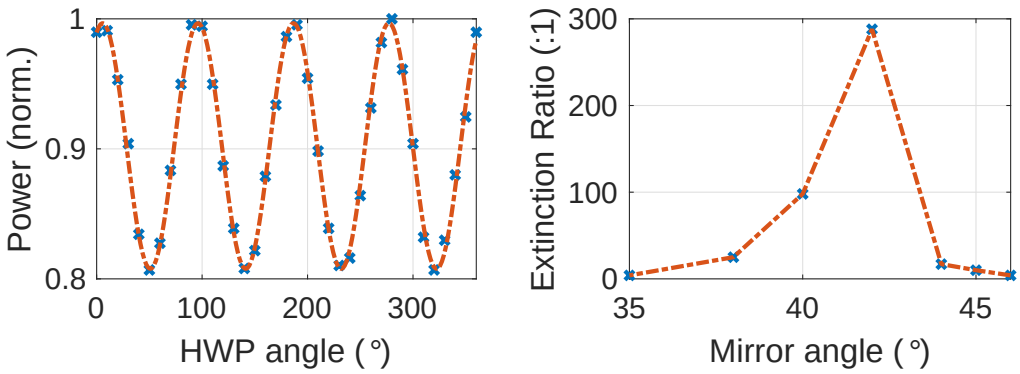

Figure 6.17: Left, the HWP angle against power measured in one arm of the PBS with non-optimal AOI. The power can only be reduced by 20 %, limiting the ability to distribute the power among the two dipole trap beams. Right, estimated mirror angle against the measured extinction ratio. By changing the AOI the manufacturer quoted extinction ratio at the PBS could be regained.

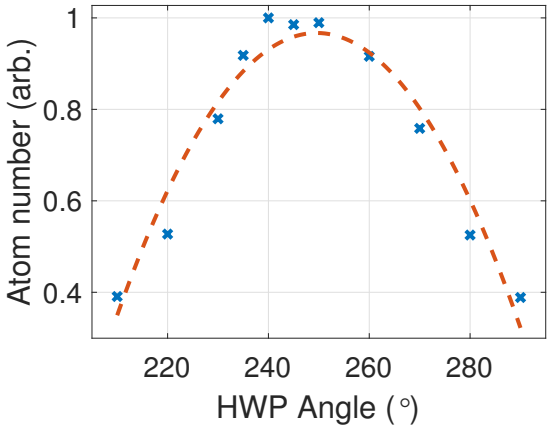

Figure 6.18: Half-wave plate optimisation to balance the power in the DT. The optimal value was found to share evenly the total power available from the dipole trap laser.

coils previously described (8 turns, 46 mm radius, Helmholtz winding) and are powered by a Kepco BOP 36-6DL4886 power supply, providing up to ± 6 A. The bipolar power supply allows control of the current via an input control voltage, sent directly from the DAQ which controls the overall sequence for the evaporation. Figure 6.19 shows a calibration of the setpoint voltage to the applied field at the atoms. This fine control of field proved paramount to achieving efficient evaporation. The right panel of Figure 6.19 shows optimisation of the setpoint for the dipole trap loading, with the density recorded as the field is swept.

Once loaded, the lifetime of the atoms in the dipole trap can be measured, shown

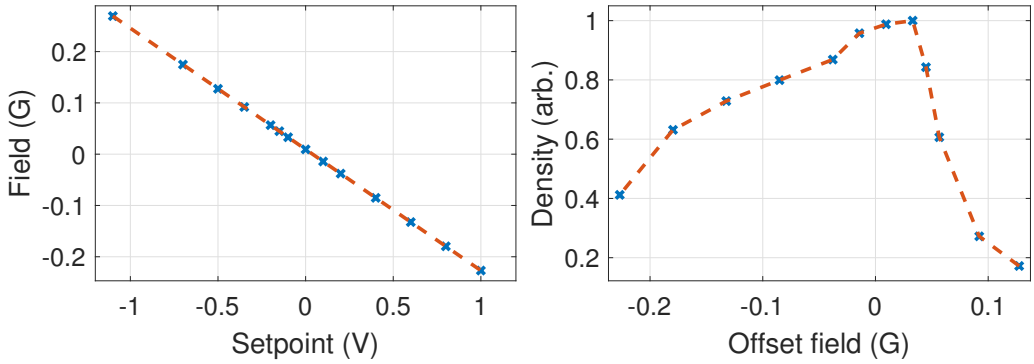

Figure 6.19: Left, calibration of the offset field, used for fine alignment of the vertical position of the magnetic trap zero with respect to the dipole trap. Right, density of the atoms when transferred from the magnetic trap to the dipole trap, optimised against the offset field value at this point in the sequence. With fine tuning of the offset field a considerable increase in density can be achieved.

in Figure 6.20. This lifetime agrees with the magnetic trap lifetime, suggesting both are limited by collisions with background atoms (the pressure in the vacuum chamber). The exponential fit gives a lifetime of 35 s.

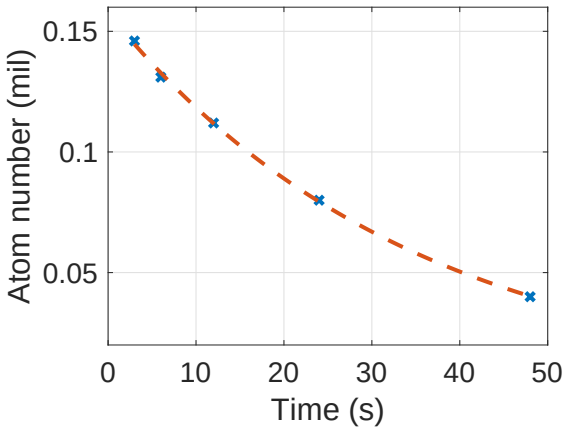

Figure 6.20: Lifetime of the atoms in the dipole trap calculated to be 35 s from the fit, similar to the lifetime of the atoms in the magnetic trap, confirming that losses are dominated by collisions with background atoms.

6.2.4 Evaporation

There are two phases to the evaporation in the dipole trap. Firstly, the magnetic field gradient is lowered in 3 s to 6.6 G/cm and the dipole trap power is reduced from maximum to 510 mW, giving an immediate increase in PSD from 8×10^{-4} after the RF evaporation in the magnetic trap to above 6×10^{-2}. This is the phase where the

bulk of the evaporation happens, as there are only 200k atoms left and the PSD is only an order of magnitude away from condensation. Optimisation of the dipole trap total power and magnetic field gradient for this phase is shown in Figure 6.21. Further increase in PSD can be achieved if the gradient is reduced past the optimal value, however the evaporation eventually stalls and condensation is not achieved. This is due to the evaporation efficiency being greatly reduced when decreasing the magnetic field gradient below 6.6 G/cm.

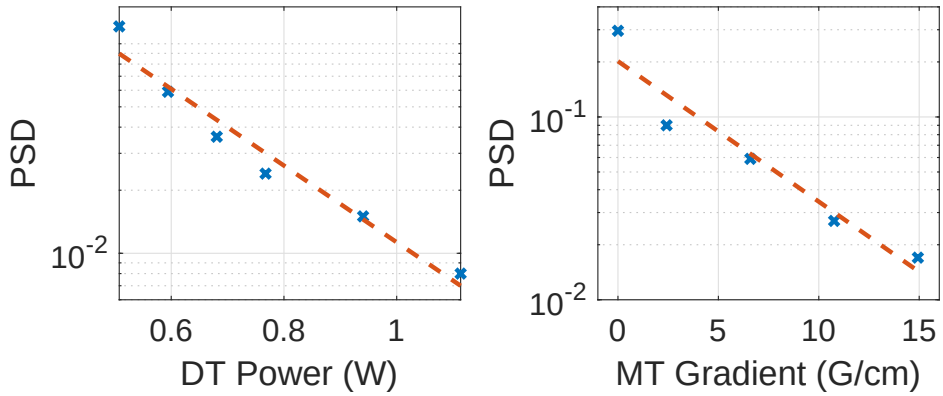

Figure 6.21: Optimisation of the dipole trap dimple loading against the dipole trap power and magnetic field gradient. Left, the dipole trap power is swept and the PSD recorded. Right, the same but for the magnetic field gradient. Optimal values of 510 mW and 6.6 G/cm are used.

Next, the evaporation is pushed further until the formation of a Bose-Einstein condensate. The dipole trap power is lowered to a final value of 300 mW. However, the magnetic field gradient must increase from the previous phase to 16.5 G/cm. This value of field gradient is close to the 15.26 G/cm required to levitate the atoms against gravity. The optimisation of this evaporation to condensation is shown in Figure 6.22. Observations of the BEC are shown in Chapter 7, where the overall evaporation sequence is summarised.

6.3 Magnetometry

With consistent BEC production, the experiment focus shifted to performing magnetometry with the ultracold atoms. This section will describe experimental upgrades made to the magnetometry phase of the apparatus. Key improvements necessary to

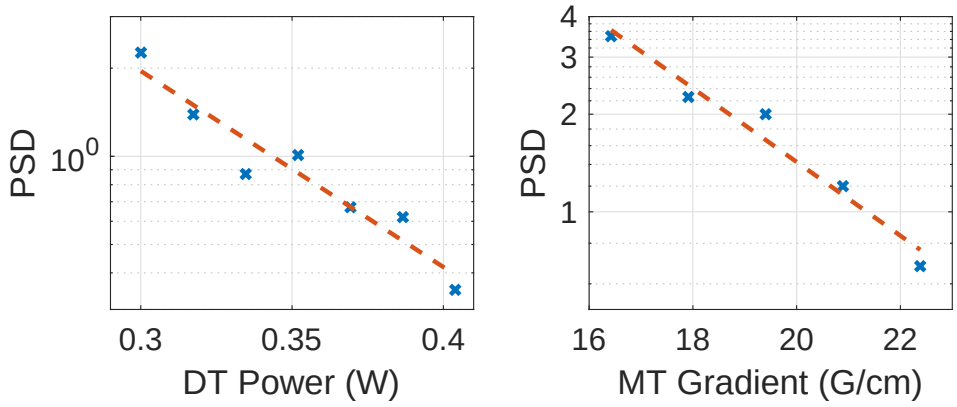

Figure 6.22: Optimisation of the final evaporation against the dipole trap power and magnetic field gradient. PSD high enough for BEC production are achieved with a final dipole trap power of 300 mW and magnetic field gradient of 16.5 G/cm.

measure magnetic fields with a BEC are highlighted.

6.3.1 Probe beam

The diode on the previously installed RadiantDyes probe laser stopped functioning. Therefore, a new probe beam was produced from spare cooling beam power. The setup is shown in Figure 6.23, where light directly from the output fibre of the cooling beam is extracted. A double pass AOM configuration increases the detuning of the probe to +330 MHz (chosen as this is the maximum detuning which can be achieved with this laser and AOM setup), before the probe beam is injected into a fibre to be passed across the optical table. At its output, an AOM, photodiode and PID lock the intensity of the probe beam behind a shutter. The shutter is only open for the duration of the measurement. Two lenses expand the beam, and a half wave plate balances the two arms of the polarimeter for maximum sensitivity.

The 20 W of optical power from the dipole trap leads to a significant amount of scattered light. This interferes with the probe power locking by increasing the measure of the photodiode in the feedback loop. Table 6.1 illustrates the difference in measurement with the dipole trap turned on/off. Clearly, the feedback loop can not work effectively. With the dipole trap at considerably different wavelength to the probe beam (1070 nm), a 780 nm filter was placed on the photodiode, ensuring only the probe beam intensity is measured. Indeed, with the filter in place, a negligible

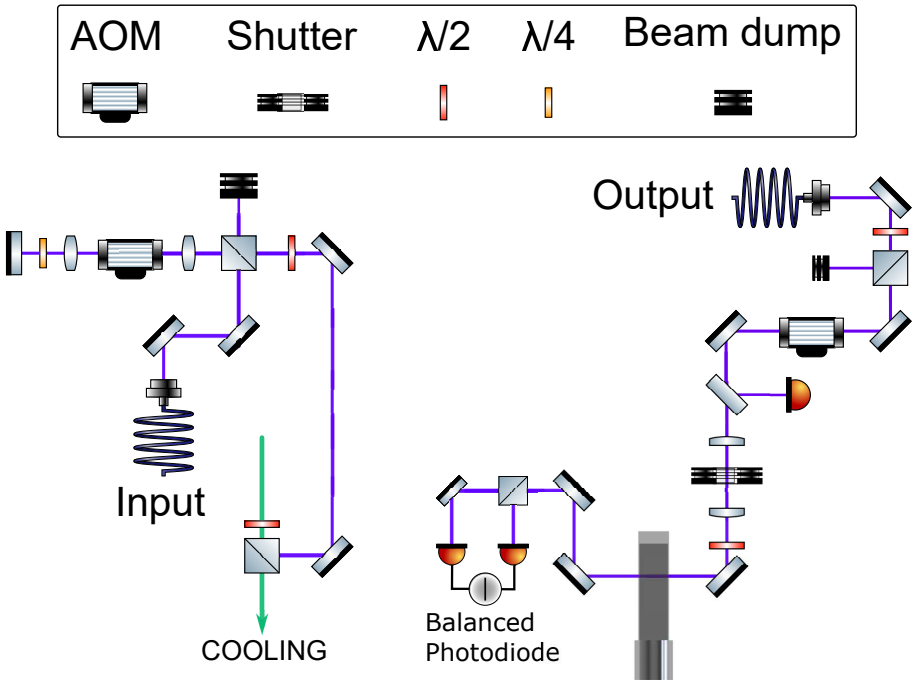

Figure 6.23: Probe beam produced from extraction of cooling light. The cooling beam is split by a PBS, with 150 mW directed towards the double pass AOM. 35 mW at the output of the fibre is intensity stabilised by a closed feedback loop. A shutter opens for the duration of the magnetometry measurement, where the probe beam's polarisation is monitored by a polarimeter consisting of a PBS and a balanced photodiode.

difference between the measured photodiode voltage for the dipole trap on/off is seen. Further problems of scattered light arise from the near resonant nature of the probe beam. Although much weaker than the dipole trap, the new probe beam produces up to 75 mW at the output of the fibre. Stray probe light proved catastrophic for the BEC production, with no atoms seen at the end of the evaporation when the new probe beam was first installed. Partitions within the setup had to be installed, ensuring no scattered light from the probe beam reached the atoms, and the BEC was regained.

	Photodiode Measure (mV)	
	Filter	No Filter
DT off	343	686
DT on	348	10190

Table 6.1: Photodiode measure values with the dipole trap on and off. A 780 nm filter allows for stabilisation of the probe power without interference from the dipole trap light.

Once filtered, the new probe power was optimised to the measured sensitivity in the magnetic trap, shown in Figure 6.24. The optimal probe power setpoint of 12 mV corresponds to an intensity of 568 $\mu W\,cm^{-2}$. With the double pass AOM, and the single pass AOM after the fibre, the total probe detuning is +330 MHz from the ^{87}Rb $5^2S_{1/2}, F = 2 \rightarrow 5^2P_{3/2}, F' = 3$ cooling transition.

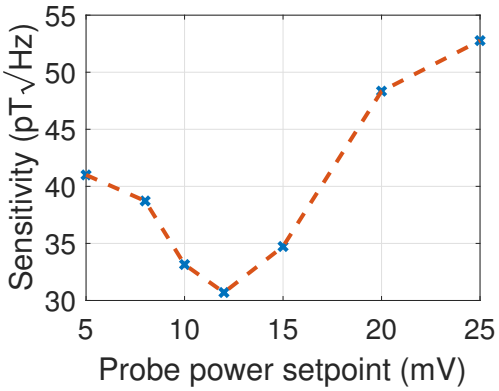

Figure 6.24: The probe power optimisation. Sensitivity is measured with the probe power swept. An optimal setpoint of 12 mV is used.

6.3.2 Active bias field compensation

The work in this section follows the ideas presented in [57]. In the reference, active stabilisation of the bias field is implemented using a closed feedback loop. A 2x improvement in sensitivity is quoted. It is interesting to note that the magnetometer is more sensitive to magnetic field noise in the bias field direction due to the summation in quadrature of the orthogonal components when calculating the total field, shown in Equation 5.2. With the field in the bias field direction typically two orders of magnitude larger than the transverse directions, a small noise in this direction results in a larger perturbation to the total field.

To implement active stabilisation, the magnetic field near the sensor in the bias field direction must first be measured. This is done using a Stefan Meyers Instruments FLC100 fluxgate magnetometer. The fluxgate can measure between $\pm$ 100 μT, DC to 1 kHz. In order to place the sensor near to the cell, the RF coil mount (used to calibrate the magnetometer) was redesigned to also hold the fluxgate, shown in Figure 6.25. Once in place, the fluxgate's measure was calibrated against the current in

Figure 6.25: The 3D printed mount, to scale, used to hold both the RF calibration coil and the FLC100 fluxgate magnetometer. 10 turns of copper wire are wound around the mount, with a side length of 3.1 cm.

the compensation coils in the $\hat{z}$ direction. This is shown in Figure 6.26. To confirm the fluxgate is well aligned to the bias field axis, the measure is also recorded whilst changing the current in the compensation coils in the $\hat{x}$, $\hat{y}$ directions. The maximum change in measure is $>$10x smaller over the same explored range in field. Next, the

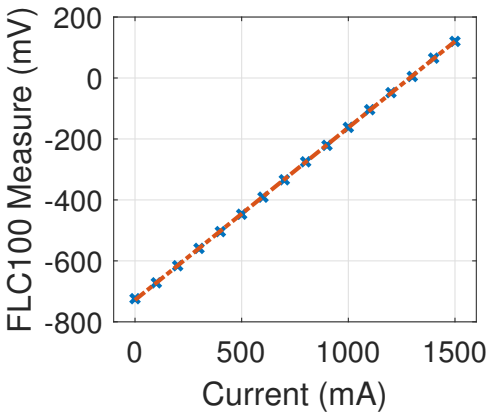

Figure 6.26: Calibration of the FLC100 fluxgate magnetometer's measure against the current in the compensation coils in the $\hat{z}$ direction.

fluxgate must work consistently even when exposed to large magnetic field gradients, such as those produced during the magnetic trapping. The output of the fluxgate was recorded during the sequence for BEC production, shown in Figure 6.27. Indeed, the fluxgate returns a consistent measure for the different parts of the sequence even when exposed to large gradients. However, when the gradient is highest, the fluxgate's measure saturates at $-2.5\,\mathrm{V}$. This prohibits the active stabilisation working during the entire sequence. Instead, the stabilisation must be turned on just before the magnetometry phase. To this end, a dedicated Helmholtz coil in the $\hat{z}$ direction is wound with the same dimensions and number of turns as the existing compensation coil. A

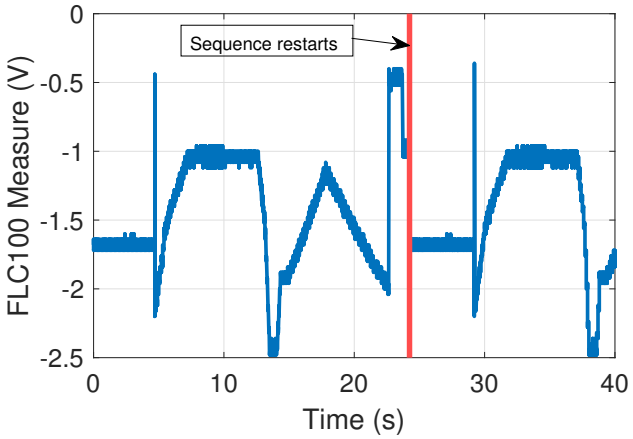

Figure 6.27: FLC100 measure during the sequence for BEC production. As the sequence runs, large magnetic field gradients saturate the measure of the FLC100. This does not affect its operation, but prohibits continuous stabilisation of the bias field.

solid state relay (SSR) is implemented to switch the stabilisation. The coil is connected to both this SSR and a MOSFET. A PID acts on the gate of the MOSFET for current control, and the SSR connects and disconnects the coils from the circuit when triggered by the sequence.

The PID error when switching is shown in Figure 6.28. The trigger is when the magnetometry measurement takes place. Clearly, the error is zeroed correctly by the PID during the measurement. To compare the performance of the atomic magnetome-

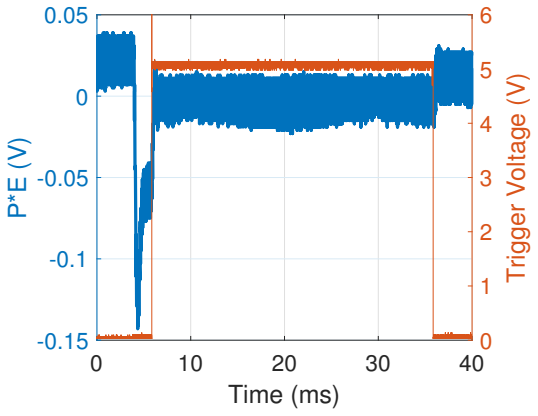

Figure 6.28: The PID locking the FLC100 measure. When the trigger is sent (orange line), the PID acts to zero the measured error, which is the difference between the set voltage and the measured voltage.

ter with and without compensation, five consecutive measurements of the magnetic

resonance were taken in the two working conditions. Each in-phase (X) response of the resonance was fitted separately to a Lorentzian function, leading to the data presented in Table 6.2.

	HWHM (kHz)	Amplitude (mV)	R^2
PID off	1.52	21.4	0.67
PID on	1.11	24.9	0.83

Table 6.2: Comparison of the active bias field stabilisation. Magnetic resonances are recorded, and the in-phase (X) response is fitted with a Lorentzian, defining a width (HWHM), amplitude and R^2. The mean values of ten separate resonances, five with and five without stabilisation are reported.

Next, the data was averaged. The average was then fitted, considering the agreement of consecutive sweeps with respect to each other. This is shown in Table 6.3, and again the magnetometer performs better with the bias field stabilisation. In all cases amplitude, width and goodness of fit improve with the stabilisation active.

	HWHM (kHz)	Amplitude (mV)	R^2
PID off	2.03	18.6	0.86
PID on	1.57	21.2	0.94

Table 6.3: Active bias field stabilisation data, the mean values of 10 separate sweeps, 5 with and 5 without stabilisation are reported.

6.3.3 Phase sensitive detection

The available AMETEK 7230 lock-in amplifier is limited to a maximum frequency of 120kHz. To increase the explored frequency range of the magnetometer, an offline lock-in amplification procedure is developed. Here, polarimeter signals at different frequencies are acquired with an oscilloscope, in the same way the signal to noise ratio of the magnetometer is determined. Generally, during lock-in amplification an input is multiplied by a reference signal,

$$V_{psd} = V_s sin(\omega_s t + \phi_s) V_r sin(\omega_r t + \phi_r), \tag{6.3}$$

which after passing through a low-pass filter, collapses to

$$V_{psd} = \frac{1}{2} V_s V_r cos(\phi_s - \phi_r), \tag{6.4}$$

where only signals at the reference frequency survive. By setting $V_r = 1$ and matching ϕ_r to the phase at resonance, we arrive at the simple result that $V_s = 2V_{psd}$. Using this, an offline phase sensitive detection procedure can be implemented.

First, the procedure was tested on a simulated signal. 100 simulated polarimeter signals are produced, with the phase changing from 5° to 175°. The amplitude is ramped from 0.5 up to 1 at resonance and then back to 0.5 linearly. White noise, at 20% depth, is added to each signal before multiplication with a reference signal. The mean of the product is calculated and doubled, giving V_s at each frequency. Indeed, the offline procedure allows phase sensitive detection, shown in Figure 6.29.

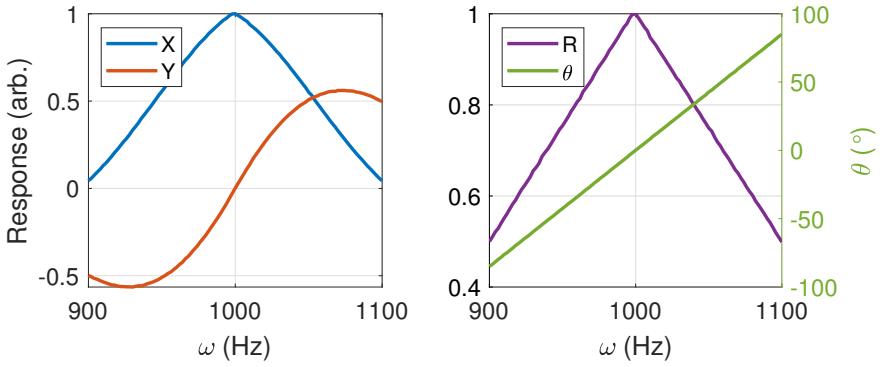

Figure 6.29: Simulated signal phase sensitive detection. White noise, at 20% depth, is added to an oscillating signal which is multiplied by a reference signal. The mean of the product is taken and plotted for each frequency. The correct amplitude and phase of the signal relative to the reference is extracted.

However, once tested on real data, a resonance could not be extracted. This was attributed to a triggering problem, where the phase of successive shots was scrambled. By operating the Keysight 33120A signal generator in 'burst mode', which outputs based on a trigger, the phase angle is reset to zero for each run. This is illustrated in Figure 6.30, where on the left a random phase between successive measurements at the same frequency is shown, and on the right consistent phase is regained after operation in 'burst mode'.

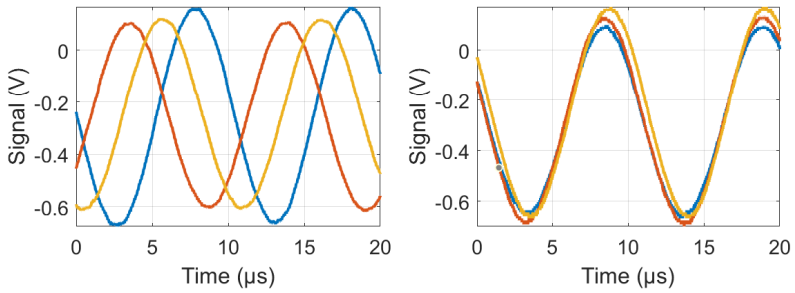

Figure 6.30: Three successive polarimeter signals measured at the same output frequency in normal (left) and 'burst' (right) mode. The phase between measurements changes when the signal generator is not triggered.

Implementation of the burst mode operation allowed for a clear resonance to be extracted. Raw data from the lock-in amplifier is compared to that from the offline phase sensitive detection procedure described. This is shown in Figure 6.31, where similar resonances are extracted from both detection methods.

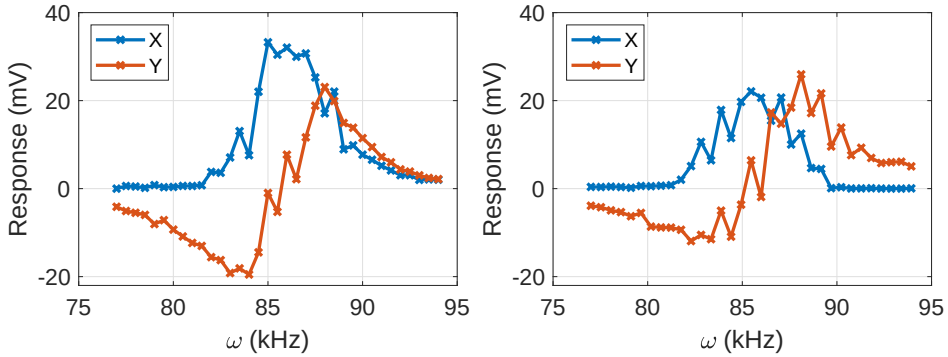

Figure 6.31: Offline phase sensitive detection. Left, the X,Y measured at different radio frequencies with the offline procedure. Right, a similar resonance obtained from the AMETEK 7230 LIA.

6.3.4 Magnetometry delay

The resonance was probed with the atoms at different phases in the evaporation. The obtained SNR decreases due to the reduction in atom number as the sequence progresses, initially seeing no magnetometry signal after the second RF evaporation. Work to improve the signal to noise ratio, especially in later parts of the sequence, is detailed next.

Firstly, consideration into the magnetic field switching (both the gradient and DC fields) led to implementations of a wait phase before magnetometry is performed. The

measured sensitivity in the magnetic trap is plotted against this wait time in Figure 6.32. An optimal value of 2 ms was found, giving over two times improvement in sensitivity. This is illustrated further in the next two panels of Figure 6.32, where the resonance with the atoms just after the first RF evaporation is plotted with the wait off and on. Clearly, the resonance is improved, with the HWHM decreasing from 4.2 kHz to just 1.1 kHz. As mentioned, this was attributed to the switching time of all coils present in the experiment, and gives the active bias field compensation's PID time to settle.

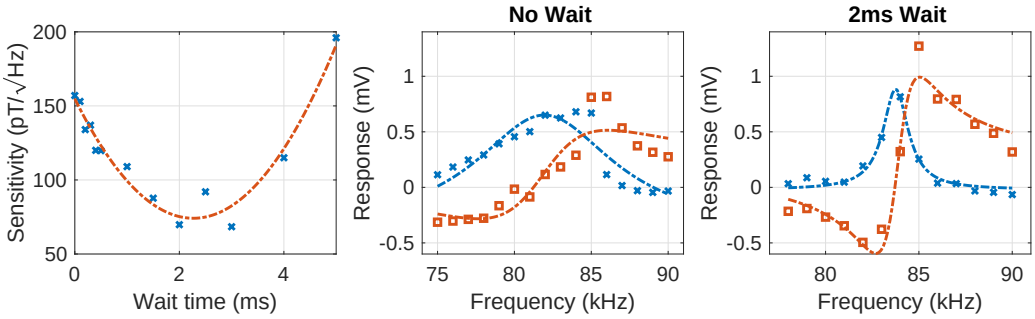

Figure 6.32: Adding a delay between the magnetic trap switching off and magnetometry. Left, the sensitivity in the magnetic trap against this wait time. Middle, the resonance with no wait in the first RF evaporation phase of the sequence. Right, the same but with a two millisecond wait.

6.3.5 Re-optimisation

During the radio-frequency evaporation in the magnetic trap, the bias field direction changes, due to separate optimisation of the bias field magnitude and direction at each phase of the sequence. The setpoints of the power supplies which drive the bias field producing coils throughout the sequence are shown in Table 6.4. There are many ways an estimation of the field can be made using these setpoints, for example through conversion to current and using the coil parameters or by measuring the response of a fluxgate. However, the most accurate way is to use the radio-frequency magnetometer which consists of the atoms themselves. This is shown in the left panel of Figure 6.33, where the resonant frequency of the magnetometer was measured for different setpoints of the bias field offset coil, converted to field through the gyromagnetic ratio (0.7 MHz/G). As the setpoint increases, the resonant frequency measured decreases

until passing through zero at 0.5 V, before increasing again. This is the point at which the magnetic field changes direction. When performing magnetometry with the atoms in the early stages of evaporation, setpoints below 0.5 V are used. However, using similar setpoints for atoms after the 2nd RF evaporation sees a large reduction in measured sensitivity. This sudden switching of the bias field sees the initial atomic spin polarisation degrade, as the spins cannot follow the fast change in direction of the field (in a similar way to Majorana flops in a magnetic trap). The dependence of the magnetometer's sensitivity on this initial spin polarisation is discussed in Section 2.3. A comparison of the extracted magnetic resonances is shown in the middle and right panels of Figure 6.33.

	MT	1st RF	2nd RF	DT Load	BEC
Setpoint (V)	0	-0.45	1.5	1.8	3.5

Table 6.4: Optimised setpoint of the current controlled bipolar power supply which supplies current for the compensation coil in the bias field direction ($\hat{z}$) as the sequence progresses.

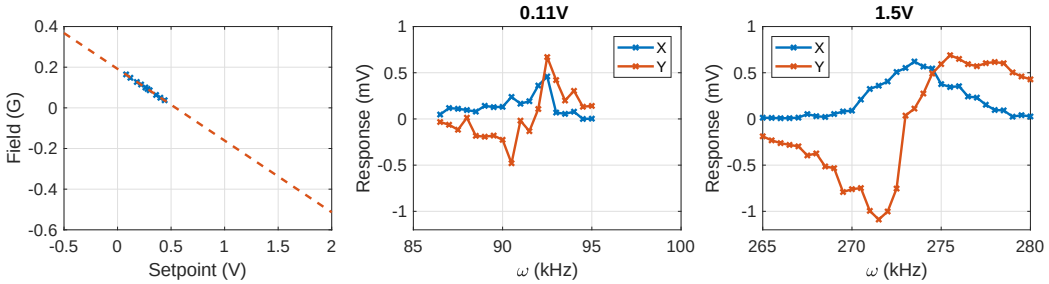

Figure 6.33: Left, the field at the atoms as the setpoint in the bias field offset coil is changed. Data (blue crosses) are converted resonant frequency measurements from the cold atom magnetometer with a linear fit (red dashed line) extrapolated for a larger range in setpoint. Middle, the magnetic resonance of atoms after the 2nd RF evaporation with the offset field setpoint of 0.11 V. Right, the same but with the field now set at 1.5 V.

With the bias field direction changing, a re-optimisation of the transverse fields is performed. In addition, gradient compensation is also implemented. All are optimised in the usual way, with transverse compensation considering the resonant frequency of the magnetometer whilst gradient compensation is optimised for minimum linewidth. This is shown in Figure 6.34. These upgrades, as well as smaller changes such as

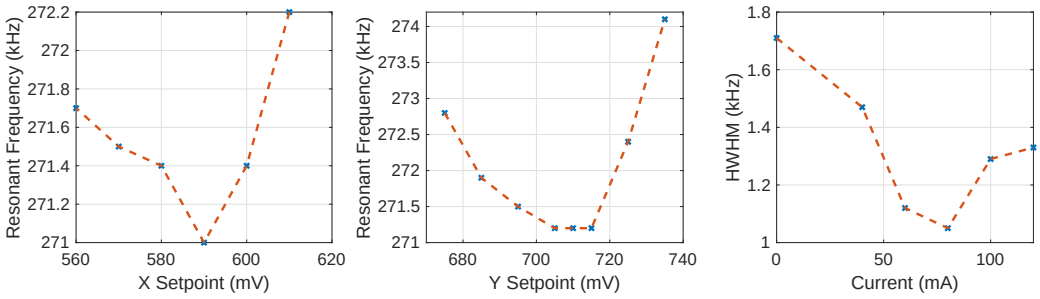

Figure 6.34: Compensation of transverse fields (left, middle) set by sweeping the bipolar setpoint and deducing the magnetometer's minimum resonant frequency. Right, optimisation of the magnetic field gradient in the bias field direction by minimising the resonance's linewidth.

reduction of the probe size to 0.5 mm diameter, led to much improved resonances both at the 2nd RF evaporation and later at the dipole trap load (200 k atoms) phase. Both are shown in Figure 6.35, with the raw data extracted from the offline phase sensitive detection method plotted. Polarimeter signal averaging was also implemented at this stage, to help with consistency in resonance shape. For the data presented in Figure 6.35, three polarimeter signals are averaged per point. A full characterisation of the magnetometers performance is given in Chapter 7, where magnetometry in the BEC is also presented.

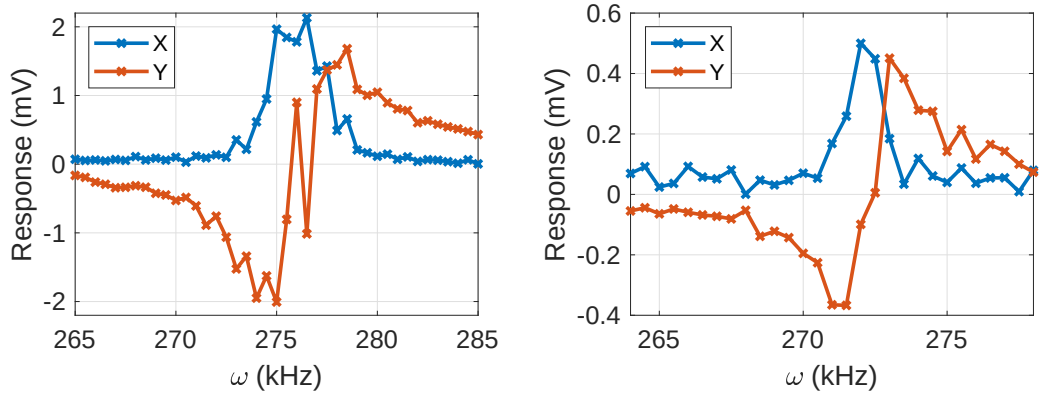

Figure 6.35: Magnetic resonances at the 2nd RF, left, and dipole trap loading phase, right. As expected, with the decrease in number of atoms the resonance amplitude drops. Data is the raw output from the offline phase sensitive detection.

Chapter 7

Ultracold AM - Results

This chapter will detail results from the ultracold ^{87}Rb radiofrequency magnetometer experiment. First, an overview of the BEC production and the necessary experimental observations for confirmation of condensation is presented, before discussion of the sensor's performance. Finally, initial work on conductivity measurements is described with applications in electromagnetic induction imaging (EMI).

7.1 Bose-Einstein Condensation

Consistent production of a BEC requires a precise sequence, where a plethora of hardware is switched on and off or ramped. This controls the frequency and intensity of different lasers, shutters, magnetic fields and a camera. For this experiment, there are five different laser beams; cooling, repumping, pumping (imaging), probing, and dipole trapping. In terms of magnetic fields, there are: compensation, radio frequency for evaporation, radio frequency to probe the magnetic resonance, and quadrupole coils. The switching during the sequence of some of these lasers and magnetic field controls are shown in Figure 7.1. Atoms are first loaded into a MOT from background vapour in the LVIS chamber, before being transported into the science chamber to be trapped by a secondary MOT. The duration of this can be tuned to the required number of atoms at the beginning of the sequence, but a typical duration of 20 s is used. Next, the atoms are compressed in a C-MOT regime, before polarisation gradient cooling (PGC) and optical pumping. All these have been described in further detail previously. Once optically pumped, the atoms can be efficiently transferred into the magnetic trap

(MT). All lasers are shuttered off, apart from the dipole trap. Switching the dipole trap on here was found to be optimal, as the depth of the trap is significantly lower than the average temperature of the atoms at this point in the sequence so it does not interfere with the magnetic trap loading or evaporation, but does give the dipole trap's optics and AOM time to reach a steady temperature. The quadrupole current is ramped up to 63 A (176 G/cm) in 2.5 s. Once at a maximum, the RF evaporation can begin. The RF sweeps from 13 MHz to 3.5 MHz in 5.3 s. The second stage of RF evaporation sees the frequency swept to a final setpoint of 0.8 MHz in 2.25 s, with the gradient also reduced to 29 G/cm. Some durations are different to the optimised ones in Chapter 6 as phases lasting hundreds of milliseconds are required for hardware switching, and the total time is reported here. This leads to the dipole trap evaporation, where both the gradient and dipole trap power are reduced to 6.6 G/cm and 510 mW respectively in 3 s. Finally, Bose-Einstein condensation is observed with the dipole trap power lowered to 300 mW and the gradient increased to 16.5 G/cm in 4.7 s. The atoms are held in this potential for 100 ms before either absorption imaging for diagnostics is performed or magnetometry.

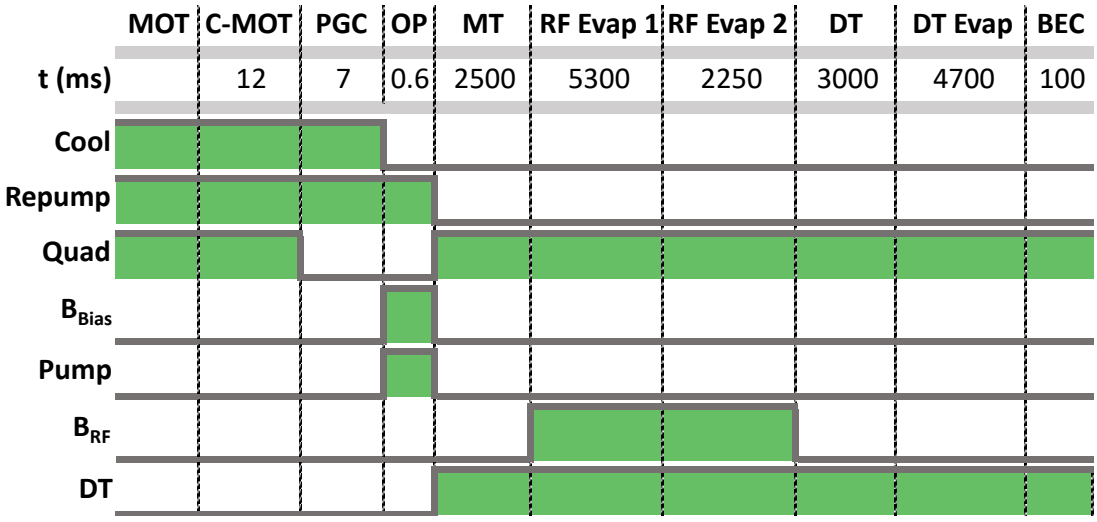

Figure 7.1: The sequence used to achieve Bose-Einstein condensation. Different phases in the sequence are labelled, with the duration of each phase reported. Cooling, repumping, pumping and dipole trap light as well as quadrupole, bias and rf fields are shown when 'on' in green. Absorption imaging and magnetometry are omitted for clarity, with the sequence showing BEC production alone.

To further illustrate the sequence, four images of the atoms in different phases

are shown in Figure 7.2. These correspond to the magnetic trap, first RF evaporation, second RF evaporation, and loading of the dipole trap dimple. The magnetic trap is where the evaporation begins, with a starting atom number of 3.4×10^8 and PSD of 1.5×10^{-7}. After the first RF evaporation, the atom number decreases to 1.1×10^7 with the PSD increasing to 3.5×10^{-6}. Next, the dipole trap beams are clearly seen in the atom image of the second RF evaporation. Here, there are 1.23×10^6 atoms with a PSD of 8×10^{-4}. Finally, the dipole trap dimple is fully loaded with 1.44×10^5 atoms and a PSD of 5.9×10^{-2}.

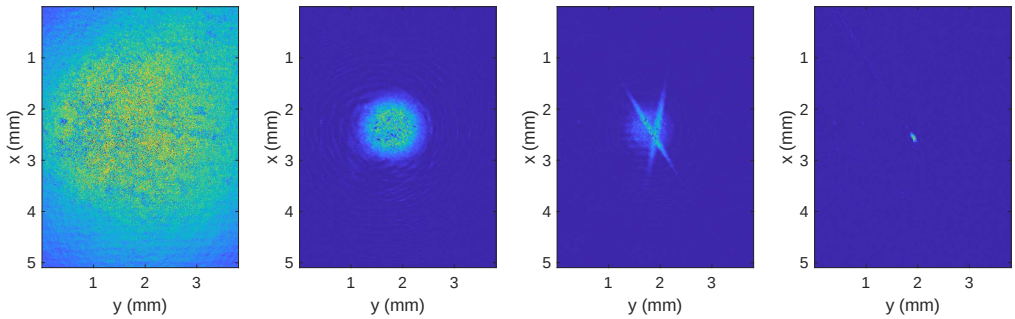

Figure 7.2: Overview of the evaporation process before condensation. Left to right: Absorption images of atoms in the magnetic trap, first RF evaporation, second RF evaporation, and dipole trap loading phases of the sequence. Atom number and PSD are described in the text. The field of view of the imaging is 3.8 mm x 5.1 mm, imaged on a 1040x1392 pixel sensor. Further details of the imaging setup is given in Appendix A.

There are two important parameters in evaporation: time and number of atoms. Both are interchangeable due to the lossy nature of the trap. 'Bad' collisions cause atom loss, limiting the time efficient evaporation can be performed for. However, atoms must be removed to decrease the temperature of the remaining cloud. The overall sequence is evaluated, to consider the efficiency with which the atoms are removed from the trap. Firstly, the evaporation sequence against time can be seen in Figure 7.3. Evaporation happens on an exponential scale [110], and so the exponential increase of PSD and decrease of temperature is expected theoretically. Time measurement begins from after the atoms are loaded into the MOT. The first measurement of PSD and temperature is after the atoms are fully loaded into the magnetic trap (t = 2.5 s). Subsequent measurements align with the distinct phases shown in Figure 7.1.

Next, the measured PSD is plotted against the atom number, shown in Figure

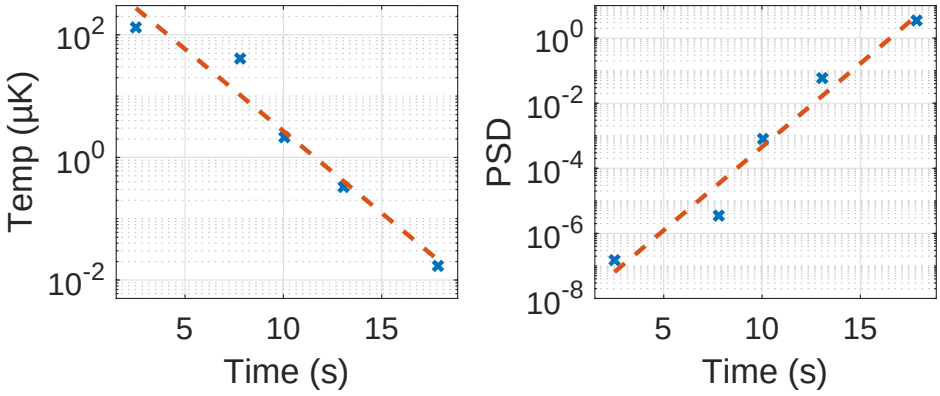

Figure 7.3: Temperature and PSD against evaporation time. Data (blue crosses) with an exponential fit (red dashed line) illustrates the decreasing temperature and increasing PSD. Each data point corresponds to a different phase in the evaporation, discussed in Figure 7.1.

7.4. The overall efficiency of the evaporation can be estimated from the fit of the data, giving

$$\bar{\gamma}_{ev} = -\frac{ln(PSD/PSD_0)}{ln(N/N_0)} = 1.98 \tag{7.1}$$

[142], where N is the atom number and N_0, PSD_0 are the initial atom number and phase space density before evaporation begins. Exponential increase in PSD is achieved, leading to observation of a BEC, with a cross section of a typical absorption image at time-of-flight (TOF) of 10 ms shown in the right panel of Figure 7.4. A bimodal distribution is observed, with a sharp peak corresponding to atoms in the BEC at the centre of the cloud. Typically, temperatures below 25 nK are achieved with 4×10^4 atoms.

Further evidence of the BEC is in the asymmetric expansion of the cloud. This is well documented in previous work [162] [163] [164], and is a good diagnostic tool to confirm the BEC presence. It is explained by the asymmetry of the confining potential, with the atoms held tighter in the radial directions. Repulsion between neighbouring atoms sees faster expansion in the radial directions compared to the axial, eventually leading to aspect ratio inversion. This is not the case for uncondensed atoms which behave as a classical gas and must expand isotropically by definition. Figure 7.5 plots the aspect ratio of both the condensed and uncondensed clouds against time of flight. Fitting of the two distributions is explained further in Appendix A.3. The

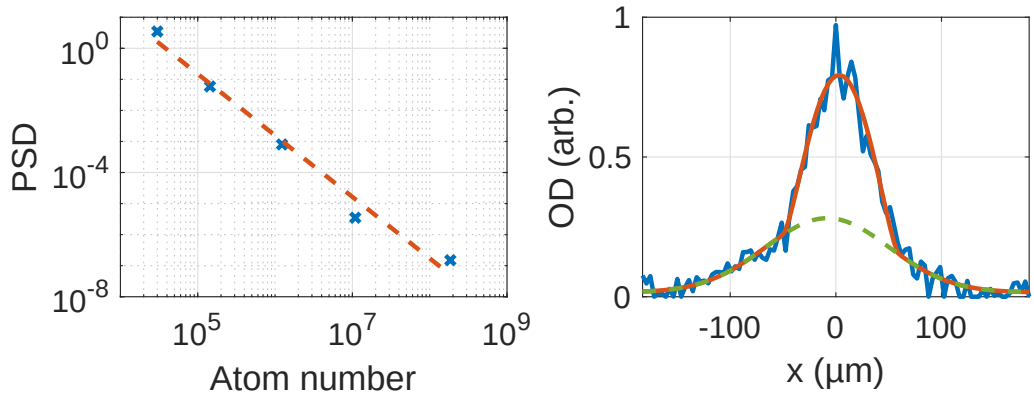

Figure 7.4: Production of a BEC via evaporative cooling. Left, the PSD increase with reduction of atom number. Data (blue crosses) are fitted with an exponential fit (red dashed line), allowing extraction of the evaporation efficiency. Right, the bimodal distribution observed when atoms are in the BEC. An absorption image of the atoms is taken and the optical density is normalised to the maximum in the image.

cloud expands from the asymmetric potential, with the uncondensed atoms saturating at unity aspect ratio, whereas the condensed atoms invert the aspect ratio.

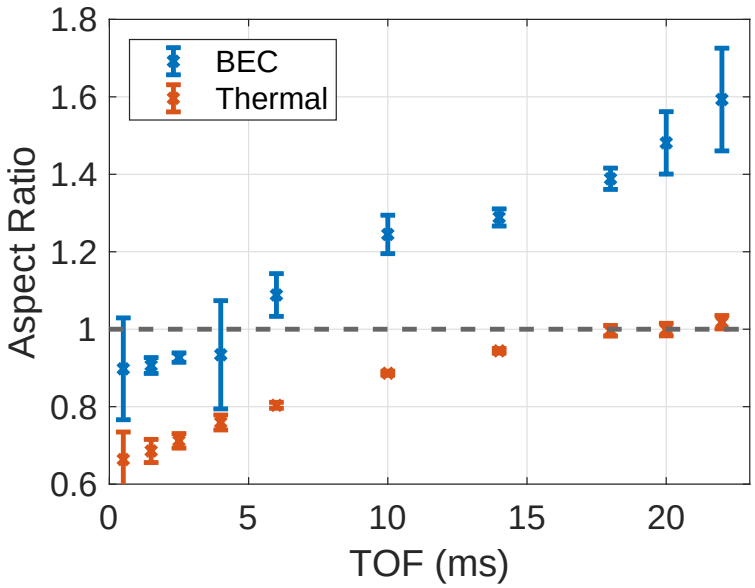

Figure 7.5: Aspect ratio of the separated BEC and thermal sections of the atomic cloud plotted against time of flight (TOF). The non-condensed atoms saturate at unity aspect ratio, whilst the BEC undergoes aspect ratio inversion due to its asymmetric expansion from a cigar shaped trap.

7.2 Sensor Characterisation

The sensor is firstly characterised with the atoms loaded into the magnetic trap. This is the phase in which the best sensitivity is measured. For the following measurements, the probe is detuned by +330 MHz from the ^{87}Rb $5^2S_{1/2}, F = 2 \rightarrow 5^2P_{3/2}, F' = 3$ cooling transition with an intensity of 568 μW cm^{-2} (optimised for best sensitivity in Figure 6.24). Figure 7.6 shows a typical response of the magnetometer working at its most sensitive, with 3.4×10^8 atoms after loading of the magnetic trap. Part (a) illustrates an amplitude spectrum with the bias field (B_{Bias}) set to 15.2 μT (106.5 kHz) and an applied calibration field (B_1) of magnitude 63 nT. The total noise (same conditions, calibration field off) defines the SNR as 2632, leading to an AC sensitivity of $\delta B_1 = \frac{B_1}{SNR} = 24\,\text{pT}/\sqrt{\text{Hz}}$.

Figure 7.6 (b) shows the phase sensitive detection response, with the frequency swept resulting in an in-phase Lorentzian and out of phase dispersive referenced to the internal oscillator. The width of the resonance, Γ, is calculated from the fit as 1.27 kHz, confirming the AC sensitivity agrees well with another figure of merit, $\delta B_2 = \frac{\hbar}{g_F \mu_b} \frac{\Gamma}{SNR} = 22\,\text{pT}/\sqrt{\text{Hz}}$. The inset to Figure 7.6 (b) shows 0.1 ms of the unprocessed polarimeter signal when B_1 is set to the resonant frequency. Clear oscillation at 106.5 kHz is seen, as expected at this bias field magnitude.

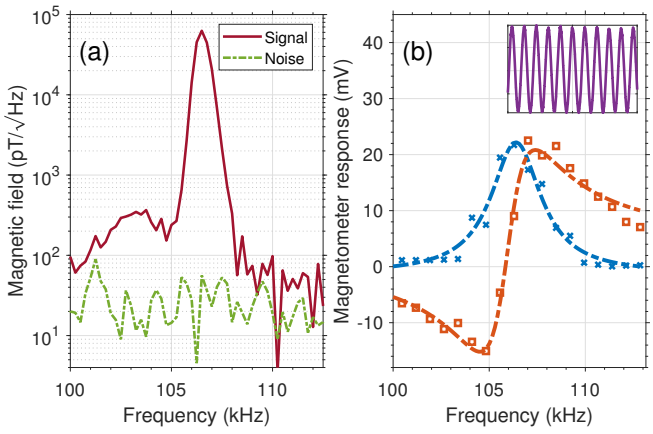

Figure 7.6: Magnetometry performed at the magnetic trap phase of the sequence where the magnetometer is most sensitive. Left, amplitude spectrum extracted from an FFT of the polarimeter signal, defining the SNR. Right, the magnetic resonance extracted from phase sensitive detection, with the inset showing 0.1 ms of polarimeter signal at the resonance to illustrate the clear oscillations. Further detail in the text.

Next, the sensitivity of the sensor is characterised in the BEC, shown in Figure 7.7. The probe parameters are the same as previously, but now the calibration field must be 398 nT for a reasonable SNR to be achieved. With an SNR of 4.7 and width of 1.44 kHz the AC sensitivity is 84 $\mathrm{nT}/\sqrt{\mathrm{Hz}}$ and the DC sensitivity is 14 $\mathrm{nT}/\sqrt{\mathrm{Hz}}$. The divergence between the AC and DC sensitivity is expected in the RF power broadened regime, and indeed similar results can be extracted from data presented in the cold atom magnetometer (such as Figure 5.4).

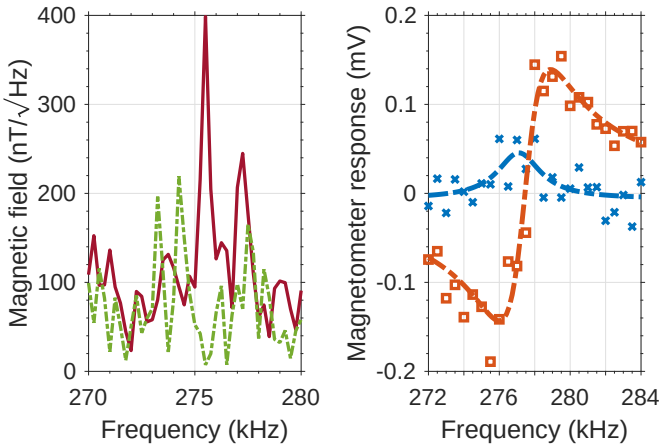

Figure 7.7: Magnetometry performed at the BEC with the smallest achievable probe volume. As before, left is an amplitude spectrum and right is the magnetic resonance. The magnetometer must be RF power broadened due to the small SNR measured, causing the out-of-phase (Y) response to grow above the in-phase (X).

With magnetometry achieved in the BEC, a comparison of the sensitivity scaling with atom number and probe volume is discussed next. The AC sensitivity is calculated at different points in the evaporation, and the atom number and density recorded (allowing for conversion to volume), illustrated in Figure 7.8. A reduction in the measured sensitivity as the probe volume decreases is seen, as expected. No obvious change in the scaling is seen between the thermal and condensed atoms. A similar conclusion can be drawn for the atom number scaling. However, both relationships show the impressive tunability of the magnetometer. The probe volume can be controlled and changed by up to seven orders of magnitude, from $1.4 \times 10^{-7}\,\mathrm{m}^3$ to $1.6 \times 10^{-14}\,\mathrm{m}^3$. No change to the sensor itself is necessary to control the probe volume, and all volumes in between the data points plotted are accessible by changing

the loading time of the MOT. This highlights the adaptability of the ultracold atom magnetometer. Depending on application, the probe volume can be tailored, with the trade-off in reduced sensitivity considered. $14\,\mathrm{nT}/\sqrt{\mathrm{Hz}}$ sensitivity at the smallest probe volume can be exploited for high conductivity EMI, although the distance between object and sensor must be considered. Higher sensitivity can be accessed at reduced spatial resolution. This level of control is infeasible in vapour cell magnetometers, where atomic number or probing volume is not tunable over such a broad range.

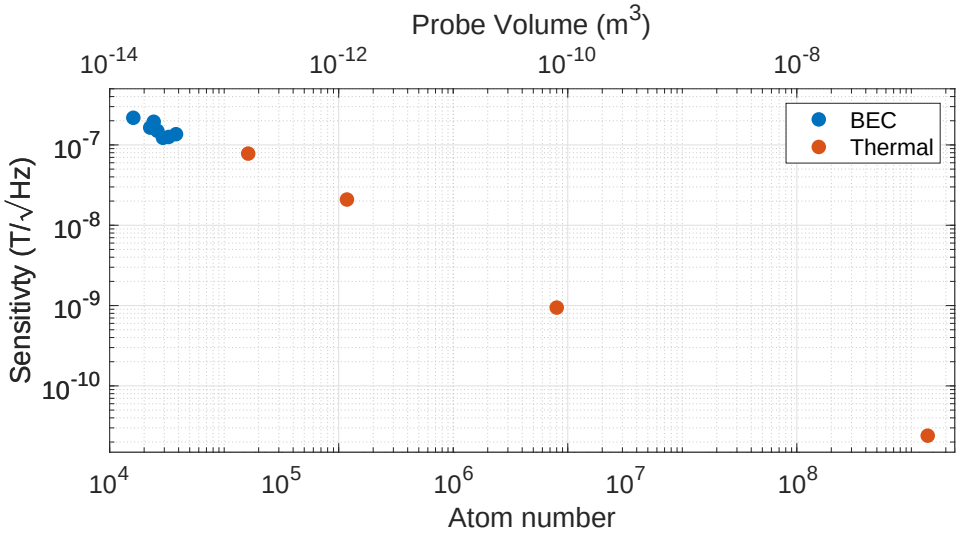

Figure 7.8: Scaling of the sensitivity with atom number and probe volume. Both parameters are varied, and the AC sensitivity for the thermal cloud and BEC is recorded. This single sensor can vary its sensing volume by seven orders of magnitude depending on the application requirements.

Next, the results are contextualised in the background of previous achieved magnetometers in literature in Figure 7.9. Here, the same set of magnetometers shown in Chapter 1 are now plotted with the results reported in this thesis. The ultracold radio frequency magnetometer achieves similar probe volume to other BEC magnetometers, apart from 'BEC2' where the atoms are loaded into a lattice and the authors define a probing volume of each lattice site. The magnetometer reported in this reference is a gradiometer, and therefore not applicable for the suggested motivation of this project. When considering absolute sensitivity, the magnetometer presented here achieves $\mathrm{nT}/\sqrt{\mathrm{Hz}}$ compared with the $\mathrm{pT}/\sqrt{\mathrm{Hz}}$ in previous implementations,

around three orders of magnitude lower. However, these either measure simulated fields induced by a light beam (BEC1), are gradiometers (BEC2), exploit complicated spin-echo measurement schemes (BEC3) or extract the sensitivity from spectrograms (BEC4). None record a magnetic resonance, required for EMI applications. Furthermore, significant improvements in sensitivity are envisaged for the ultracold radio frequency magnetometer, starting from increasing of the probe detuning. Many of the BEC magnetometers either exploit D1 detuned probes or wavelengths near 790 nm. The current near resonant detuning, due to limitations of available equipment, is likely to be non-ideal.

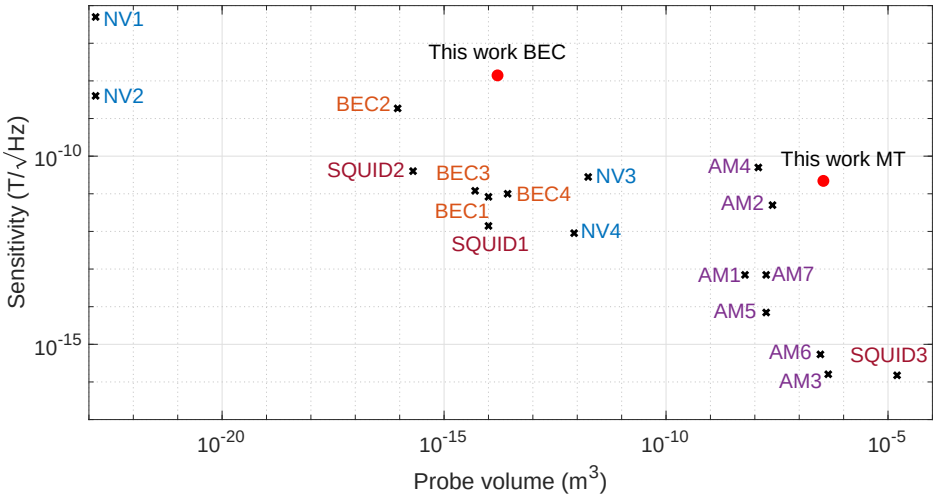

Figure 7.9: Contextualising the results presented in this thesis. As before, **NV(1-4)** [67, 68, 69, 70], **AM(1-7)** [28, 71, 42, 72, 73, 40, 74] **SQUID(1-3)** [75, 76, 35] **BEC(1-4)** [53, 77, 78, 79]. Probing volumes between the two points shown are accessible with the magnetometer built in this project.

7.3 Conductivity measurements

To further motivate this work, a proof of concept EMI measurement is presented in this section. EMI relies on a sample's response to an oscillating field. These oscillating fields produce eddy currents in the sample, causing a secondary field. A magnetometer measures the total field, which is a combination of the two fields described. We can firstly describe the skin depth, a property which defines the depth at which the eddy

current density falls to 1/e, as

$$\delta = \sqrt{\frac{2}{\sigma\omega\mu}}\left[\sqrt{1+\left(\frac{\omega\varepsilon}{\sigma}\right)^2}+\frac{\omega\varepsilon}{\sigma}\right]^{\frac{1}{2}}, \tag{7.2}$$

where σ is the conductivity, ε is the permittivity and μ is the permeability of the object [165, 158, 27]. Next, we start by assuming the object to be a disc, placed coaxially and midway between the oscillating field producing coil and the sensor. In addition, we assume that both the diameter of the coil is small compared with the separation and that the penetration depth is much larger than the object thickness. We can then write the relative change in magnetic field at the sensor, $\Delta B/B$, as

$$\frac{\Delta B}{B} = C\omega\mu_0[\omega\varepsilon_0(\varepsilon_r-1)-i\sigma]+D(\mu_r-1). \tag{7.3}$$

Here, C and D are parameters which depend on the geometry. Equation 7.3 illustrates that the EMI response from a target object arises from the sample's properties, and any phase lag originates from the sample conductivity, due to the imaginary term. As a proof of concept, a simple EMI setup is shown in Figure 7.10. A small coil generates an oscillating field. This produces eddy current in a 7.5 cm diameter copper disc which generate a secondary field, sensed by the atoms. Rather than full images, a single magnetic resonance is recorded with and without a sample.

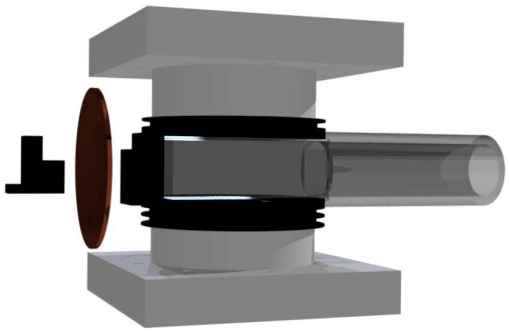

Figure 7.10: Basic setup for conductivity measurements with the ultracold atom magnetometer. A coil (shown in black, left) applies a radio frequency field to the sample (copper disc, middle). A secondary field produced by eddy currents flowing in the sample changes the total field felt at the atoms, altering the magnetic resonance.

Initial measurements with a conductive target are shown in Figure 7.11, with the magnetometer at its most sensitive in the magnetic trap. Both the Y (left) and phase output (right) of the magnetic resonance are plotted. A clear reduction in the Y amplitude is seen. Furthermore, a phase change of the resonance confirms conductivity EMI is attainable with the cold atom magnetometer. However, this amplitude reduction is too large for the magnetometer in later phases of the sequence. This is due to the SNR at the smallest probe volumes, and so a smaller target was used for subsequent measurements.

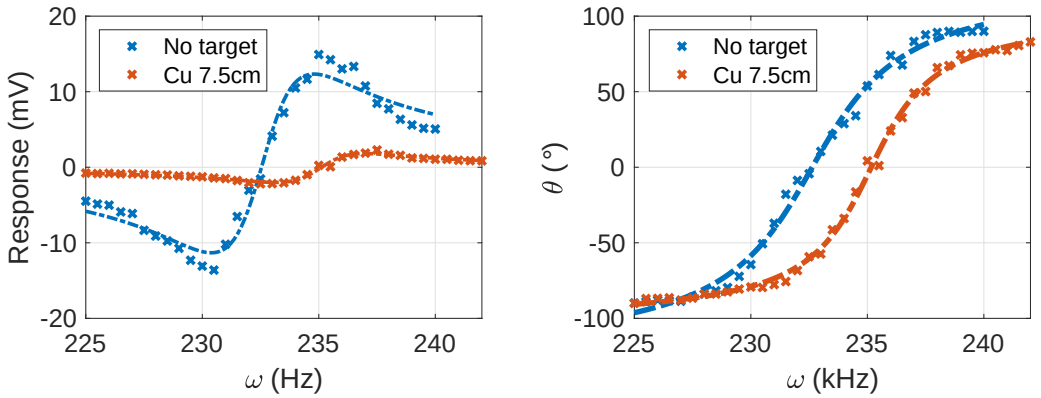

Figure 7.11: MT conductivity measurements. Left, the Y response of the magnetic resonance with and without a 7.5 cm target. Right, the same but for the phase response. The resonance amplitude and phase both change, illustrating this setup's capability to produce EMI images.

Next, this conductivity measurement is pushed further down the evaporation sequence, with a reduced number of atoms and a smaller probe volume. First, the response to a 4 cm target in the 2nd RF evaporation is plotted in Figure 7.12. Here, the bias field points in the opposite direction and at a slightly larger magnitude to the data presented in Figure 7.11, leading to a resonant frequency of 277 kHz. EMI images can employ a detuning from resonance to increase contrast in the output, discussed further in references [23, 25, 2]. As such, we can quote the maximum change in amplitude and phase at a detuning of 1 kHz (taken from a fit of the data) as 1.56 mV and 38.2° respectively. Both would produce clear images if a full EMI procedure is employed.

Finally, the magnetic resonance response to the same conductive target is probed with the atoms loaded into the dipole trap dimple. At this stage of the evaporation,

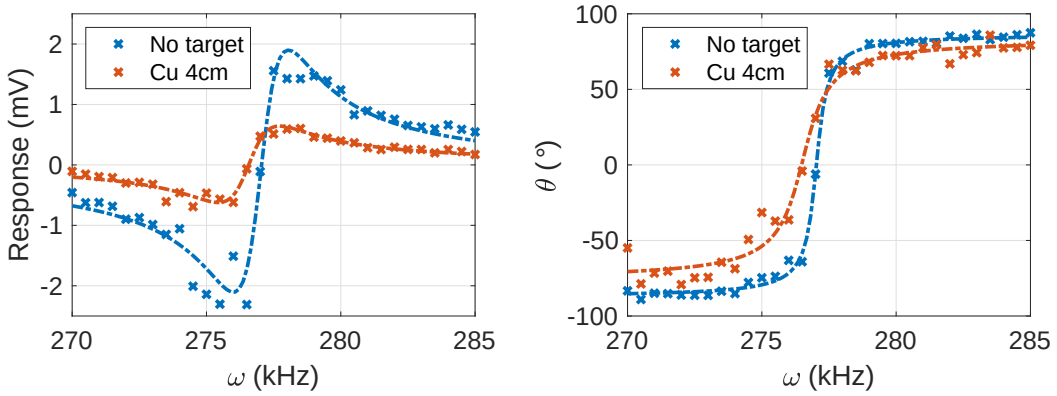

Figure 7.12: Magnetic resonance response to a 4 cm copper disc placed between the RF coil and sensor. Left, the out-of-phase (Y) response. Right, the magnetometer's phase response. Clear reduction in Y amplitude, with a small change in phase suggest EMI images can be produced with this sensor.

only 140k atoms are left in the trap, with a probe volume of just $8.5 \times 10^{-14}\,\mathrm{m}^3$ at a temperature of 300 nK. This is already close to the minimum achieved probe volume of $1.6 \times 10^{-14}\,\mathrm{m}^3$ in the BEC. The data is presented in Figure 7.13. Again, the largest change is seen at a small detuning from resonance. Fitting of the phase data produced coefficients of determination below 0.9, and so the raw data is plotted with the data points joined as a guide to the eye. The change in phase is not quoted due to difficulty in deciding upon an appropriate data point, but the change in amplitude at a detuning of 0.5 kHz is 0.26 mV, taken from a fit of the data.

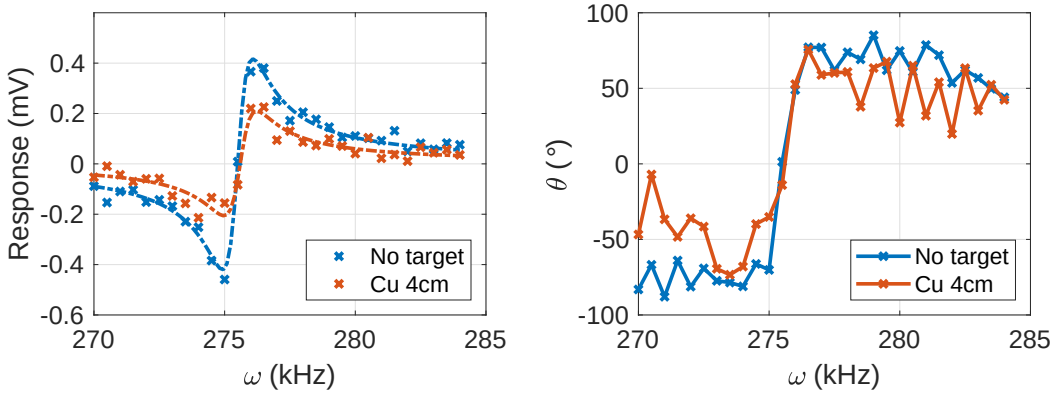

Figure 7.13: As in Figure 7.12 but with the atoms loaded into the dipole trap dimple. At a probe volume of 8.5×10^{-14}, this is the smallest probe volume where a proof of concept EMI measurement was achieved. Reduction in the Y is clear, but the change of phase is less conclusive due to the relatively small SNR.

Chapter 8

Conclusions

This thesis detailed the experimental realisation of a BEC radio-frequency magnetometer, from general concepts to experimental apparatus and results. Firstly, a vacuum system was baked and pumped down to a pressure of 1.02×10^{-10} mbar. Next, a two MOT system trapped 200 µK atoms in the science chamber. C-MOT and PGC schemes compressed and cooled the atoms to 20 µK. Here, the first set of results are recorded. A cold atom magnetometer is built by applying a short optical pumping scheme, before spin precession in a bias field is driven by a radio-frequency magnetic field. This sensor is characterised, achieving a sensitivity of $330\,\mathrm{pT}/\sqrt{\mathrm{Hz}}$. A Bose-Einstein condensate is then produced via evaporation in a magnetic and hybrid dipole trap, reaching temperatures as low as 17 nK. The experimental apparatus is described, highlighting necessary aspects for reliable and repeatable BEC production. The ultracold atoms are then used as a magnetic field sensor, with radio-frequency magnetometry demonstrated, which is characterised and contextualised. A DC sensitivity of $14\,\mathrm{nT}/\sqrt{\mathrm{Hz}}$ and AC of $84\,\mathrm{nT}/\sqrt{\mathrm{Hz}}$ at a probe volume of just $1.6 \times 10^{-14}\,\mathrm{m}^3$ opens the door for applications in high spatial resolution electromagnetic induction imaging, bringing previously achieved EMI in vapour cell magnetometers into the micrometer regime. Proof of concept measurements are made showing conductive targets affecting the acquired magnetic resonance, which can be extended to produce EMI images of high conductivity targets at 4.5 cm stand-off relatively simply with current technology. Applications in conductivity images with micrometer resolution are envisaged by bringing the sensor closer to the target.

All magnetometry performed in this work is in an unshielded environment. The work of this thesis has led to a publication which summarises the results of the cold atom magnetometer [1], where the data presented in Chapter 5 is reported. Work to publish the results in Chapter 7 has now begun.

8.1 Outlook

The long term outlook for this work consists of further improvements to the magnetometer. An immediate upgrade of the probe beam will be made, using a separate laser. This will allow an increase in probe detuning, which should lead to an improvement in sensitivity. Wavelengths of interest include 790 nm, inline with literature suggesting this is the sweet spot for minimal disturbance of coherent precession of the atoms [79], leading to the best sensitivity. Furthermore, efforts to reduce the noise floor by considering different photodiodes and data acquisition solutions could yield further improvements in sensitivity. For the ultracold atom section of the experiment, there will be continued efforts to optimise the sequence and improve the final BEC atom number. A full machine learning optimisation, such as the one suggested in [161], could be implemented.

8.2 Further Work

Apart from the ultracold atom magnetometry, which is the main focus of this thesis, advancements in vapour cell EMI have also been achieved. A portable vapour cell magnetometer was built, characterised and used to show the first implementation of EMI where the sensor is moved and the target is held fixed. Many applications of EMI require the movement of the sensor over the target area. However, all previous AM EMI systems have seen the target scanned with the magnetometer stationary. This is due to the unshielded nature of the radio-frequency magnetometers used for this application. The best sensitivity is achieved by zeroing of background fields. Moving the magnetometer therefore introduces many technical difficulties.

Briefly, the portable magnetometer drives progress in the commercialisation and miniaturisation of many components which are standard in laboratory implementation of radio-frequency magnetometers. Firstly, the whole sensor head is re-

duced to 110x110x145 mm, weighing 1.49 kg. Two Vixar I0-0795S-0000-BC06 VCSEL lasers provide pumping and probing light. The pump is tuned to the ^{87}Rb $5^2S_{1/2}, F = 1 \rightarrow 5^2P_{1/2}, F' = 2$ D1 transition, with the probe firstly tuned to ^{87}Rb $5^2S_{1/2}, F = 1 \rightarrow 5^2P_{1/2}, F' = 1$ and then optimised against the magnetometer resonance. A bias field is produced by Helmholtz coils (35 turns 0.2 mm diameter), with similar coils in the perpendicular directions used to zero the transverse fields. A 3-axis fluxgate (Bartington MAG619) measures the magnetic field near the cell, and is used to stabilise the fields in all directions. SIM960 PIDs are used to lock the measure from the fluxgate, by controlling the current in each of the coils. A radio-frequency coil drives coherent spin precession which is imprinted onto the probe polarisation due to Faraday rotation. A miniaturised polarimeter, consisting of a half wave plate, polarising beam splitter, mirror, photodiodes, PCB and SMA output provides electronic readout of the probe polarisation oscillation. The total volume for the polarimeter is 29.7 cm^3, a vast improvement on typical laboratory implementations. The technique to stabilise the field showed a reduction in resonant frequency variation across a 200x200 mm plane from 25.6 kHz to 3.2 kHz as well as an improvement in the resonance amplitude by a factor of two. A 17 nT calibration field leads to an SNR of 915, defining the AC sensitivity as 19 pT/$\sqrt{\text{Hz}}$. A linewidth of 460 Hz leads to a DC sensitivity of 22 pT/$\sqrt{\text{Hz}}$. Although impressive, two further techniques to extract high quality images from the data are required. Firstly, the resonant frequency is tracked by fitting the in-phase (X) resonance. Secondly, data for (X,Y,R,ϕ) is extracted with some detuning from the resonant frequency defined separately for each pixel. This smooths the background so clear images are produced without the need for background subtraction. This work is published in [2].

To conclude, this thesis has driven progress in the development of new sensors. In the past, technological advancements such as these have proven extremely valuable to society. Continuing research into these sensors could see them integrated into everyday lives, with a plethora of applications.

Appendix A

Imaging system

A.1 Fluorescence

Fluorescence imaging is used as a tool for diagnostics and optimisation. Although any measurements in this system are not converted to atom number or temperature, it allows for fast non-invasive read out of the atom trap condition. The fluorescence imaging system uses an Allied Vision Mako U130B camera with a C-MOUNT mounted objective. It has a CMOS sensor, 1280 (H) × 1024 (V) resolution and close to 35% quantum efficiency at 780 nm. The distance from the objective to the MOT is 20 cm, although the position of the camera is moved frequently depending on need. The image is in the yz plane, perpendicular to the absorption imaging plane.

A LabVIEW program uses the USB 3.0 interface on the camera to output a Mono8 image, which is false coloured for the user. Region of interest (ROI) selection is available, where a mean of the pixel measurements within the ROI is calculated and displayed on a time graph. Although the numbers are arbitrary, estimation of the MOT size, atom number and density can be made. This real-time response is crucial for the fast and efficient optimisation of the MOT and continued monitoring of experimental conditions.

A.2 Absorption

Absorption imaging of the atoms is used to extract atom number, density and temperature measurements. The optical path of the imaging beam is illustrated in Figure 4.5. Cooling light is extracted and passed through an AOM, allowing for dedicated fast

switching of the imaging beam. Next, the beam is injected into a fibre, which is passed across the optical table before collimation at the fibre output. Circular polarisation is set after passing through a quarter waveplate. The frequency of the beam is resonant with the $5^2S_{1/2}, F = 2 \rightarrow 5^2P_{3/2}, F' = 3$ transition. A single lens (f = 200 mm) focuses the atom image onto a pco.pixelfly USB camera. A schematic of the image formation and beam propagation is shown in Figure A.1.

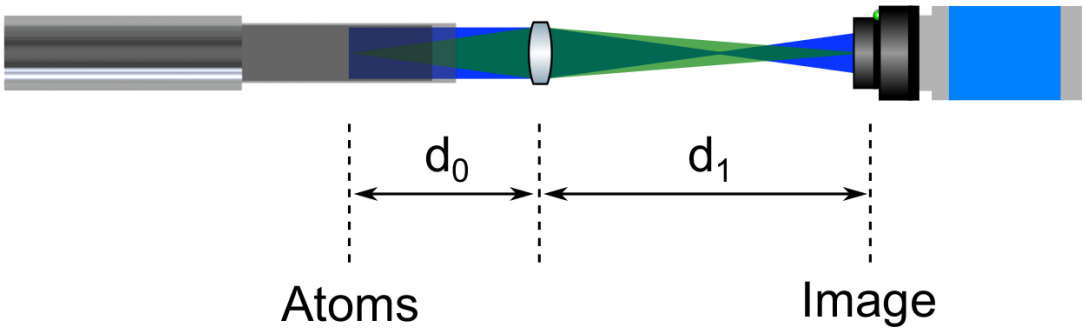

Figure A.1: Imaging of the atoms with a single lens. A collimated imaging beam (blue) passes through the cell and atoms. The image formed (green) is in focus when the lens equation is fulfilled. Changing the distance between the atoms and the lens (d_0) allows tuning of the magnification. The camera position is set at a distance from the lens (d_1) which produces an in-focus image. Mirrors and other optical components are omitted for clarity.

For imaging of the atoms, resolution on the order of 10 µm is required, corresponding to a value smaller than the typical size of a BEC. Furthermore, a relatively large field of view is also essential to be able to image the atoms both at the MOT and through the evaporation. Finally, with the imaging beam alignment seeing the atoms' free fall change the distance of the object to be imaged to the lens, a reasonable depth of field is also required. To confirm many of these parameters, a USAF 1951 target is used. This is placed above and below the cell (d_0), and the focus position is measured (d_1). Element [1,6], with a width of 140 µm, is used to determine the experimental magnification (M_{Exp}), by mapping the measured pixel width and comparing with the sensor's actual pixel width of 6.45 µm. The expected theoretical magnification is also quoted (M_{Theory}). A summary of the result is shown in Table A.1.

	Top	Bottom
f (mm)	200	200
d_0 (mm)	329	294
d_1 (mm)	511	627
M_{Theory}	-1.56	-2.13
Pixel width (μm)	4.22	3.04
M_{Exp}	-1.53	-2.12

Table A.1: Focal length, distance and magnification values for two positions of the target, above and below the cell. A 200 mm lens is placed after the imaging beam passes through a USAF 1951 target. The distance between the target and lens is varied (d_0), and the distance of the focus is found by moving the pixelfly camera (d_1). A theortical magnification at these distances is calculated (M_{Theory}) and is compared to the experimentally measured magnification (M_{Exp}) calculated from the ratio of the pixel width at the image and the actual pixel width.

To visualise the change in magnification and ideal camera position as the object moves through the cell, the data above is plotted with theoretical calculations, shown in Figure A.2. The data is in good agreement with the theoretical prediction, so the camera is placed at 552 mm away from the lens, the ideal position to focus atoms after 10 ms of free fall (0.49 mm below the centre of the cell, 10 ms chosen as this is the time of flight the BEC will be imaged at). The calculated magnification is 1.76, giving an image pixel size of 3.66 μm.

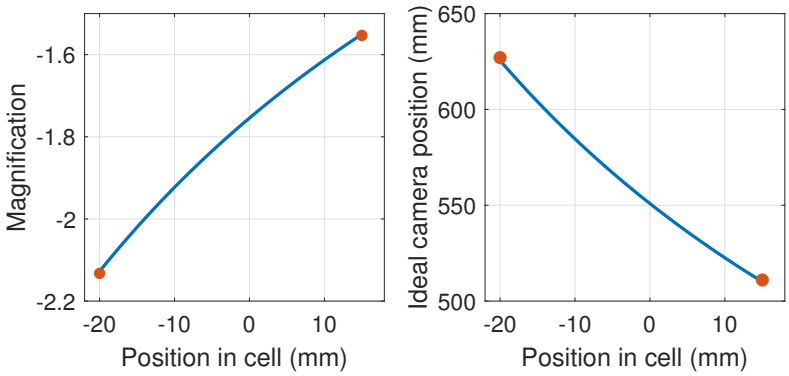

Figure A.2: Red circles show the experimentally measured magnifications and ideal camera positions for an in-focus image. The blue line plots the theoretical predictions by the lens equations. The atoms are imaged at −0.49 mm from the centre of the cell, so the camera is placed at d_1 = 552 mm giving a magnification of 1.76.

A.2.1 Atom Number

The following reasoning closely follows the work presented in [166], which describes a simple setup for production of BECs. The intensity of an imaging beam propagating through a cloud of cold atoms can be described by Beer's law:

$$I = I_0 e^{-O.D} \, . \tag{A.1}$$

I_0 is the initial intensity, I the intensity of the beam after interaction with the atoms and $O.D$ the optical density of the atoms. Rewriting this in terms of the column density of the atoms, $n(x,y)$ and their interaction cross section, σ,

$$I = I_0 e^{-n(x,y)\sigma} \, , \tag{A.2}$$

where σ has the expected Lorentzian dependence on the on resonance scattering cross section, σ_0,

$$\sigma = \frac{\sigma_0}{1 + 4(\frac{\Delta}{\Gamma})^2 + \frac{I_0}{I_{sat}}} \, . \tag{A.3}$$

I_{sat} is the saturation intensity, Γ the linewidth of the transition, and Δ the detuning. The on resonance scattering rate, for circularly polarised light driving a cooling transition, can be calculated from the following:

$$\sigma_0 = \frac{3\lambda^2}{2\pi} \, . \tag{A.4}$$

Clearly, if the optical density of the atoms is known, the column density can be deduced from:

$$n(x,y) = \frac{O.D(x,y)}{\sigma} \, . \tag{A.5}$$

The optical density of the atoms can be calculated by taking 3 images; an image with the atoms (I_{atoms}), an image without the atoms but the imaging beam on (I_{light}), and an image with no atoms and no imaging beam (I_{dark}). I_{dark} describes any signal from dark currents in the camera or light not from the imaging beam, which can be subtracted

from the measurement, so equation A.1 becomes:

$$(I_{atoms} - I_{dark}) = (I_{light} - I_{dark})e^{-O.D_{meas}}, \tag{A.6}$$

leading to:

$$O.D_{meas} = ln\left(\frac{I_{light} - I_{dark}}{I_{atoms} - I_{dark}}\right). \tag{A.7}$$

This measured optical density is not the true optical density of the atoms. We must consider saturation of the camera pixel, due to off resonant light (multi mode of the imaging beam) or imaging beam scattering. We can make some adjustments, by calculating a modified optical density [166], $O.D_{mod}$:

$$O.D_{mod} = ln\frac{1 - e^{-O.D_{sat}}}{e^{-O.D_{meas}} - e^{-O.D_{sat}}} \tag{A.8}$$

A measurement of $O.D_{sat}$ can be made by expanding a very dense cloud for 1ms. With a very dense cloud, the saturation optical density is obvious, with a flat top at the centre where our measurement is limited. A final adjustment can be made to get the true optical density, taking into account the imaging beam intensity:

$$O.D_{actual} = O.D_{mod} + (1 - e^{-O.D_{mod}})\frac{I_0}{I_{sat}}. \tag{A.9}$$

In this experiment, imaging beam intensities (I_0) on the order of $60\,\mu W\,cm^{-2}$ are used. Given the saturation intensity for ^{87}Rb ($I_{sat} = 1.67\,mW\,cm^{-2}$ [81]), the final term on the RHS of Equation A.9 is neglected. Finally, the atom number can be calculated. We can define the atom number N to be

$$N = \int_{-\infty}^{+\infty}\int_{-\infty}^{+\infty} n(x,y)dxdy. \tag{A.10}$$

Practically, $O.D_{actual}$ is an array with points corresponding to each pixel. The effective area a pixel covers, A_{pixel}, is calibrated by measuring the magnification of

the imaging system, described earlier. The integral becomes a summation:

$$N = \frac{A_{pixel}}{\sigma} \sum_{all\,pixels} O.D_{actual}. \tag{A.11}$$

Further adjustments include if any pixel is different by more than 4 O.D of its 8 neighbouring pixels, then an average of the 8 is taken and used for the value of the problematic pixel. A robust and reliable imaging system is realised.

A.2.2 Temperature

Once an optical density array is extracted, the data is fitted with a 2D Gaussian function. This gives a σ_x and σ_y, as well as their central points, in pixel number. Conversion to lengths is done with the previously described calibration, giving the radial size of the cloud in the x and y direction. The time dependent size of the cloud can be related to the temperature with the following equation:

$$\sigma(t)^2 = \frac{k_b T}{m} t^2 + \sigma_0^2 \tag{A.12}$$

Time of flight (TOF) measurements allow plotting of $\sigma(t)^2$ against TOF^2, and extraction of the gradient, which is the coefficient of t. Temperatures in the x and y direction are calculated, and their mean taken. This gives an overall temperature which characterises the atoms. An example of how the Gaussian fit increases with TOF can be seen in Figure A.3. Adding more TOFs allows plotting of Figure A.4, giving a temperature for the example used of 2 µK.

A.2.3 Optical pumping out of resonance

The imaging beam interrogates atoms on the $5^2S_{1/2}, F = 2 \rightarrow 5^2P_{3/2}, F' = 3$ cooling transition. Atoms may be in a state not visible to a laser tuned to this transition, so called 'dark states'. Going down the cooling sequence, from MOT to polarisation gradient cooling (PGC) to magnetic trapping (MT), an increase in measured number of atoms is seen. This was attributed to lack of interaction with the imaging beam, due to optical pumping during the MOT into a dark state ($|F_1\rangle$). Insufficient repumping laser power is likely the cause of this. For confirmation, a dedicated 0.2 ms repumping

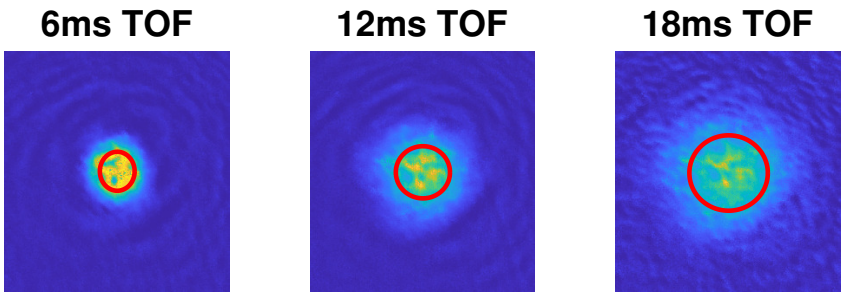

Figure A.3: A temperature measurement of 2 µK atoms. As the time of flight (TOF) increases, the calculated σs from a 2D Gaussian fit increase. These are illustrated by plotting a circle (red line), with radii corresponding to the fit σs.

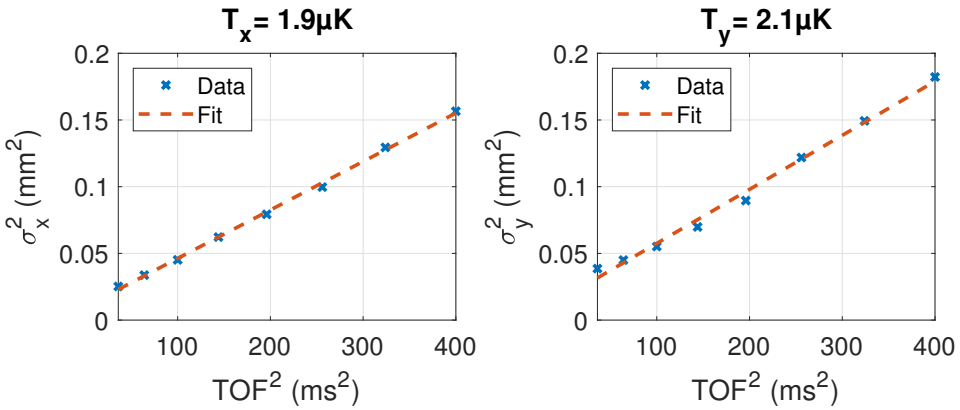

Figure A.4: Temperature measurement of the same atoms as in Figure A.3, with more TOFs inserted, giving an overall average temperature of 2 µK.

phase is implemented prior to imaging, during which the atoms are only exposed to the repumping beam. Figure A.5 illustrates this test. In (a), no repumping phase is implemented, and the number of atoms as the sequence progresses increases. In (b), the expected decrease in atom number as the sequence progresses is regained, with the true number of atoms in the MOT measured. At the magnetic trap, the number of measured atoms is within experimental error for both conditions. As such, the repumping phase is implemented only when requiring a measurement of the MOT or PGC atom number.

A.3 BEC fitting

In order to identify the phase transition from a thermal cloud to a BEC, both the temperature and density of the atoms must be accurately measured. This gives a useful

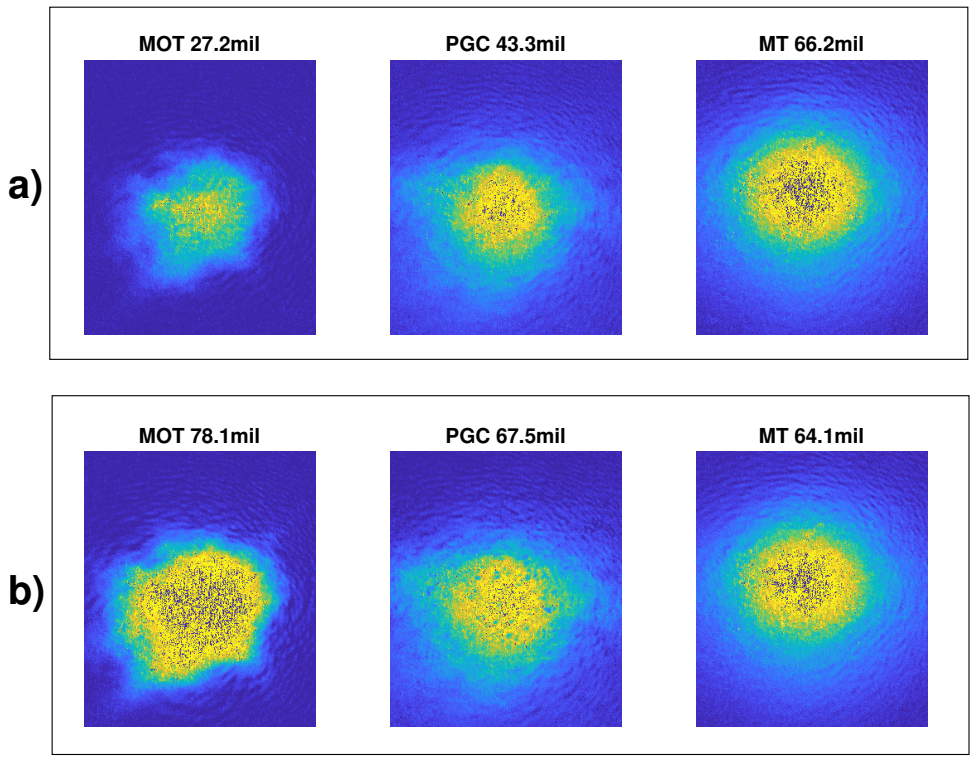

Figure A.5: Atom number measurements at different points in the cooling sequence. In a) with no repumping and b) with repumping, confirming atoms are optically pumped out of resonance in the MOT and PGC. Consistent atom number measurements in the magnetic trap (MT) are seen for both (a) and (b).

figure, the phase space density, which implies a phase transition as it reaches unity. At the boundary of the transition, a bi-modality in the distribution of the atoms is seen. This is the most informative sign which can be used for optimisation of the evaporation sequence to improve the number of atoms in the BEC. Firstly, in the thermal regime above condensation, the cloud can be well described by a multivariate Gaussian function

$$OD_{Gauss}(x,y) = OD_{Gmax} \exp\left[-\frac{1}{2}\left(\frac{x-x_0}{\sigma_{Gx}}\right)^2 - \frac{1}{2}\left(\frac{y-y_0}{\sigma_{Gy}}\right)^2\right]. \tag{A.13}$$

Once condensed, the atomic distribution in the BEC can be estimated using the Thomas-Fermi approximation [167] [168], leading to the inverted parabola Thomas-

Fermi distribution, defined as

$$OD_{TF}(x,y) = \Re\left\{ OD_{TFmax} \exp\left[\left(1 - \left(\frac{x-x_0}{\sigma_{TFx}} \right)^2 - \left(\frac{y-y_0}{\sigma_{TFy}} \right)^2 \right)^{\frac{3}{2}} \right] \right\}. \quad \text{(A.14)}$$

The disagreement between this and Equation 3.38 is due to integration along the z direction, as images obtained from absorption imaging flatten the distribution into a single plane. With the above equations in hand, we would like to fit a 2D distribution which contains both A.13 and A.14 to an image with a small condensed fraction. This is not straightforward, and so some processing must take place. An overview of the procedure, modified from [169], is

1. Filter noise from image
2. Fit initial 2D Gaussian to identify central cross sections
3. Fit 1D function containing both distributions along separate axes
4. Remove BEC contribution, fit new 2D Gaussian
5. Remove thermal contribution, fit 2D Thomas Fermi

A very useful tool to remove some noise from our data is the Matlab function *conv2*. This computes the convolution between two arrays, such as data and a filter, and resizes the output array to the size of the input array. An outcome of this is that the values of the new filtered image is larger, but this can easily be accounted for by dividing by the magnitude of the convolution of the filter with an array of ones, whose size is that of the image. A comparison of two images, the original and one convoluted with a simple array

$$\begin{bmatrix} 1 & 1 & 1 & 1 & 1 \\ 1 & 2 & 2 & 2 & 1 \\ 1 & 2 & 3 & 2 & 1 \\ 1 & 2 & 2 & 2 & 1 \\ 1 & 1 & 1 & 1 & 1 \end{bmatrix} \quad \text{(A.15)}$$

is shown in Figure A.6. The filter weights the current pixel value the highest, but also considers contribution from neighbouring pixels. This can be extended by instead defining a Gaussian filter.

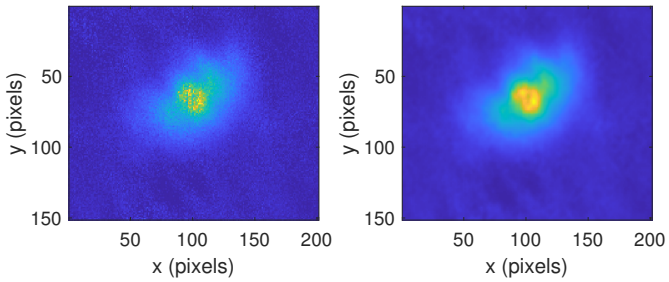

Figure A.6: The raw data (right) compared with the convoluted data (left).

Once filtered, a 2D Gaussian, described by Equation A.13, is fitted to the data by using the *fminunc* optimisation function in Matlab. This minimises the error of a fit (least squares) for a given fit function, and requires initial start points which are calculated automatically from the image. The central positions, defined by x_0 and y_0, and the OD_{Gmax} are all taken from the image maximum. Next, the initial guess for σ_x and σ_y are computed from an estimation of the full-width-at-half-maximum (FWHM). By scanning the array for the closest value to half the maximum before and after the maximum's position, an estimation of the FWHM is extracted, which for a Gaussian function can be easily related to σ using

$$FWHM = 2\sqrt{2ln2}\sigma \approx 2.4\sigma. \tag{A.16}$$

The fitting function can now accurately locate the cloud in the image with no user input. The σ_x, σ_y can be used to plot a circle on the image, which identifies the region the fit believes the cloud to be in. This is useful to ensure the fit is giving a reasonable output, and is shown in Figure A.7. The filtering of the image does not change the computed fit significantly, as fitting of both the filtered and unfiltered image gives output parameters which agree to within 0.3 %. However, filtering does improve reliability of fits, reducing the probability that noisy images are poorly fitted. Once the atoms are found with the initial 2D Gaussian fit, a central cut horizontally and

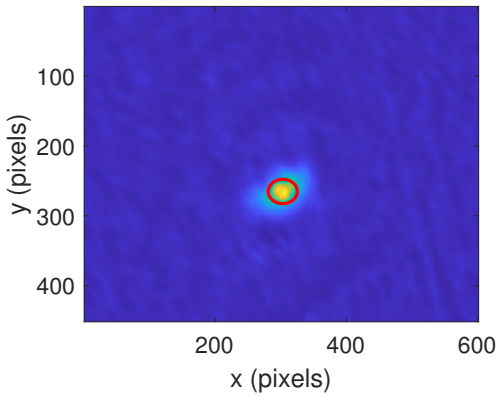

Figure A.7: Gaussian fitting locating atoms in an absorption image. The red circle is plotted using the extracted fitting parameters.

vertically is taken. This allows for 1D fitting of the function OD_{AXS}, where

$$\begin{aligned} OD_{AXS}(x) = & OD_{Gmaxx} \exp\left[-\frac{1}{2}\left(\frac{x-x_{G0}}{\sigma_{Gx}}\right)^2\right] + \\ & \Re\left\{OD_{TFmaxx}\left(1-\left(\frac{x-x_{TF0}}{\sigma_{TFx}}\right)^2\right)^{3/2}\right\}, \end{aligned} \tag{A.17}$$

and similarly for the complementary function in y. The initial start points for the optimisation of this function are taken from the 2D fit. The σ guesses are the same for both the Gaussian and the Thomas Fermi contributions, simply the computed 2D $\sigma x, y$. The maximum OD for each function are guessed at half the maximum OD from the 2D fit. The output for the cross sectional fit is shown in Figure A.8 for the y direction, but is computed for both directions independently.

The computed σ_{TFx} and σ_{TFy} are used to build a new array using Equation A.14, which is then subtracted from the image. This allows for a more accurate 2D fitting of just the thermal part of the cloud, which uses the 1D gauss fit parameters from the combined fit as initial starting points for the new 2D Gaussian fit. In the case used to illustrate, the change in calculated σ_{Gy} is 16.5 % and σ_{Gx} is 19.7 %.

Finally, the BEC part of the image is selected from the image using the Thomas Fermi radii from the 1D fit. This is now 2D fitted using the same Matlab optimisation function *fminunc* and Equation A.14. An estimation of the number of atoms in each

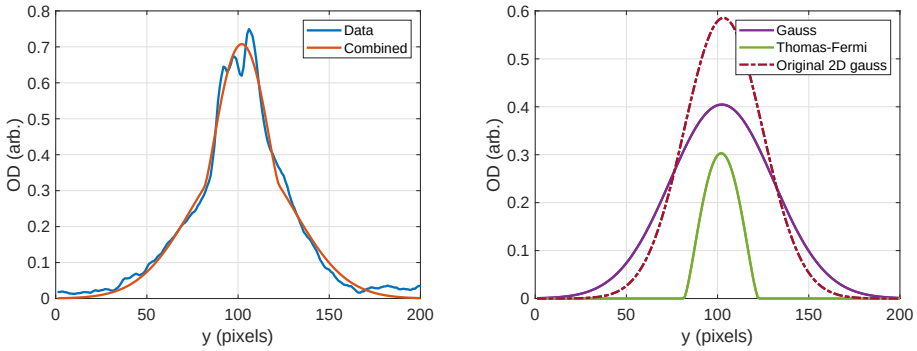

Figure A.8: 1D fitting of a combination of the Thomas Fermi and Gaussian functions to a central vertical cut of the image. Left, data (blue line) and the combined fitted function (red line). Right, the fits of different functions plotted separately to highlight the difference between the original 2D Gaussian fit and the new combined fits.

distribution is made using the maximum ODs and σs calculated from the 2D fits, giving out a final condensed fraction number.

In the case of the example used to illustrate this process the condensed fraction was found to be 8 %. The PSD of the atoms was close to 1, and so some condensed fraction is expected. However, only using the data presented in Figure A.8 to calculate the condensed fraction would lead to a significant over estimation. This is why the much more involved procedure described here is used. To confirm the validity of the procedure, atoms with a temperature of 2 µK and PSD on the order of 10^{-5} were also used. This gave no calculated contribution from the Thomas Fermi function, and returned a Gaussian fit similar to that of the original 2D fit, shown in Figure A.9. Comparison with Figure A.8 highlights the bi-modality at higher PSDs.

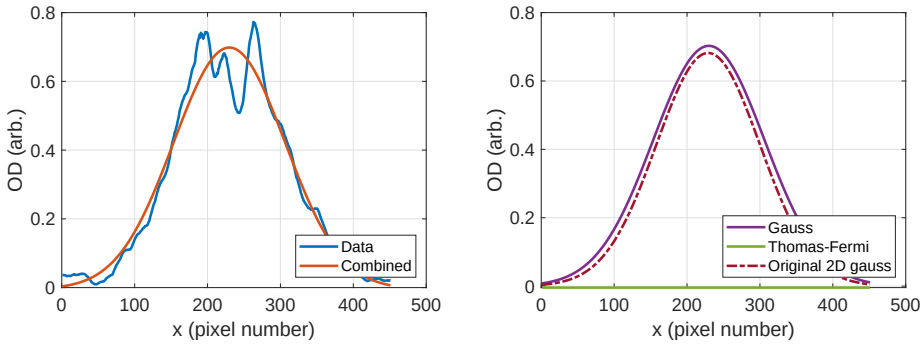

Figure A.9: Same as Figure A.8 for atoms with a PSD of $10^{-}5$. No BEC contribution is calculated, as expected.

Finally, the fitting procedure was tested against simulated data. Here, a bimodal distribution was artificially created to be fitted. With no noise, and no filtering, the procedure performs well, shown in Figure A.10a. Noise sees the procedure perform worse, but with some filtering a consistent response between actual condensed fraction and the calculated one can be achieved. This can be seen in Figure A.10b, where 20 % white noise is added to the simulated data. In conclusion, an accurate (and completely independent from user input) procedure to calculate the condensed fraction of an atom image has been developed.

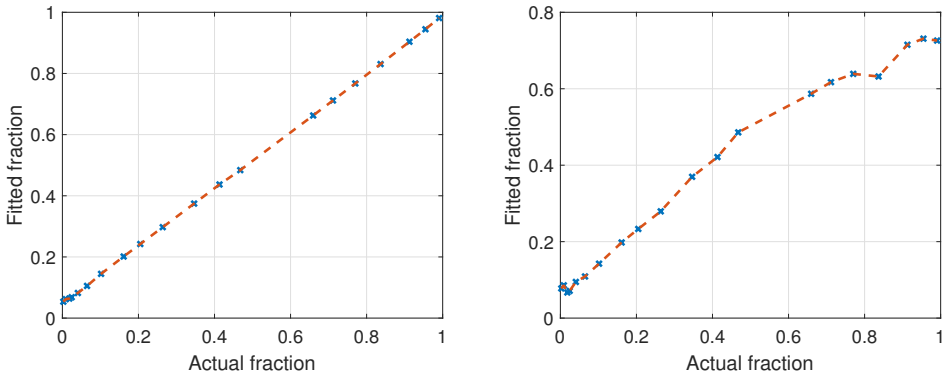

(a) No noise or filtering.

(b) 20 % noise, filtered.

Figure A.10: Testing of the developed procedure against simulated data. A bimodal distribution is created, giving an actual condensed fraction, and the fitted fraction is measured. In (a), the results with no noise and (b) with 20% white noise added and filtering which improves the estimated fraction.

Appendix B

Optimisation

A selection of parameter optimisation omitted earlier in the thesis are shown in Figure B.1. Optimisation is performed by varying the parameter and measuring a dependent variable such as atom number, density, temperature, and PSD.

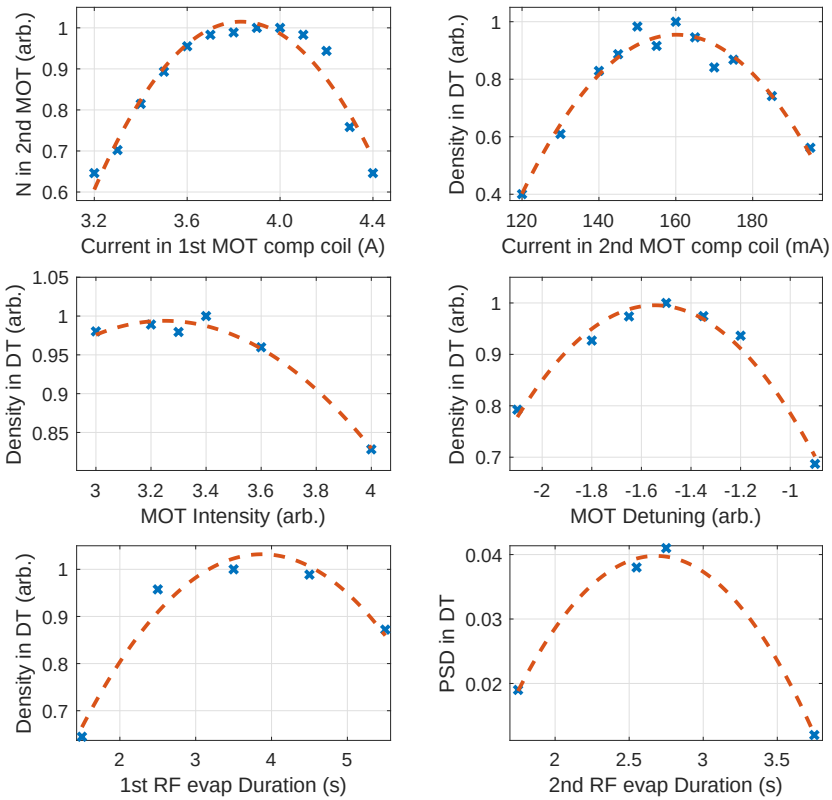

Figure B.1: Optimisation of a selection of parameters not reported earlier in the thesis.

Appendix C

Computer systems

This thesis is written in LaTeX, graphs are plotted in MATLAB, to scale 3D sketchs are made in Autodesk Inventor and illustrations are created in Inkscape with optical setup diagrams using the open source ComponentLibrary created by Alexander Franzen. Most of the experiment is run on custom built LabVIEW programs, which allow for microsecond interaction with hardware. An overview of these programs is shown in Figure C.1.

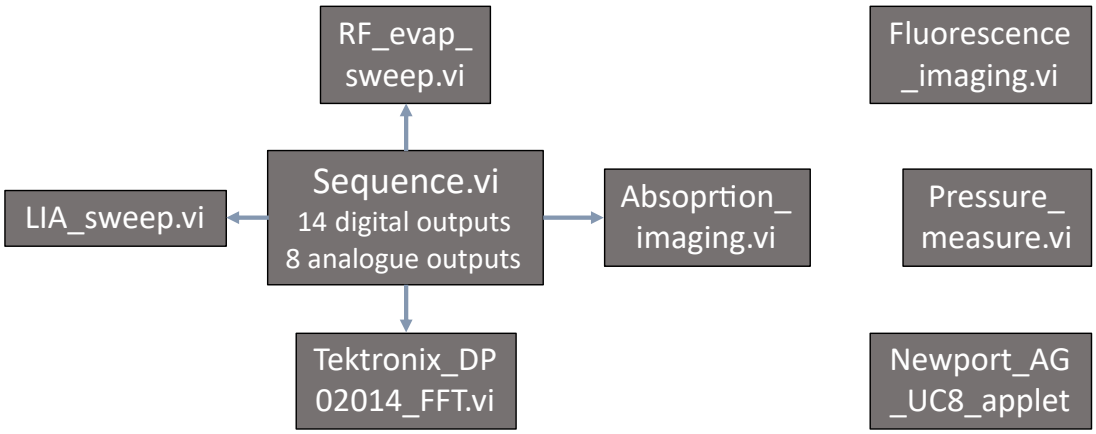

Figure C.1: Programs written or heavily modified by the author required for running the BEC ultracold magnetometer experiment. Sequence.vi interacts with a DAQ to drive 14 digital 8 analogue outputs. These control many different experimental hardware, as well as triggering further sub programs. For BEC production, RF evaporation is controlled via RF_evap_sweep.vi, with the atoms then imaged by Absorption_imaging.vi. Magnetometry is performed with either LIA_sweep.vi (for phase sensitive detection via a lock-in amplifier) or Tektronix_DP02014_FFT_vi (for SNR determination). Other programs which continuously monitor or used as needed are the Fluorescence_imaging.vi, Pressure_measure.vi and the Newport_AG_UC8_applet for moving the piezo-actuated mirrors.

Bibliography

[1] Y. Cohen, K. Jadeja, S. Sula, M. Venturelli, C. Deans, L. Marmugi, and F. Renzoni. A cold atom radio-frequency magnetometer. *App. Phys. Lett.*, 2019. doi:10.1063/1.5084004.

[2] C. Deans, Y. Cohen, H. Yao, B. Maddox, A. Vigilante, and F. Renzoni. Electromagnetic induction imaging with a scanning radio frequency atomic magnetometer. *Applied Physics Letters*, 2021. doi:10.1063/5.0056876.

[3] S. Xu, V. V. Yashchuk, M. H. Donaldson, S. M. Rochester, D. Budker, and A. Pines. Magnetic resonance imaging with an optical atomic magnetometer. *PNAS*, 2006. doi:10.1073/pnas.0605396103.

[4] H. C. Davis, P. Ramesh, A. Bhatnagar, A. Lee-Gosselin, J. F. Barry, D. R. Glenn, R. L. Walsworth, and M. G. Shapiro. Mapping the microscale origins of magnetic resonance image contrast with subcellular diamond magnetometry. *Nature Communications*, 2018. doi:10.1038/s41467-017-02471-7.

[5] K. Kim, S. Begus, H. Xia, S.-K. Lee, V. Jazbinsek, Z. Trontelj, and M. V. Romalis. Multi-channel atomic magnetometer for magnetoencephalography: A configuration study. *NeuroImage*, 2014. doi:10.1016/j.neuroimage.2013.10.040.

[6] R. M. Hill, E. Boto, N. Holmes, C. Hartley, Z. A. Seedat, J. Leggett, G. Roberts, V. Shah, T. M. Tierney, and M. W. Woolrich. A tool for functional brain imaging with lifespan compliance. *Nature Communications*, 2019. doi:10.1038/s41467-019-12486-x.

[7] P. Bevington, R. Gartman, W. Chalupczak, C. Deans, L. Marmugi, and F. Renzoni. Non-destructive structural imaging of steelwork with atomic magnetometers. *Appl. Phys. Lett.*, 2018. doi:10.1063/1.5042033.

[8] S. G. H. Staples, C. Vo, D. M. J. Cowell, S. Freear, C. Ives, and B. T. H. Varcoe. Solving the inverse problem of magnetisation–stress resolution. *Journal of Applied Physics*, 2013. doi:10.1063/1.4799049.

[9] H. Liu, H. Dong, J. Ge, Z. Liu, Z. Yuan, J. Zhu, and H. Zhang. Apparatus and method for efficient sampling of critical parameters demonstrated by monitoring an Overhauser geomagnetic sensor. *Review of Scientific Instruments*, 2018. doi:10.1063/1.5054749.

[10] G. Shorshi and I.Y. Bar-Itzhack. Satellite autonomous navigation and orbit determination using magnetometers. *Proceedings of the 31st IEEE Conference on Decision and Control*, 1992. doi:10.1109/CDC.1992.371675.

[11] M. H. Acuña. Space-based magnetometers. *Review of Scientific Instruments*, 2002. doi:10.1063/1.1510570.

[12] M. L. Psiaki. Global magnetometer-based spacecraft attitude and rate estimation. *Journal of Guidance, Control, and Dynamics*, 2004. doi:10.2514/1.1039.

[13] G. Baldini, F. Dimc, R. Kamnik, G. Steri, R. Giuliani, and C. Gentile. Identification of mobile phones using the built-in magnetometers stimulated by motion patterns. *Sensors*, 2017. doi:10.3390/s17040783.

[14] I. M. Savukov, S. J. Seltzer, and M. V. Romalis. Detection of NMR signals with a radio-frequency atomic magnetometer. *Journal of Magnetic Resonance*, 2007. doi:10.1016/j.jmr.2006.12.012.

[15] S.-K. Lee, K. L. Sauer, S. J. Seltzer, O. Alem, and M. V. Romalis. Subfemtotesla radio-frequency atomic magnetometer for detection of nuclear quadrupole resonance. *Applied Physics Letters*, 2006. doi:10.1063/1.2390643.

[16] S. A. Murthy, D. Krause, Z. L. Li, and L. R. Hunter. New limits on the electron electric dipole moment from cesium. *Phys. Rev. Lett.*, 1989. doi:10.1103/PhysRevLett.63.965.

[17] C. J. Berglund, L. R. Hunter, D. Krause, Jr., E. O. Prigge, M. S. Ronfeldt, and S. K. Lamoreaux. New limits on local lorentz invariance from hg and cs magnetometers. *Phys. Rev. Lett.*, 1995. doi:10.1103/PhysRevLett.75.1879.

[18] J. M. Brown, S. J. Smullin, T. W. Kornack, and M. V. Romalis. New limit on lorentz- and cpt-violating neutron spin interactions. *Phys. Rev. Lett.*, 2010. doi:10.1103/PhysRevLett.105.151604.

[19] B. J. Darrer, J. C. Watson, P. A. Bartlett, and F. Renzoni. Electromagnetic imaging through thick metallic enclosures. *AIP Advances*, 2015. doi:10.1063/1.4928864.

[20] R. Guilizzoni, J. C. Watson, P. Bartlett, and F. Renzoni. Penetrating power of resonant electromagnetic induction imaging. *AIP Advances*, 2016. doi:10.1063/1.4963299.

[21] C. Deans, L. Marmugi, and F. Renzoni. Through-barrier electromagnetic imaging with an atomic magnetometer. *Opt. Express*, 2017. doi:10.1364/OE.25.017911.

[22] C. Deans, L. Marmugi, and F. Renzoni. Active underwater detection with an array of atomic magnetometers. *Appl. Opt.*, 2018. doi:10.1364/AO.57.002346.

[23] L. Marmugi, C. Deans, and F. Renzoni. Electromagnetic induction imaging with atomic magnetometers: Unlocking the low-conductivity regime. *Applied Physics Letters*, 2019. doi:10.1063/1.5116811.

[24] K. Jensen, M. Zugenmaier, J. Arnbak, H. Stærkind, M. V. Balabas, and E. S. Polzik. Detection of low-conductivity objects using eddy current measurements with an optical magnetometer. *Phys. Rev. Research*, 2019. doi:10.1103/PhysRevResearch.1.033087.

[25] C. Deans, L. Marmugi, and F. Renzoni. Sub-sm–1 electromagnetic induction imaging with an unshielded atomic magnetometer. *Appl. Phys. Lett.*, 2020. doi:10.1063/5.0002146.

[26] L. Marmugi and F. Renzoni. Optical magnetic induction tomography of the heart. *Scientific Reports*, 2016. doi:10.1038/srep23962.

[27] L. Marmugi and F. Renzoni. Electromagnetic induction imaging with atomic magnetometers: Progress and perspectives. *Applied Sciences*, 2020. doi:10.3390/app10186370.

[28] V. Shah, S. Knappe, P. D. D. Schwindt, and J. Kitching. Subpicotesla atomic magnetometry with a microfabricated vapour cell. *Nature Photonics*, 2007. doi:10.1038/nphoton.2007.201.

[29] E. H. Hall. On a new action of the magnet on electric currents. *American Journal of Mathematics*, 1879.

[30] M. N. Baibich, J. M. Broto, A. Fert, F. Nguyen Van Dau, F. Petroff, P. Etienne, G. Creuzet, A. Friederich, and J. Chazelas. Giant magnetoresistance of (001)Fe/(001)Cr magnetic superlattices. *Phys. Rev. Lett.*, 1988. doi:10.1103/PhysRevLett.61.2472.

[31] P P Freitas, R Ferreira, S Cardoso, and F Cardoso. Magnetoresistive sensors. *Journal of Physics: Condensed Matter*, 2007. doi:10.1088/0953-8984/19/16/165221.

[32] F Primdahl. The fluxgate magnetometer. *Journal of Physics E: Scientific Instruments*, 1979. doi:10.1088/0022-3735/12/4/001.

[33] R. L. Fagaly. Superconducting quantum interference device instruments and applications. *Review of Scientific Instruments*, 2006. doi:10.1063/1.2354545.

[34] R. L. Fagaly. Superconducting quantum interference device instruments and applications. *Review of Scientific Instruments*, 2006. doi:10.1063/1.2354545.

[35] J.-H. Storm, P. Hömmen, D. Drung, and R. Körber. An ultra-sensitive and wide-band magnetometer based on a superconducting quantum interference device. *Applied Physics Letters*, 2017. doi:10.1063/1.4976823.

[36] John F. Barry, Jennifer M. Schloss, Erik Bauch, Matthew J. Turner, Connor A. Hart, Linh M. Pham, and Ronald L. Walsworth. Sensitivity optimization for nv-diamond magnetometry. *Rev. Mod. Phys.*, 2020. doi:10.1103/RevModPhys.92.015004.

[37] T. Wolf, P. Neumann, K. Nakamura, H. Sumiya, T. Ohshima, J. Isoya, and J. Wrachtrup. Subpicotesla diamond magnetometry. *Phys. Rev. X*, 2015. doi:10.1103/PhysRevX.5.041001.

[38] L Rondin, J-P Tetienne, T Hingant, J-F Roch, P Maletinsky, and V Jacques. Magnetometry with nitrogen-vacancy defects in diamond. *Reports on Progress in Physics*, 2014. doi:10.1088/0034-4885/77/5/056503.

[39] R. Schirhagl, K. Chang, M. Loretz, and C. L. Degen. Nitrogen-vacancy centers in diamond: Nanoscale sensors for physics and biology. *Annual Review of Physical Chemistry*, 2014. doi:10.1146/annurev-physchem-040513-103659.

[40] I. K. Kominis, T. W. Kornack, J. C. Allred, and M. V. Romalis. A subfemtotesla multichannel atomic magnetometer. *Nature*, 2003. doi:10.1038/nature01484.

[41] D. Budker and M. Romalis. Optical magnetometry. *Nature Physics*, 2007. doi:10.1038/nphys566.

[42] H. B. Dang, A. C. Maloof, and M. V. Romalis. Ultrahigh sensitivity magnetic field and magnetization measurements with an atomic magnetometer. *App. Phys. Lett.*, 2010. doi:10.1063/1.3491215.

[43] Arnold L. Bloom. Principles of operation of the rubidium vapormagnetometer. *Appl. Opt.*, 1962. doi:10.1364/AO.1.000061.

[44] E. Breschi, Z. D. Grujić, P. Knowles, and A. Weis. A high-sensitivity push-pull magnetometer. *Appl. Phys. Lett.*, 2014. doi:10.1063/1.4861458.

[45] D. Budker, W. Gawlik, D. F. Kimball, S. M. Rochester, V. V. Yashchuk, and A. Weis. Resonant nonlinear magneto-optical effects in atoms. *Rev. Mod. Phys.*, 2002. doi:10.1103/RevModPhys.74.1153.

[46] D. Budker, D. F. Kimball, S. M. Rochester, V. V. Yashchuk, and M. Zolotorev. Sensitive magnetometry based on nonlinear magneto-optical rotation. *Phys. Rev. A*, 2000. doi:10.1103/PhysRevA.62.043403.

[47] M. P. Ledbetter, V. M. Acosta, S. M. Rochester, D. Budker, S. Pustelny, and V. V. Yashchuk. Detection of radio-frequency magnetic fields using nonlinear magneto-optical rotation. *Phys. Rev. A*, 2007. doi:10.1103/PhysRevA.75.023405.

[48] S. Pustelny, A. Wojciechowski, M. Gring, M. Kotyrba, J. Zachorowski, and W. Gawlik. Magnetometry based on nonlinear magneto-optical rotation with amplitude-modulated light. *Journal of Applied Physics*, 2008. doi:10.1063/1.2844494.

[49] C. Affolderbach, M. Stähler, and S. Knappe. An all-optical, high-sensitivity magnetic gradiometer. *Appl Phys B*, 2002. doi:10.1007/s00340-002-0959-8.

[50] G. Liu and S. Gu. Experimental study of the CPT magnetometer worked on atomic energy level modulation. *Journal of Physics B: Atomic, Molecular and Optical Physics*, 2010. doi:10.1088/0953-4075/43/3/035004.

[51] I. Kominis, T. Kornack, and J. Allred. A subfemtotesla multichannel atomic magnetometer. *Nature*, 2003. doi:10.1038/nature01484.

[52] H. B. Dang, A. C. Maloof, and M. V. Romalis. Ultrahigh sensitivity magnetic field and magnetization measurements with an atomic magnetometer. *Appl. Phys. Lett.*, 2010. doi:10.1063/1.3491215.

[53] M. Vengalattore, J. M. Higbie, S. R. Leslie, J. Guzman, L. E. Sadler, and D. M. Stamper-Kurn. High-resolution magnetometry with a spinor Bose-Einstein condensate. *Phys. Rev. Let.*, 2007. doi:10.1103/PhysRevLett.98.200801.

[54] J. M. Higbie, L. E. Sadler, S. Inouye, A. P. Chikkatur, S. R. Leslie, K. L. Moore, V. Savalli, and D. M. Stamper-Kurn. Direct nondestructive imaging of magnetization in a spin-1 Bose-Einstein gas. *Phys. Rev. Lett.*, 2005. doi:10.1103/PhysRevLett.95.050401.

[55] S. Wildermuth, S. Hofferberth, I. Lesanovsky, S. Groth, P. Krüger, J. Schmiedmayer, and I. Bar-Joseph. Sensing electric and magnetic fields with Bose-Einstein condensates. *App. Phys. Lett.*, 2006. doi:10.1063/1.2216932.

[56] T. Isayama, Y. Takahashi, N. Tanaka, K. Toyoda, K. Ishikawa, and T. Yabuzaki. Observation of larmor spin precession of laser-cooled rb atoms via paramagnetic faraday rotation. *Phys. Rev. A*, 1999. doi:10.1103/PhysRevA.59.4836.

[57] C. Deans, L. Marmugi, and F. Renzoni. Sub-picotesla widely tunable atomic magnetometer operating at room-temperature in unshielded environments. *Review of Scientific Instruments*, 2018. doi:10.1063/1.5026769.

[58] L. Marmugi, C. Deans, and F. Renzoni. Electromagnetic induction imaging with atomic magnetometers: Unlocking the low-conductivity regime. *Applied Physics Letters*, 2019. doi:10.1063/1.5116811.

[59] C. Deans, L. Marmugi, S. Hussain, and F. Renzoni. Electromagnetic induction imaging with a radio-frequency atomic magnetometer. *Appl. Phys. Lett.*, 2016. doi:10.1063/1.4943659.

[60] L. Marmugi, L. Gori, S. Hussain, C. Deans, and F. Renzoni. Remote detection of rotating machinery with a portable atomic magnetometer. *Appl. Opt.*, 2017. doi:10.1364/AO.56.000743.

[61] C. Deans, L. D. Griffin, L. Marmugi, and F. Renzoni. Machine learning based localization and classification with atomic magnetometers. *Phys. Rev. Lett.*, 2018. doi:10.1103/PhysRevLett.120.033204.

[62] D. Becker, M. D. Lachmann, S. T. Seidel, H. Ahlers, A. N. Dinkelaker, J. Grosse, O. Hellmig, H. Muntinga, V. Schkolnik, T. Wendrich, and et. al.

Space-borne Bose–Einstein condensation for precision interferometry. *Nature*, 2018. doi:10.1038/s41586-018-0605-1.

[63] M. Cerna and A. F. Harvey. *The Fundamentals of FFT-Based Signal Analysis and Measurement*. National Instruments, 2000.

[64] V. G. Lucivero, P. Anielski, W. Gawlik, and M. W. Mitchell. Shot-noise-limited magnetometer with sub-picotesla sensitivity at room temperature. *Review of Scientific Instruments*, 2014. doi:10.1063/1.4901588.

[65] I. M. Savukov, S. J. Seltzer, K. L. Sauer, and M. V. Romalis. Tunable atomic magnetometer for detection of radio-frequency magnetic fields. *Phys. Rev. Let.*, 2005. doi:10.1103/PhysRevLett.95.063004.

[66] D. Budker, D. F. Kimball, S. M. Rochester, V. V. Yashchuk, and M. Zolotorev. Sensitive magnetometry based on nonlinear magneto-optical rotation. *Phys. Rev. A.*, 2000. doi:10.1103/PhysRevA.62.043403.

[67] J. R. Maze, P. L. Stanwix, J. S. Hodges, S. Hong, J. M. Taylor, P. Cappellaro, L. Jiang, M. V. Gurudev Dutt, E. Togan, and A. S. Zibrov. Nanoscale magnetic sensing with an individual electronic spin in diamond. *Nature*, 2008. doi:10.1038/nature07279.

[68] G. Balasubramanian, P. Neumann, D. Twitchen, M. Markham, R. Kolesov, N. Mizuochi, J. Isoya, J. Achard, J. Beck, and J. Tissler. Ultralong spin coherence time in isotopically engineered diamond. *Nature Materials*, 2009. doi:10.1038/nmat2420.

[69] G. Chatzidrosos, A. Wickenbrock, L. Bougas, N. Leefer, T. Wu, K. Jensen, Y. Dumeige, and D. Budker. Miniature cavity-enhanced diamond magnetometer. *Phys. Rev. Applied*, 2017. doi:10.1103/PhysRevApplied.8.044019.

[70] T. Wolf, P. Neumann, K. Nakamura, K. Sumiya, T. Ohshima, J. Isoya, and J. Wrachtrup. Subpicotesla diamond magnetometry. *Phys. Rev. X.*, 2015. doi:10.1103/PhysRevX.5.041001.

[71] P. D. D. Schwindt, B. Lindseth, S. Knappe, V. Shah, J. Kitching, and L. Liew. Chip-scale atomic magnetometer with improved sensitivity by use of the mx technique. *Applied Physics Letters*, 2007. doi:10.1063/1.2709532.

[72] P. D. D. Schwindt, S. Knappe, V. Shah, L. Hollberg, J. Kitching, L. Liew, and J. Moreland. Chip-scale atomic magnetometer. *Applied Physics Letters*, 2004. doi:10.1063/1.1839274.

[73] S. P. Krzyzewski, A. R. Perry, V. Gerginov, and S. Knappe. Characterization of noise sources in a microfabricated single-beam zero-field optically-pumped magnetometer. *Journal of Applied Physics*, 2019. doi:10.1063/1.5098088.

[74] V. Gerginov, M. Pomponio, and S. Knappe. Scalar magnetometry below 100 ft/hz¡sup¿1/2¡/sup¿ in a microfabricated cell. *IEEE Sensors Journal*, 2020. doi:10.1109/JSEN.2020.3002193.

[75] F. Baudenbacher, L. E. Fong, J. R. Holzer, and M. Radparvar. Monolithic low-transition-temperature superconducting magnetometers for high resolution imaging magnetic fields of room temperature samples. *Applied Physics Letters*, 2003. doi:10.1063/1.1572968.

[76] J. R. Kirtley, M. B. Ketchen, K. G. Stawiasz, J. Z. Sun, W. J. Gallagher, S. H. Blanton, and S. J. Wind. High-resolution scanning squid microscope. *Applied Physics Letters*, 1995. doi:10.1063/1.113838.

[77] W. Muessel, H. Strobel, D. Linnemann, D. B. Hume, and M. K. Oberthaler. Scalable spin squeezing for quantum-enhanced magnetometry with Bose-Einstein condensates. *Phys. Rev. Lett.*, 2014. doi:10.1103/PhysRevLett.113.103004.

[78] Y. Eto, H. Ikeda, H. Suzuki, S. Hasegawa, Y. Tomiyama, S. Sekine, M. Sadgrove, and T. Hirano. Spin-echo-based magnetometry with spinor Bose-Einstein condensates. *Phys. Rev. A*, 2013. doi:10.1103/PhysRevA.88.031602.

[79] M. Jasperse, M. J. Kewming, S. N. Fischer, P. Pakkiam, R. P. Anderson, and L. D. Turner. Continuous faraday measurement of spin precession without light shifts. *Phys. Rev. A*, 2017. doi:10.1103/PhysRevA.96.063402.

[80] J. F. Barry, J. M. Schloss, E. Bauch, M. J. Turner, C. A. Hart, L. M. Pham, and R. L. Walsworth. Sensitivity optimization for NV-diamond magnetometry. *Rev. Mod. Phys.*, 2019. doi:10.1103/RevModPhys.92.015004.

[81] D. A Steck. Rubidium 87 D line data. `https://steck.us/alkalidata/rubidium87numbers.pdf`, 2003.

[82] C. J. Pethick and H. Smith. *Bose–Einstein Condensation in Dilute Gases*. 2008. doi:10.1017/CBO9780511802850.

[83] K. M. O'Hara, S. R. Granade, M. E. Gehm, T. A. Savard, S. Bali, C. Freed, and J. E. Thomas. Ultrastable CO_2 laser trapping of lithium fermions. *Phys. Rev. Lett.*, 1999. doi:10.1103/PhysRevLett.82.4204.

[84] V. Giovannetti, S. Lloyd, and L. Maccone. Quantum-enhanced measurements: Beating the standard quantum limit. *Science*, 2004. doi:10.1126/science.1104149.

[85] W. Wasilewski, K. Jensen, H. Krauter, J. J. Renema, M. V. Balabas, and E. S. Polzik. Quantum noise limited and entanglement-assisted magnetometry. *Phys. Rev. Lett.*, 2010. doi:10.1103/PhysRevLett.104.133601.

[86] R. J. Sewell, M. Koschorreck, M. Napolitano, B. Dubost, N. Behbood, and M. W. Mitchell. Magnetic sensitivity beyond the projection noise limit by spin squeezing. *Phys. Rev. Lett.*, 2012. doi:10.1103/PhysRevLett.109.253605.

[87] F. Bloch. Nuclear induction. *Phys. Rev.*, 1946. doi:10.1103/PhysRev.70.460.

[88] A. Abragam. *The principles of nuclear magnetism; Reprint with corrections*. 1989.

[89] S. J. Smullin, I. M. Savukov, G. Vasilakis, R. K. Ghosh, and M. V. Romalis. Low-noise high-density alkali-metal scalar magnetometer. *Physical Review A*, 2009. doi:10.1103/PhysRevA.80.033420.

[90] S. Chu, L. Hollberg, J. E. Bjorkholm, A. Cable, and A. Ashkin. Three-dimensional viscous confinement and cooling of atoms by resonance radiation pressure. *Physical Review Letters*, 1985. doi:10.1103/PhysRevLett.55.48.

[91] E. L. Raab, M. Prentiss, A. Cable, S. Chu, and D. E. Pritchard. Trapping of neutral sodium atoms with radiation pressure. *Phys. Rev. Lett.*, 1987. doi:10.1103/PhysRevLett.59.2631.

[92] C. Monroe, W. Swann, H. Robinson, and C. Wieman. Very cold trapped atoms in a vapor cell. *Phys. Rev. Lett.*, 1990. doi:10.1103/PhysRevLett.65.1571.

[93] S. Chu. Nobel lecture: The manipulation of neutral particles. *Rev. Mod. Phys.*, 1998. doi:10.1103/RevModPhys.70.685.

[94] C. N. Cohen-Tannoudji. Nobel lecture: Manipulating atoms with photons. *Rev. Mod. Phys.*, 1998. doi:10.1103/RevModPhys.70.707.

[95] W. D. Phillips. Nobel lecture: Laser cooling and trapping of neutral atoms. *Rev. Mod. Phys.*, 1998. doi:10.1103/RevModPhys.70.721.

[96] C. Cohen-Tannoudji. Laser cooling and trapping of neutral atoms: theory. *Physics Reports*, 1992. doi:10.1016/0370-1573(92)90133-K.

[97] A. Aspect. Manipulation of neutral atoms. experiments. *Physics Reports*, 1992. doi:10.1016/0370-1573(92)90132-J.

[98] M. H. Anderson, J. R. Ensher, M. R. Matthews, C. E. Wieman, and E. A. Cornell. Observation of Bose-Einstein condensation in a dilute atomic vapor. *Science*, 1995. doi:10.1126/science.269.5221.198.

[99] K. B. Davis, M. O. Mewes, M. R. Andrews, N. J. van Druten, D. S. Durfee, D. M. Kurn, and W. Ketterle. Bose-Einstein condensation in a gas of sodium atoms. *Phys. Rev. Lett.*, 1995. doi:10.1103/PhysRevLett.75.3969.

[100] C. C. Bradley, C. A. Sackett, J. J. Tollett, and R. G. Hulet. Evidence of Bose-Einstein condensation in an atomic gas with attractive interactions. *Phys. Rev. Lett.*, 1995. doi:10.1103/PhysRevLett.75.1687.

[101] S. L. Cornish, N. R. Claussen, J. L. Roberts, E. A. Cornell, and C. E. Wieman. Stable ^{85}Rb Bose-Einstein condensates with widely tunable interactions. *Phys. Rev. Lett.*, 2000. doi:10.1103/PhysRevLett.85.1795.

[102] D. G. Fried, T. C. Killian, L. Willmann, D. Landhuis, S. C. Moss, D. Kleppner, and T. J. Greytak. Bose-Einstein condensation of atomic hydrogen. *Phys. Rev. Lett.*, 1998. doi:10.1103/PhysRevLett.81.3811.

[103] A. Robert, O. Sirjean, A. Browaeys, J. Poupard, S. Nowak, D. Boiron, C. I. Westbrook, and A. Aspect. A Bose-Einstein condensate of metastable atoms. *Science*, 2001. doi:10.1126/science.1060622.

[104] T. Weber, J. Herbig, M. Mark, H. Nägerl, and R. Grimm. Bose-Einstein condensation of cesium. *Science*, 2003. doi:10.1126/science.1079699.

[105] W. D. Phillips and H. Metcalf. Laser deceleration of an atomic beam. *Phys. Rev. Lett.*, 1982. doi:10.1103/PhysRevLett.48.596.

[106] P. D. Lett, R. N. Watts, C. I. Westbrook, W. D. Phillips, P. L. Gould, and H. J. Metcalf. Observation of atoms laser cooled below the doppler limit. *Phys. Rev. Lett.*, 1988. doi:10.1103/PhysRevLett.61.169.

[107] D. S. Weiss, E. Riis, Y. Shevy, P. J. Ungar, and S. Chu. Optical molasses and multilevel atoms: experiment. *J. Opt. Soc. Am. B*, 1989. doi:10.1364/JOSAB.6.002072.

[108] J. Dalibard and C. Cohen-Tannoudji. Laser cooling below the doppler limit by polarization gradients: simple theoretical models. *J. Opt. Soc. Am. B*, 1989. doi:10.1364/JOSAB.6.002023.

[109] P. D. Lett, W. D. Phillips, S. L. Rolston, C. E. Tanner, R. N. Watts, and C. I. Westbrook. Optical molasses. *J. Opt. Soc. Am. B*, 1989. doi:10.1364/JOSAB.6.002084.

[110] W. Ketterle and N. J. Van Druten. *Evaporative Cooling of Trapped Atoms*. 1996. doi:10.1016/S1049-250X(08)60101-9.

[111] A. L. Migdall, J. V. Prodan, W. D. Phillips, T. H. Bergeman, and H. J. Metcalf. First observation of magnetically trapped neutral atoms. *Phys. Rev. Lett.*, 1985. doi:10.1103/PhysRevLett.54.2596.

[112] W. Petrich, M. H. Anderson, J. R. Ensher, and E. A. Cornell. Stable, tightly confining magnetic trap for evaporative cooling of neutral atoms. *Phys. Rev. Lett.*, 1995. doi:10.1103/PhysRevLett.74.3352.

[113] H. J. Metcalf and P. van der Straten. *Laser Cooling and Trapping of Neutral Atoms*. Amer. Canc. Soci., 2007. doi:10.1002/9783527600441.oe005.

[114] M. H. Anderson, J. R. Ensher, M. R. Matthews, C. E. Wieman, and E. A. Cornell. Observation of Bose-Einstein condensation in a dilute atomic vapor. *Science*, 1995. doi:10.1126/science.269.5221.198.

[115] K. B. Davis, M. O. Mewes, M. R. Andrews, N. J. van Druten, D. S. Durfee, D. M. Kurn, and W. Ketterle. Bose-Einstein condensation in a gas of sodium atoms. *Phys. Rev. Lett.*, 1995. doi:10.1103/PhysRevLett.75.3969.

[116] Yu T Baiborodov, M S Ioffe, V M Petrov, and R I Sobolev. An adiabatic trap with combined magnetic field. *Nucl. Ener. C*, 1963. doi:10.1088/0368-3281/5/6/315.

[117] D. E. Pritchard. Cooling neutral atoms in a magnetic trap for precision spectroscopy. *Phys. Rev. Lett.*, 1983. doi:10.1103/PhysRevLett.51.1336.

[118] T. Bergeman, Gidon Erez, and Harold J. Metcalf. Magnetostatic trapping fields for neutral atoms. *Phys. Rev. A*, 1987. doi:10.1103/PhysRevA.35.1535.

[119] M.-O. Mewes, M. R. Andrews, N. J. van Druten, D. M. Kurn, D. S. Durfee, C. G. Townsend, and W. Ketterle. Collective excitations of a Bose-Einstein condensate in a magnetic trap. *Phys. Rev. Lett.*, 1996. doi:10.1103/PhysRevLett.77.988.

[120] T. Bergeman, Gidon Erez, and Harold J. Metcalf. Magnetostatic trapping fields for neutral atoms. *Phys. Rev. A*, 1987. doi:10.1103/PhysRevA.35.1535.

[121] C. R. Monroe, E. A. Cornell, C. A. Sackett, C. J. Myatt, and C. E. Wieman. Measurement of cs-cs elastic scattering at t=30 μk. *Phys. Rev. Lett.*, 1993. doi:10.1103/PhysRevLett.70.414.

[122] T. Esslinger, I. Bloch, and T. W. Hänsch. Bose-Einstein condensation in a quadrupole-ioffe-configuration trap. *Phys. Rev. A*, 1998. doi:10.1103/PhysRevA.58.R2664.

[123] R. G. Dall and A. G. Truscott. Bose–Einstein condensation of metastable heliumin a bi-planar quadrupole ioffe configuration trap. *Opt. Comm.*, 2006. doi:10.1016/j.optcom.2006.09.031.

[124] V. Bolpasi, J. Grucker, M. J Morrissey, and W. Von-Klitzing. A gradient and offset compensated ioffe–pritchard trap for Bose–Einstein condensation experiments. *Jour. of Phys. B*, 2012. doi:10.1088/0953-4075/45/23/235301.

[125] O. Morizot, C. L. Garrido-Alzar, P. E. Pottie, V. Lorent, and Perrin. H. Trapping and cooling of rf-dressed atoms in a quadrupole magnetic field. *Jour. of Phys. B*, 2007. doi:10.1088/0953-4075/40/20/004.

[126] S. Hofferberth, I. Lesanovsky, and B. Fischer. Radiofrequency-dressed-state potentials for neutral atoms. *Nat. Phys.*, 2006. doi:10.1038/nphys420.

[127] M. White, H. Gao, M. Pasienski, and B. DeMarco. Bose-Einstein condensates in rf-dressed adiabatic potentials. *Phys. Rev. A*, 2006. doi:10.1103/PhysRevA.74.023616.

[128] P. W. Courteille, B. Deh, J. Fortagh, A. Günther, S. Kraft, C. Marzok, S. Slama, and C. Zimmermann. Highly versatile atomic micro traps generated by multi-frequency magnetic field modulation. *Jour. of Phys. B*, 2006. doi:10.1088/0953-4075/39/5/005.

[129] N. R. Thomas, A. C. Wilson, and C. J. Foot. Double-well magnetic trap for Bose-Einstein condensates. *Phys. Rev. A*, 2002. doi:10.1103/PhysRevA.65.063406.

[130] I. Lesanovsky and W. Von-Klitzing. Time-averaged adiabatic potentials: Versatile matter-wave guides and atom traps. *Phys. Rev. Lett.*, 2007. doi:10.1103/PhysRevLett.99.083001.

[131] B. E. Sherlock, M. Gildemeister, E. Owen, E. Nugent, and C. J. Foot. Time-averaged adiabatic ring potential for ultracold atoms. *Phys. Rev. A*, 2011. doi:10.1103/PhysRevA.83.043408.

[132] A. D. West, C. G. Wade, K. J. Weatherill, and I. G. Hughes. Piezoelectrically actuated time-averaged atomic microtraps. *Appl. Phys. Lett.*, 2012. doi:10.1063/1.4736580.

[133] R. Grimm, M. Weidemüller, and Y. B. Ovchinnikov. Optical dipole traps for neutral atoms. *Advances In Atomic, Molecular, and Optical Physics*, 2000. doi:https://doi.org/10.1016/S1049-250X(08)60186-X.

[134] C. Y. Shih and M. S. Chapman. Nondestructive light-shift measurements of single atoms in optical dipole traps. *Phys. Rev. A*, 2013. doi:10.1103/PhysRevA.87.063408.

[135] M. D. Barrett, J. A. Sauer, and M. S. Chapman. All-optical formation of an atomic Bose-Einstein condensate. *Phys. Rev. Lett.*, 2001. doi:10.1103/PhysRevLett.87.010404.

[136] T. Weber, J. Herbig, M. Mark, H.-C. Nägerl, and R. Grimm. Bose-Einstein condensation of cesium. *Science*, 2003. doi:10.1126/science.1079699.

[137] G. Cennini, G. Ritt, and C. Geckeler. Bose–Einstein condensation in a co2-laser optical dipole trap. *Appl. Phys. B*, 2003. doi:10.1007/s00340-003-1333-1.

[138] D. Comparat, A. Fioretti, G. Stern, E. Dimova, B. Laburthe Tolra, and P. Pillet. Optimized production of large Bose-Einstein condensates. *Phys. Rev. A*, 2006. doi:10.1103/PhysRevA.73.043410.

[139] Y.-J. Lin, A. R. Perry, R. L. Compton, I. B. Spielman, and J. V. Porto. Rapid production of ^{87}Rb Bose-Einstein condensates in a combined magnetic and optical potential. *Phys. Rev. A*, 2009. doi:10.1103/PhysRevA.79.063631.

[140] D. L. Jenkin, D.J. McCarron, and M. P. Köppinger. Bose-Einstein condensation of ^{87}Rb in a levitated crossed dipole trap. *Eur. Phys. J. D.*, 2011. doi:10.1140/epjd/e2011-10720-5.

[141] A.S. Flores, H.P. Mishra, and W. Vassen. Simple method for producing Bose–Einstein condensates of metastable helium using a single-beam optical dipole trap. *Appl. Phys. B*, 2015. doi:10.1007/s00340-015-6243-5.

[142] C.-L. Hung, X. Zhang, N. Gemelke, and C. Chin. Accelerating evaporative cooling of atoms into Bose-Einstein condensation in optical traps. *Phys. Rev. A*, 2008. doi:10.1103/PhysRevA.78.011604.

[143] F. Dalfovo, S. Giorgini, L. P. Pitaevskii, and S. Stringari. Theory of Bose-Einstein condensation in trapped gases. *Rev. Mod. Phys.*, 1999. doi:10.1103/RevModPhys.71.463.

[144] V. Bagnato, D. E. Pritchard, and D. Kleppner. Bose-Einstein condensation in an external potential. *Phys. Rev. A*, 1987. doi:10.1103/PhysRevA.35.4354.

[145] J. R. Ensher, D. S. Jin, M. R. Matthews, C. E. Wieman, and E. A. Cornell. Bose-Einstein condensation in a dilute gas: Measurement of energy and ground-state occupation. *Phys. Rev. Lett.*, 1996. doi:10.1103/PhysRevLett.77.4984.

[146] Z. T. Lu, K. L. Corwin, M. J. Renn, M. H. Anderson, E. A. Cornell, and C. E. Wieman. Low-velocity intense source of atoms from a magneto-optical trap. *Phys. Rev. Lett.*, 1996. doi:10.1103/PhysRevLett.77.3331.

[147] *Dual Controller User Manual*. Agilent Technologies, 2011. 87-900-094-01.

[148] M. Prentiss, A. Cable, J. E. Bjorkholm, Steven Chu, E. L. Raab, and D. E. Pritchard. Atomic-density-dependent losses in an optical trap. *Opt. Lett.*, 1988. doi:10.1364/OL.13.000452.

[149] T. Arpornthip, C. A. Sackett, and K. J. Hughes. Vacuum-pressure measurement using a magneto-optical trap. *Phys. Rev. A*, 2012. doi:10.1103/PhysRevA.85.033420.

[150] R. W. G. Moore, L. A. Lee, E. A. Findlay, L. Torralbo-Campo, G. D. Bruce, and D. Cassettari. Measurement of vacuum pressure with a magneto-optical trap: A pressure-rise method. *Review of Scientific Instruments*, 2015. doi:10.1063/1.4928154.

[151] D. E. Fagnan, J. Wang, C. Zhu, P. Djuricanin, B. G. Klappauf, J. L. Booth, and K. W. Madison. Observation of quantum diffractive collisions using shallow atomic traps. *Phys. Rev. A*, 2009. doi:10.1103/PhysRevA.80.022712.

[152] M. Prentiss, A. Cable, J. E. Bjorkholm, Steven Chu, E. L. Raab, and D. E. Pritchard. Atomic-density-dependent losses in an optical trap. *Opt. Lett.*, 1988. doi:10.1364/OL.13.000452.

[153] A. Millett-Sikking, I. G. Hughes, P. Tierney, and S. L. Cornish. DAVLL lineshapes in atomic rubidium. *J. Phys. B: At. Mol. Opt. Phys.*, 2007. doi:10.1088/0953-4075/40/1/017.

[154] G. C. Bjorklund. Frequency-modulation spectroscopy: a new method for measuring weak absorptions and dispersions. *Opt. Lett., OL*, 1980. doi:10.1364/OL.5.000015.

[155] E. A. Donley, T. P. Heavner, F. Levi, M. O. Tataw, and S. R. Jefferts. Double-pass acousto-optic modulator system. *Review of Scientific Instruments*, 2005. doi:10.1063/1.1930095.

[156] D. A Steck. Rubidium 85 D line data. `https://steck.us/alkalidata/rubidium85numbers.pdf`, 2003.

[157] W. Petrich, M. H. Anderson, J. R. Ensher, and E. A. Cornell. Behavior of atoms in a compressed magneto-optical trap. *J. Opt. Soc. Am. B*, 1994. doi:10.1364/JOSAB.11.001332.

[158] C. Deans. Electromagnetic Induction Imaging with Atomic Magnetometers. `https://discovery.ucl.ac.uk/id/eprint/10063674/`, 2018.

[159] A. F. R. Alvarez, E. Franco-Mejía, and C. R. Pinedo-Jaramillo. Study and analysis of magnetic field homogeneity of square and circular helmholtz coil pairs. In *2012 VI Andean Region International Conference*, 2012. doi:10.1109/Andescon.2012.27.

[160] S. Pustelny, A. Wojciechowski, M. Gring, M. Kotyrba, J. Zachorowski, and W. Gawlik. Magnetometry based on nonlinear magneto-optical rotation with amplitude-modulated light. *Journal of Applied Physics*, 2008. doi:10.1063/1.2844494.

[161] A. J. Barker, H. Style, K. Luksch, S. Sunami, D. Garrick, F. Hill, C. J. Foot, and E. Bentine. Applying machine learning optimization methods to the production of a quantum gas. *Machine Learning: Science and Technology*, 2020. doi:10.1088/2632-2153/ab6432.

[162] F. Gerbier, J. H. Thywissen, S. Richard, M. Hugbart, P. Bouyer, and A. Aspect. Experimental study of the thermodynamics of an interacting trapped Bose-Einstein condensed gas. *Phys. Rev. A*, 2004. doi:10.1103/PhysRevA.70.013607.

[163] E. A. L. Henn, J. A. Seman, G. B. Seco, E. P. Olimpio, P. Castilho, G. Roati, D. V. Magalhaes, K. M. Magalhaes, and V. S. Bagnato. Bose-Einstein condensation in 87rb: characterization of the brazilian experiment. *Brazilian Journal of Physics*, 2008. doi:10.1590/S0103-97332008000200012.

[164] Christopher J Foot. *Atomic physics*. Oxford University Press, 2007.

[165] Edward C Jordan and Keith G Balmain. *Electromagnetic waves and radiating systems*. 1968.

[166] H. J. Lewandowski, D. M. Harber, D. L. Whitaker, and E. A. Cornell. Simplified system for creating a Bose–Einstein condensate. *Journal of Low Temperature Physics*, 2003. doi:10.1023/A:1024800600621.

[167] Y. Castin and R. Dum. Bose-Einstein condensates in time dependent traps. *Phys. Rev. Lett.*, 1996. doi:10.1103/PhysRevLett.77.5315.

[168] G. Baym and C. J. Pethick. Ground-state properties of magnetically trapped Bose-condensed rubidium gas. *Phys. Rev. Lett.*, 1996. doi:10.1103/PhysRevLett.76.6.

[169] J. Szczepkowski, R. Gartman, M. Witkowski, L. Tracewski, M. Zawada, and Gawlik W. Analysis and calibration of absorptive images of Bose-Einstein condensate at non-zero temperatures. *Rev. Sci. Inst.*, 2009. doi:10.1063/1.3125051.